Masterarbeit

Design and Implementation of a Wireless Sensor Platform for River Monitoring Based on Energy Harvesting

Leander Bernd Hörmann, BSc

Institut für Technische Informatik
Technische Universität Graz
Vorstand: O. Univ.-Prof. Dipl.-Ing. Dr. techn. Reinhold Weiß

Begutachter: Ass.Prof. Dipl.-Ing. Dr. techn. Christian Steger
Betreuer: Dipl.-Ing. Philipp Maria Glatz, Bakk.techn.
Ass.Prof. Dipl.-Ing. Dr. techn. Christian Steger

Graz, im März 2010

Kurzfassung

Der aktuelle Wasserstand und die Fließgeschwindigkeit eines Flusses sind von großer Bedeutung für Frühwarnsysteme von Hochwasser. Auch Wasserkraftwerke können diese Information für eine optimale Regelung verwenden. Weitere Anwendungsbereiche sind Wasserbau und Wassersportveranstaltungen.

Die Sensoren existierender Informationssysteme sind hauptsächlich an Gebäuden, zum Beispiel Brücken, angebracht. Sie müssen regelmäßig gewartet werden und sind meist nicht netzwerkfähig. Deshalb sind der Aufbau und der Betrieb solcher Systeme sehr kostenintensiv.

Diese Masterarbeit präsentiert einen Prototyp zur Verwendung in autonomen Flussinformationssystemen. Sie beinhaltet die Entwicklung und die Realisierung einer batterielosen Sensornetz-Plattform zur Flussüberwachung. Die Hardware ist in eine Boje eingebaut, um direkt im Fluss den Wasserstand bestimmen zu können. Dafür werden Ultraschall-Transceiver und ein GPS Modul verwendet. Es werden Solarzellen verwendet, um die Sonnenstrahlung in elektrische Energie umzuwandeln. Für den Betrieb in der Nacht wird die Energie in Ultrakondensatoren gespeichert.

Der entwickelte Prototyp ist kostengünstig, erweiterbar, langlebig und wartungsfrei. Die Sensornetz-Plattform ist so ausgelegt, um verschiedene Energiesparmethoden für Sensornetze testen zu können. Beispiele sind energiesparende Betriebszustände, Veränderung der Arbeitszyklen und Vorhersage der verfügbaren Energie.

Um die korrekte Funktionalität des entwickelten Prototyps zu zeigen, wird jede Komponente getestet. Ein Langzeittest demonstriert die autarke Versorgung des Prototypen mit Hilfe von Solarzellen.

Abstract

A river's water level and flow are the most important factors for flood warning information systems and for hydroelectric power plants to perform an optimal control. Further application areas are hydraulic engineering and sport events.

The sensors of existing information systems are mainly mounted on buildings (e.g. a bridge). These systems need to be serviced regularly and do not provide integrated networking capabilities, which increase the cost of building, deploying and maintaining such systems.

This master's thesis presents a prototype for setting up an autonomous water level information system. It covers the design and implementation of a battery-less wireless sensor network (WSN) platform for river monitoring. The hardware is mounted into a buoy for in-river measurements of the water level. The measurements are done with ultrasonic transceivers and a GPS module. Solar cells are used to harvest energy. The energy is stored in ultracapacitors to enable continuous operation during the night.

The developed prototype is cost-saving, extendable, durable and maintenance-free. The WSN platform is designed to be able to test various energy-saving methods like low-power modes (LPMs), duty cycling and energy harvesting prediction schemes.

The proper functionality of the developed prototype is shown by testing each component. A long-term test demonstrates the self-sustaining supply of the prototype via solar cells.

Keywords

wireless sensor network, energy harvesting, energy harvesting system, solar cell, ultracapacitor, battery-less, river level monitoring, ultrasonic sensor, GPS module

STATUTORY DECLARATION

I declare that I have authored this thesis independently, that I have not used other than the declared sources / resources, and that I have explicitly marked all material which has been quoted either literally or by content from the used sources.

....
date (signature)

Acknowledgment

I thank my parents, who supported me during the whole studies. My studies would not possible without my parents.

I also express my special gratitude to my girlfriend Sabine for her support and the patience in the last year.

I thank all the people of the Institute for Technical Informatics, especially Dipl.-Ing.(FH) Engelbert Meissl and Ing. Kurt Haller who supported me during the setup of the prototype.

Special thanks goes to my advisor, Dipl.-Ing. Philipp Maria Glatz, Bakk.techn., who supported me perfectly during the whole master's thesis. He always helped me, when I did not know how to go on.

Finally, I thank my assessor, Ass.Prof. Dipl.-Ing. Dr. techn. Christian Steger.

March 2010 Leander Bernd Hörmann

Contents

1 Introduction and Outline

Ubiquitous computing has a very ambitious vision. It is the seamless integration of computational power into the environment. State-of-the-art solutions are implemented using so-called wireless sensor networks (WSNs). These networks consist of highly integrated wireless sensor nodes, which are able to measure specific values of the environment, to process the measured data and to communicate with other wireless sensor nodes. The wireless communication highly increases the mobility and the flexibility of such wireless sensor nodes. These wireless sensor nodes are also known as motes.

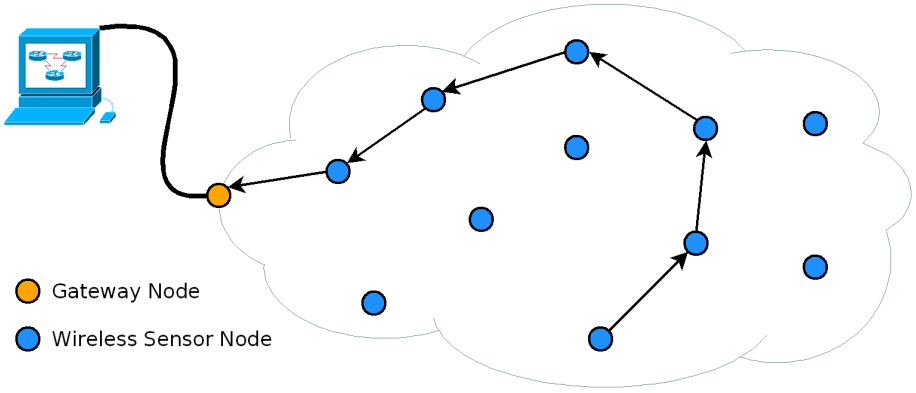

Figure 1.1: Typical structure of a wireless sensor network.

Figure 1.1 shows a typical structure of a WSN. The motes send the measured and processed data to a gateway node. The gateway node is connected to a computer, which stores the data from the motes. It is often called base station. Usually the gateway node has the ability to measure and process data, too. A multi-hop routing protocol is used to transmit the data through the WSN.

The field of application of WSNs is manifold. They can be used in agriculture for temperature or ground well level monitoring. The measurement of the temperature and the humidity in greenhouses are also an example for an agricultural use. WSNs can also be used for home automation and smart buildings. There, they are used for HVAC (heating, ventilating and air conditioning). Further fields of application are for example vehicle detection, health monitoring, military use and various commercial applications [1].

The power supply of the motes is a big challenge. Normal batteries have a limited capacity. Therefore, the operating time of the battery-powered motes is limited.

Some motes are equipped with a so-called energy harvesting system (EHS). Such a system harvests energy from the environment. It uses energy harvesting devices (EHDs), e.g. solar cells, thermogenerators or piezoelectric generators. The operating time of a mote with an EHS is much longer than without. Therefore, it is possible to enhance the

operating time up to the lifetime of the components. Because *energy from the environment is generally unpredictable, discontinuous, and unstable* [16], the energy must be stored to enable a continuous mode of operation. For example, solar cells harvest energy only if they are exposed to light. Energy storage devices are used in such cases, e.g. rechargeable batteries or ultracapacitors.

A WSN platform consists of the mote itself, the EHD, the EHS and the energy storage device. The unit of these components is named RiverMote.

1.1 River Monitoring

River monitoring is essential for the residents and for various applications around the river. Typical application areas are the control of hydroelectric power plants and flood warning systems. Furthermore, it can be used for leisure time activity information systems, e.g. for fishing or kayak. The monitoring and recording of the river's water level have a very long tradition. In the past, it was done manually. Today it is done by information systems that measure the water level automatically.

WSNs can enhance the accuracy and the coverage of such information systems. Much more sensors are used and so an area-wide network can be created. The motes must be able to measure the water level of the river and to communicate with each other. So the data of the water level can be sent via other nodes to a gateway node.

1.2 Outline of the Master's Thesis

This master's thesis is about the design, implementation and testing of a wireless sensor platform for river monitoring based on energy harvesting.

River monitoring itself can be done in different ways. A part of this work is to find out how the water level of a river can be measured. The measurement components are selected with respect to minimal power consumption and low costs.

One key feature of this platform is the battery-less design. Hence, the energy is stored in an ultracapacitor. A RiverMote must harvest enough energy to allow a continuous mode of operation. Therefore, power estimation is done to be able to select one or more appropriate EHDs.

The implementation of the WSN platform consists of the hardware part and the software part. First, detailed circuits of the EHS and the mote are created. The hardware of the mote is designed to port TinyOS onto it. Then, the software is written specially for this mote. The software is only used for testing the various functionality of hardware.

A prototype of the hardware is built. This prototype is used to verify and test the dimensioning and the functionality of the EHS and mote hardware. The prototype enables to test various network protocols in conjunction with the EHS. The following requirements should be met:

1. The accuracy of the measured water level is equal or better than 10 cm.
2. The range of communication is greater than 500 m (line of sight).
3. At least two different measurement principles should be used.

4. The data delivery interval is lower than 15 *min*.
5. The cost of the hardware of one RiverMote is lower than € 500.
6. A porting of TinyOS must be possible.
7. Further sensors can be connected to the hardware.

Finally, the written part of the master's thesis contains a detailed documentation of the parts described above. In addition, the test results are visualized and discussed in the work.

1.3 Structure of this Document

This document is separated into seven Chapters. The first Chapter contains the introduction and outline of the master's thesis. The related work is discussed in the second Chapter. Several different applications of WSNs can be found there. Chapter three contains the concept of the WSN platform. Chapter four shows the detailed implementation of the hardware of the RiverMote. The implementation of the software is shown in Chapter five.

The results of the various measurements are summarized in Chapter six. It contains the measurement of the energy storage device, the EHS and the mote itself.

The results are discussed in Chapter seven. It contains a summary and the conclusion of this master's thesis. Possible future work can be found in this Chapter, too.

Finally, the complete circuit diagrams of the EHS and of the mote and a hardware illustration can be found in the appendix.

2 Related Work

This Chapter deals with the existing work on river level monitoring, WSNs and EHSs. First, a general overview about rivers and river monitoring is given in Section 2.1. In addition, different methods to measure the river level are explained. Then, different state-of-the-art WSN projects are shown in Section 2.2. Section 2.3 deals with existing hardware of wireless sensor networks. Section 2.4 shows different aspects of the software for wireless sensor networks. Finally Section 2.5 shows different possibilities for harvesting energy from the environment and the storage of this energy.

2.1 River Monitoring

River monitoring is important for the civilization around the river. The water level is needed to control hydroelectric power plants [29] and to predict flood disasters . A monitoring of flood disasters [52] is used to study the impact of floods on human life [50]. The monitoring of floods is also needed for flood management [35].

River level monitoring systems can be categorized dependent to their applications. Measurements have been done at great rivers in the world for hundreds of years. The water mills needed a maximum height of the tail water in order to operate correctly. The next mill downstream must ensure a maximum height of the river level. Therefore, water level measurements are used for legitimate control. Especially in flood prone areas, periodical measurements have been done with a gauge board very early. These measurements are needed to forecast the next floods. The river height can be read directly by a person. Today the measurements are done automatically by floaters, pressure transducers, radar and ultrasonic devices.

A river level monitoring system is described in [30], which measures the current river level using GPS receivers. The system consists of a river buoy equipped with a GPS receiver, a GPS antenna, a communication unit and other sensors. These sensors are used to correct the measured height and consist of a pressure transducer and a tilt sensor. The buoy is powered by a battery. The system also uses a reference receiver that is based on the riverbank. This receiver is used to correct atmospheric disturbances and should be placed near (few tens of kilometers) the receiver in the buoy. Such a correction system is called differential GPS as described in [31] and is shown in Figure 2.1. The position and height information of the buoy receiver and the reference receiver are sent to a central facility. This system was tested aground incipiently. The reference receiver was placed on a building and the buoy receiver was placed on a hanging platform. This platform can swing around and move up and down since an elastic cord was used. The expected accuracy is in the range of a few centimeters. First tests have shown that this accuracy can be reached, during steady phases. The system was also tested by measuring a river level. The long-term average of the measured river level has an accuracy of a few millimeters. The reference receiver was placed near the measurement receiver and the

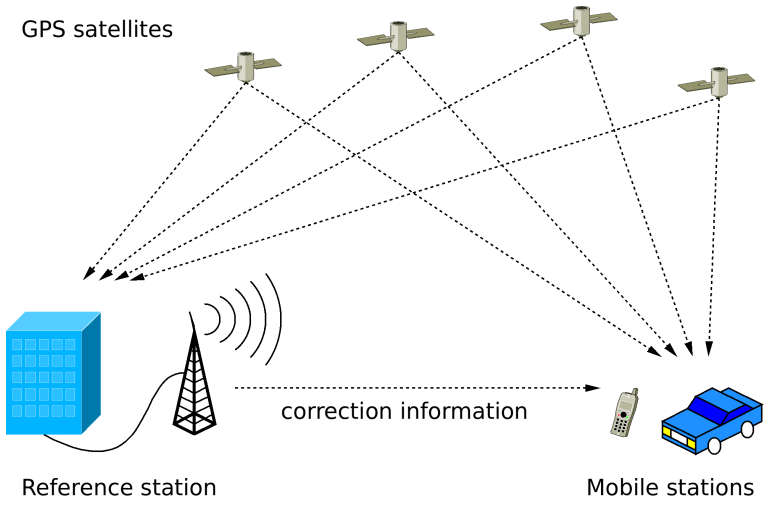

Figure 2.1: Differential GPS system architecture modified from [31].

data was recorded over three hours. Single measurement values have an accuracy of a few centimeters. Therefore, GPS is suitable to monitor water levels.

Another method to determine the river level is introduced in [14]. GumStix embedded computers are used for processing images of a river. They are equipped with 802.11b and a low-power radio module. The hardware is powered with solar cells and high-capacity batteries. One node has a power consumption of up to 3W. Cameras are used to detect the rate-of-flow of the river. The image processing is done locally on the nodes. The images can be distributed to other nodes to enhance the accuracy of the system. It exploits local computation to enhance the performance. Therefore, an "*adaption of WSN behavior based on awareness of environmental conditions such as flood data and power monitoring*" can be performed [15].

2.2 Wireless Sensor Network Projects

There are many different applications for wireless sensor networks. An overview of some WSN projects is shown in [40]. Only projects related to environmental monitoring are relevant for this master's thesis. Therefore, only such examples are discussed here.

For example, there is a WSN for monitoring the sub-glacier environment [24]. The motes are equipped with temperature, pressure and tilt sensors. These nodes are supplied via drill holes into the glacier. The batteries cannot be changed during operation. Another example is a WSN that is used to monitor the impact on the surrounding environment of a wind farm off the coast of England. The nodes are fixed on the ocean bed by an anchor. The nodes are equipped with several sensors for measuring temperature, pressure, current, conductivity and turbidity. They are able to form a self-organized network. The communication is done by a module that is fixed over the sea-level onto a buoy. A system overview is given in Figure 2.2.

Some volcanoes are also supervised by a WSN as introduced in [48]. The nodes are

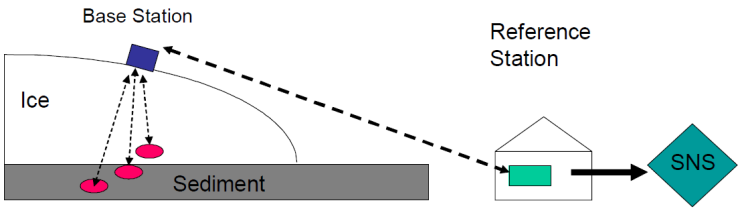

Figure 2.2: System overview of the Glaceweb from [24].

equipped with an infrasonic sensor and are synchronized with a reference node with GPS connection. The GPS data can be used for synchronization. It contains a very accurate time stamp. Therefore, all motes can use their GPS module for time synchronization. The logged data from the different motes must be synchronous to allow a prediction of a volcanic eruption. One node has a long-distance radio module. All the measured data from the other nodes is transmitted to this node. It forwards the data to a base station at an observation post.

2.3 Wireless Sensor Node Hardware

The hardware of a mote consists of a measuring unit, which measures specific values of the environment, a processing unit that processes the measured data, a communication unit that is used for transmitting the data and a power unit that supplies the other units. A generic structure of a mote can be seen in Figure 2.3. The original structure from [37]

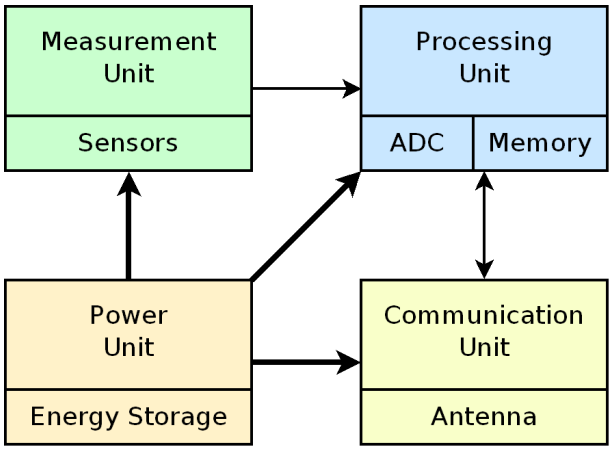

Figure 2.3: Generic structure of a mote modified from [37]. The thin lines represent the internal data information flow and the thick lines represent the power flow.

has been modified. Some state-of-the-art motes have an integrated antenna, e.g. TelosB. Almost all motes use microcontrollers with integrated analog to digital converters (ADCs).

There are many different motes on the market. In addition, schematics of some motes

are available online e.g. Mica2 and TelosB. The mote TelosB uses the MSP430F1611 microcontroller from Texas Instruments®. This microcontroller has very low power consumption and many integrated components such as an ADC and serial interfaces. An overview of state-of-the-art motes is shown in Table 2.1.

Sensor Node	Microcontroller	Communic.	Power Consumption [mW] (active/receiving/sending)
Crossbow Mica2	ATmega128	CC1000	33 / 62 / 89
Crossbow TelosB	MSP430	CC2420	3 / 41 / 41
ITRI ZBnode	ARM 720T	CC2420	140 / 202 / 202
Dust Networks Mote2020	MSP430	CC2420	-/-/-

Table 2.1: Overview of state-of-the-art WSN nodes [36, 22]. The column power consumption shows the active power of the microcontroller, the needed power for receiving and the power consumption of the mote during sending with maximum power.

For providing proper functionality of a WSN node placed in a river, the nodes have to be water-tight. In addition, different environmental factors must be considered such as high temperature differences, ice on the river and flotsam. A WSN for monitoring coral reefs is introduced in [5]. The system consists of a water-tight housing with an MSP430 microcontroller, a lithium battery pack, a wireless subsystem and some sensors (temperature, light, pressure, conductivity and pH) inside. The hardware is shown in Figure 2.4.

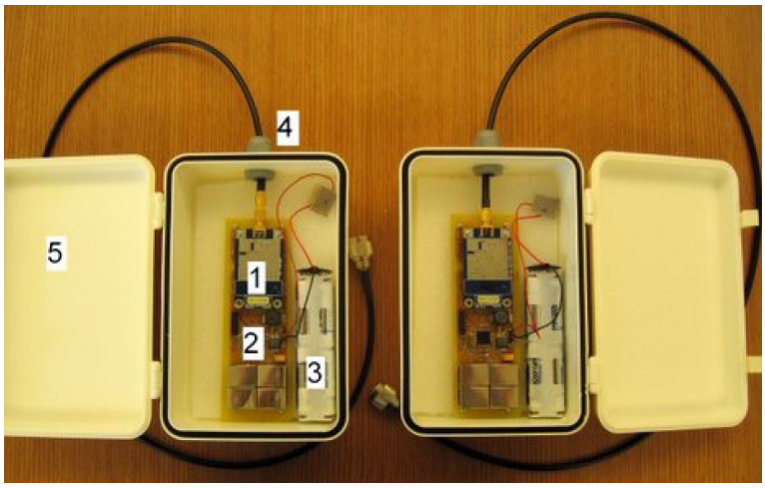

Figure 2.4: Watertight mote from [5].

The communication under water is very complicated. Low-cost radio chips use frequencies that are attenuated heavily under water [47]. There are other techniques, for example ultrasonic or optical communication. Ultrasonic communication has the advantage of very high distance coverage. The significant disadvantage is the slow propagation speed of the

sound waves compared to an electromagnetic wave. An acoustic modem is also very expensive (3000 $) and has a slow data rate (5 kbit/s). The optical communication has the advantages of higher data rates and cheaper devices. Hence, the range of such a communication device is only about a few meters in clear water.

2.4 Wireless Sensor Node Software

WSNs are error prone, because of the influences of the harsh environment. Therefore, the software of a WSN must be fault-tolerant and dependable. For example, the WSN must not fail if one mote cannot complete a measurement.

Power aware tasking is important for environmentally powered sensor networks [18]. An analytical energy harvesting model is introduced, which describes the available power of the EHD, the energy storage device and the consumer. This model is described in detail in Section 2.5.2. If the average power available to the system is lower than the consumed power the system cannot operate perpetually. The software must notice this fact and choose a low enough duty cycle. So a regularly system functionality can be ensured.

The duty cycle of the nodes leads to another problem. Each node must be synchronized with all other nodes. Otherwise the communication will not work. If one node is not synchronized, the data cannot be sent to this node. The whole system must wait for this node and waste a lot of energy. A method for time synchronization with extreme temperature conditions is explained in [39]. A Sliding Clock Synchronization (SCS) is used for keeping the motes synchronized. One node transmits two consecutive beacons. The other nodes receive these beacons and calculate the time difference between them. Therefore, they can determine their own error and correct them.

Topology control is also important for a WSN as mentioned in [42]. To provide a successful delivery of the data from every node to another node, the whole network must be connected. It is sufficient to reach the next hop. Problems can occur if a node fails. Transmission power control can be used in such situations. If the next node has failed, the transmission power could be increased to reach the next but one. Also the routing mechanisms can be tuned to power awareness [7, 51]. So-called anycasts are suitable for power aware WSNs [42]. Here only one node will forward data packets towards the sink. This saves a lot of energy because the sink does not receive duplicated packets.

A power aware routing mechanism is introduced in [51]. Figure 2.5 shows an example of power aware routing. A threshold value is introduced to limit the maximum distance (maximum transmission distance). This value influences the topology of the WSN. Such an algorithm should be combined with a transmission power control to save energy.

Hardware abstraction is needed to be able to run the same application on different hardware platforms. Figure 2.6 shows the hardware abstraction of TinyOS. The hardware abstraction is split into three different layers. The first layer is the hardware presentation layer (HPL). This layer is used for direct access to the hardware via memory or port mapped I/O. The hardware signals occurring events with interrupts. The second layer is the hardware abstraction layer (HAL). This layer uses the HPL to build a meaningful abstraction of the hardware. Therefore, the complexity can be hidden. The third layer is the hardware interface layer (HIL). It provides hardware independent interfaces by using the platform specific HAL interfaces. [12]

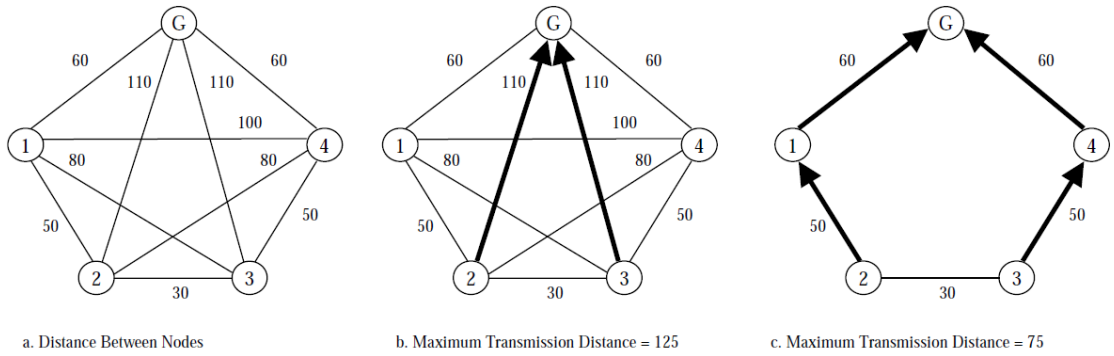

Figure 2.5: Power aware routing example from [51]. (a) Distance between the different motes. (b) Transmission according to a minimum number of hops routing algorithm and a maximum transmission distance of 125. A direct transmission and higher energy costs for the sending nodes are the results. (c) Transmission according to a minimum number of hops routing algorithm and a maximum transmission distance of 75. Lower energy costs but a higher latency are the results.

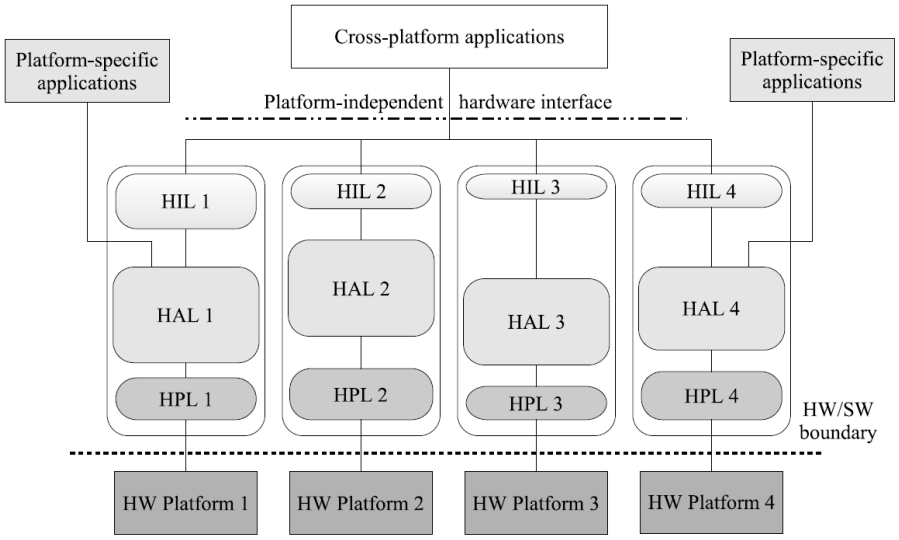

Figure 2.6: Hardware abstraction architecture of TinyOS from [12].

2.5 Energy Harvesting Systems

The lifetime of each normal battery is finite. As mentioned in [10] a single AA battery with a capacity of 2.6 Ah has a leakage current of 30 μA. The lifetime of a battery-powered mote versus the power consumption is shown in Figure 2.7.

Therefore, energy harvesting is vital for a perpetual mote. It must harvest enough

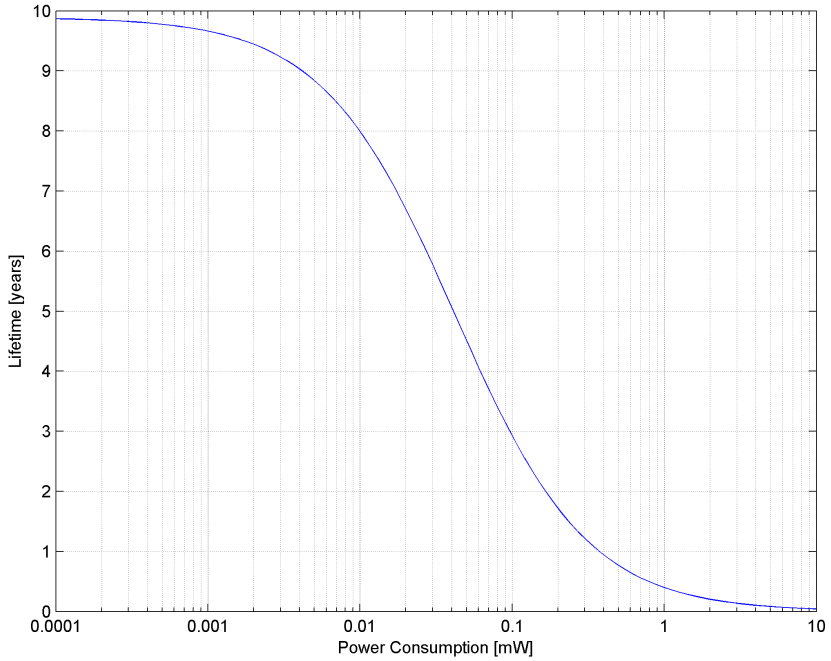

Figure 2.7: Lifetime of a battery-powered mote versus average power consumption using a simple battery model of a single AA cell (NiMH) with 2.6 Ah and a leakage current of 30 μA. [10]

energy from the environment. There are several different types of environmental energy source, which can be used for such systems [42]. Table 2.2 shows a list of different energy harvesting technologies and the expected output power density [38]. It can be seen that the

Harvesting technology	Power density	Demand for 10 mW
Solar cells (outdoor at noon)	15 mW/cm^2	0.667 cm^2
Piezoelectric (shoe inserts)	330 $\mu W/cm^3$	30.3 cm^3
Vibration (small microwave oven)	116 $\mu W/cm^3$	86.2 cm^3
Thermoelectric (10°C gradient)	40 $\mu W/cm^3$	250 cm^3
Acoustic noise (100dB)	960 nW/cm^3	10417 cm^3

Table 2.2: Power densities of different harvesting technologies [38]. The third column shows the required area or space of the theoretical EHD to supply a mote with a power consumption of 10 mW.

power density of acoustic noise is very low. To supply a mote with a power consumption of 10 mW, a large EHD is needed. Therefore, it is not suited to supply motes. The other technologies can be used to supply motes. Especially the solar cells provide a high power density. They are used very often to supply motes. Typically, a solar energy harvesting module is used to store and convert the energy of the solar cells.

The design and the development of such a module are described in [38]. This module is

connected to a Mica2 mote and is called Heliomote. It is mentioned that the deployment of a node is more expensive than the node itself. So it is suitable to use EHS for a longer lifetime. Solar cells are the most effective power sources refering to the physical size of the EHD. A solar cell has been characterized and it behaves as a voltage limited current source. The characterization is done with a U-I diagram and the main parameters of a solar cell are the open circuit voltage (U_{oc}) and the short circuit current (I_{sc}). The open circuit voltage is the voltage at a current of $0\,A$ and can be found at the intersection of the U-I curve with the voltage axis. The short circuit current is the current at a voltage of $0\,V$ and can be found at the intersection of the U-I curve with the current axis. An example U-I diagram is shown in Figure 2.8. There is an optimal operating point with a maximum

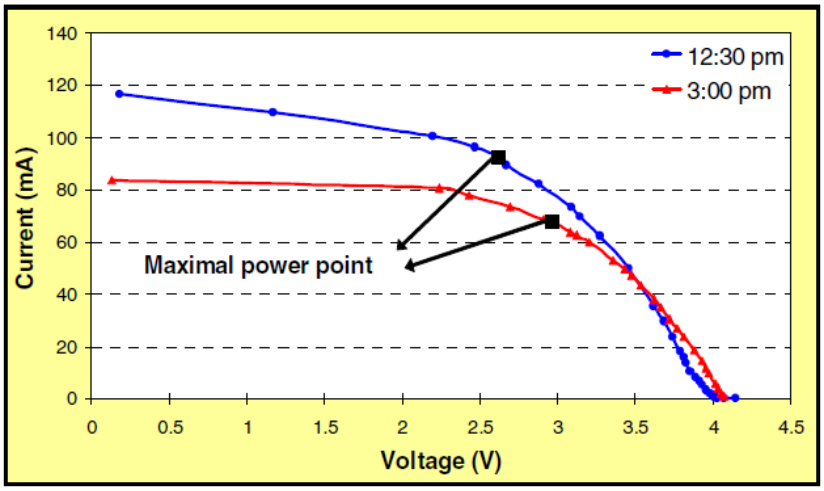

Figure 2.8: Measured U-I diagram of a solar cell from [38].

of output power at a certain current and voltage. The optimal operating point varies with the amount of incident solar radiation but the open circuit voltage remains nearly constant. The solar cell is connected to a rechargeable battery directly. This provides a voltage of the solar cell close to the optimal point if the battery is charged. This method is very easy and cheap. The solar harvesting module monitors the voltage of the battery and prevents overcharge and undercharge of it. The module provides a constant output voltage of $3\,V$. Therefore, a step up DC-DC converter is used. Measurement results have shown that the Heliomote can be powered successfully by the developed solar harvesting module.

An adaptive system for optimal solar energy harvesting has been introduced in [2] to gain the maximum power out of a solar cell. The advantage of such systems is the optimal energy harvesting. The disadvantage is a more complex and more expensive circuit compared to a direct charge of the energy storage device.

A long-duration solar-powered WSN is introduced in [9]. This system uses a Fleck1 mote and two NiMH rechargeable batteries to store the energy of the solar cell. It is also shown that a DC-DC converter is important for a longer power supply of the mote. The converter exhausts the batteries and provides a constant output voltage. This provides an up to three times longer operational time of the mote. An ultra-capacitor is also mentioned

as energy storage device. In comparison to two AA NiMH batteries, a $50F$ ultra-capacitor has only 0.4% of the batteries capacitance. A WSN, consisting of 15 motes, has been realized, which monitors the environment. The available solar power has been tracked over more than 250 days.

The prediction of the available energy is a nice feature of an EHS. It is important for motes, because so they should stay in an energy-neutral operation [17]. This means that the energy consumed by the mote is less than the harvested energy. Some algorithms for harvested energy prediction are explained in [3]. A weather conditioned moving average has been introduced and some tests have been done with solar cells as EHDs. The available power of the last few days is saved in a matrix. This matrix is used for solar energy estimation. The current available power and the values stored in the matrix are used to predict the power.

2.5.1 Energy Storage

Normal batteries are not useful because of the battery replacement problem described in [28]. An enormous amount of dead batteries has to be replaced in a long lifetime WSN.

Energy storage devices are vital for perpetual motes. The energy must be stored for hard times. For example, no energy can be harvested with solar cells during darkness. Therefore, it must be stored. Rechargeable batteries or ultra-capacitors can be used to bridge periods without harvested energy.

The common problem of all rechargeable batteries is the capacity fade with increasing charge-discharge cycles. Figure 2.9 shows the capacity fade over the number of charge-discharge cycles [23] of a simulated lithium ion battery. It can be seen that the end of charge voltage is important for the capacity fade. Further important factors are the charge current and the depth of discharge (DOD).

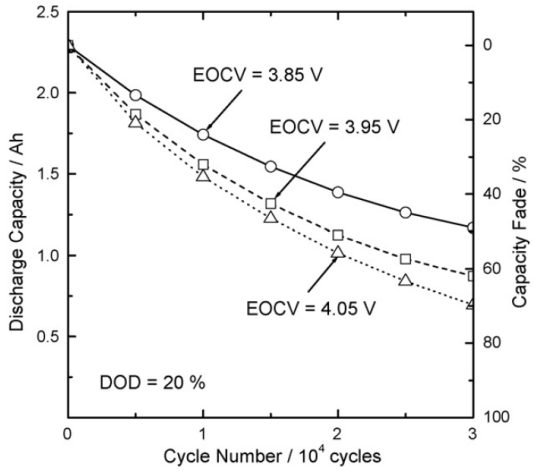

Figure 2.9: Capacity fade over the number of charge-discharge cycles of a simulated lithium ion battery. Three different end of charge voltages (EOCV) are simulated. [23]

In addition, the aging of lithium ion batteries is a known problem. Figure 2.10 shows the aging of a standard industry cell and a prototype cell at various storage temperatures.

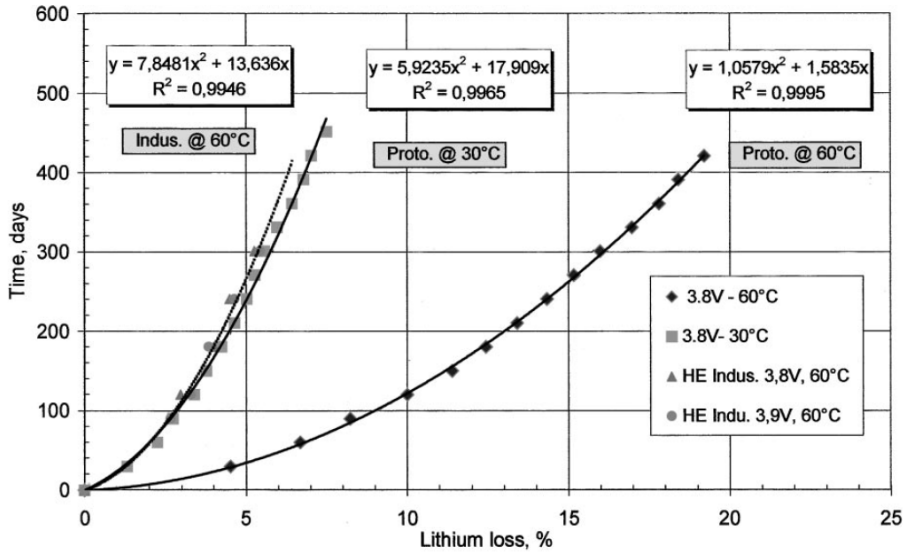

Figure 2.10: Capacity loss of lithium ion batteries over time. [6]

There are also other methods to store energy. In [16] it is shown that the energy can be stored in one ore more ultracapacitors. To ensure a guaranteed minimum of lifetime a primary battery is needed. This battery can not be charged but must be used, because the energy from the environment is generally unpredictable, discontinuous and unstable. It has been shown that the longest lifetime can be achieved if the primary battery is decoupled from the power consumer.

2.5.2 Energy Harvesting Model

A theoretical energy harvesting model is introduced in [18]. The model deals with the description of environmental energy sources and the energy sink (consumer). The model bases on the following definition.

Definition: *(ρ, σ_1, σ_2) - source: Suppose $P(t)$ is a continuous and bounded function of a continuously varying parameter t. $P(t)$ is said to be a (ρ, σ_1, σ_2) - source if and only if for any finite real number T, it satisfies* [18]:

$$\int_T P(t)dt \geq \rho T - \sigma_1$$

$$\int_T P(t)dt \leq \rho T + \sigma_2$$

Figure 2.11 shows a graphical description of this model.

The (ρ, σ_1, σ_2) - source model can be used to describe environmental energy sources. $P(t)$ is the continuous power output of the source at the time t. ρ is the average power output of this source. σ_1 and σ_2 describe the changes of the power output. The power

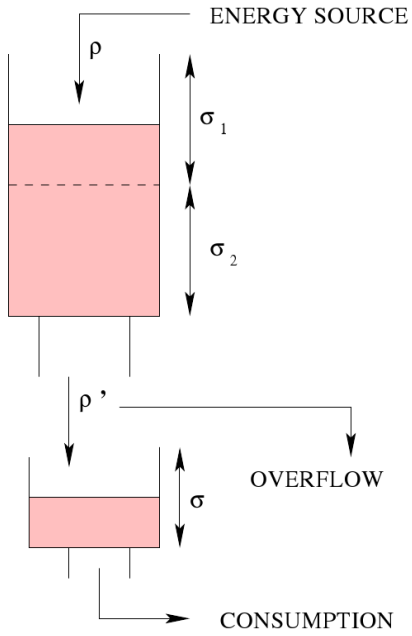

Figure 2.11: Theoretical energy harvesting model [18].

consumption is also characterized with the average power consumption ρ' and the maximum power consumption σ. It is called (ρ', σ) - consumer. The following theorem has been proven in [18]:

Theorem: *Sustainable Performance at Eternity (Variable Consumption Profile): If a (ρ', σ) - consumer device is powered by a (ρ, σ_1, σ_2) - source model, has an energy storage capacity of $\sigma + \sigma_1 + \sigma_2$, and $\rho' < \rho$, then the device can operate forever.*

2.6 Summary

A lot of related work has been analyzed in this Section. First, the possibilities for river monitoring have been discussed. Differential GPS can be used to determine the current river level. Then, several WSN projects and WSN hardware platforms have been introduced. There are for example WSN solutions to monitor the sub-glacier environment or volcanoes. The requirements for WSN software have been shown briefly. Key feature of the wireless sensor software is power awareness including duty cycling, synchronization, topology control and transmission power control. Finally, different EHS have been discussed. It has been shown that normal batteries cannot be used for perpetual operation. In addition, the capacity loss of normal batteries is a problem for environmentally powered motes. Now the concept of the battery-less WSN platform for river monitoring can be developed. In addition, the components of this platform can be selected to ensure proper functionality.

3 Design of the Wireless Sensor Platform

This Chapter deals with the different aspects of the development of a battery-less WSN river monitoring platform. There are different possibilities to realize such a monitoring platform. It can be placed in a buoy floating on the river or placed in a water-tight box on the ground of the river. Another possibility was introduced in Section 2.1. There, cameras are used to detect the water level and the flow rate of a river.

Many different factors must be taken into account, e.g. lifetime and costs. These factors are discussed in the following Sections and the appropriate components will be selected.

3.1 Component Selection

First of all, the fundamental principle of river monitoring must be chosen for the component selection. It is better to use more than one sensor for a measurement, because inaccuracies and failures of a sensor can be compensated. Therefore, three complete different methods have been chosen:

- Water pressure measurement
- Ultrasonic distance measurement
- GPS heighting

The water pressure transducer must be placed on the riverbed and so it measures the hydrostatic head. Therefore, the mote must also be placed on the ground or it must be connected with a cable. The position of the sensor is important because it should be near to the deepest point of the riverbed. If it is placed there, the real water height can be determined easily. To ensure an accurate measurement, the surrounding air pressure must be measured too. Then, the pressure value measured at the ground can be corrected. The following calculation will show the error of air pressure fluctuations if no correction is performed. The average sea-level pressure is 1013.25 $mbar$ and the maximum measured pressure in Germany was 1056.6 $mbar$ [49]. The difference is:

$$P_{diff} = 1056.6 - 1013.25 = 43.35\ mbar$$

The pressure under water is $p = 98.0665\ mbar/m$. Now the difference of two measurements at average sea-level pressure and at the highest pressure can easily be calculated with:

$$h_{diff} = \frac{P_{diff}}{p} = \frac{43.35\ mbar}{98.0665\ mbar/m} = 0.442m$$

That is only the difference between the average and the maximum value. The difference between minimum and maximum is still higher. Therefore, it can be seen clearly that a correction of the pressure is necessary for an accurate water level measurement.

An ultrasonic distance sensor can be used to determine the water level of the river. The sensor can be placed on the bottom of a buoy. Therefore, it can emit the ultrasonic waves directly into the river. The sound waves will be reflected from the riverbed and can be measured at the ultrasonic sensor. A possible tilt of the buoy does not disturb the measurement if the angle of the emitted waves is high enough. Larger stones in the riverbed can influence the measured water level. The important factor is the fluctuation of the river level and this can be measured with the ultrasonic sensor, too. To get a precise measurement, the temperature of the water must be measured. The temperature has an influence on the speed of the sound in water. The dependency of temperature and speed of sound is shown in [8].

GPS heighting for measuring the water level of a river was introduced in [30]. Therefore, each mote must be equipped with a GPS receiver. This receiver must be placed on the surface of the river. A buoy that is stick to the riverbed or the bank of the river is suited well. In addition, a reference station is needed to correct the disturbances.

Since two of three measurement methods need the placement at the surface of the river, the hardware components of the platform will be placed there. This reduces the effort of wiring the sensors to the mote and therefore the cost of a RiverMote. The hardware is placed into a buoy, which is streamlined. So the buoy always heads into float direction. It can be attached to the ground with a cord. An anchor can be used to fix the postion of the RiverMote. A pressure transducer attached to the anchor could measure the water level.

The following Sections describe each hardware component in detail.

3.1.1 Pressure Transducer

The pressure transducer must be able to detect changes of the river level. To detect changes of $1\,cm$, the following accuracy is necessary:

$$\Delta p = 98.0665\,mbar/m \cdot 0.01\,m = 0.98\,mbar$$

The range of the pressure transducer should be large enough to use it in most rivers. Therefore, it should be able to measure the pressure up to $10\,m$ water depth. It equates to a pressure of $0.98\,bar$.

3.1.2 Ultrasonic Sensor

The ultrasonic sensor must be water-tight, too. It emits the sound waves into the water. Therefore, it is placed on the bottom of the buoy. In most commercial systems, a dedicated sender and a dedicated receiver are used. This ensures an easy measurement of the reflected sound waves. There is also the possibility of the measurement of the distance with a combined sender and receiver. The problem is the distinction of the sent signal and the received signal. Measurements should show if a distance measurement is possible with only one transceiver.

3.1.3 Communication

The communication under water is a difficult problem. Ultrasonic communication is used in open water but is not tested in rivers. In addition, the power consumption and the cost

of such systems are too high. Therefore, an RF communication module must be mounted above the river surface. This can be done easily since the hardware of the RiverMote is placed into a buoy.

A complete RF module reduces the development time and costs. Therefore, the 2.4 GHz IEEE 802.15.4 transceiver module MRF24J40MB from Microchip®is chosen. The module integrates a crystal, an internal voltage regulator, a matching circuitry, a power amplifier, a low noise amplifier and a PCB antenna. The module can operate within a voltage range from $2.4\,V$ to $3.6\,V$ and has a current consumption of $25\,mA$ at receiving and $130\,mA$ at sending (maximum power). The normal supply voltage is $3.3\,V$. This is very common in low-power applications and is supported by many other hardware components as well.

This RF module supports a range of up to $1200\,m$. Obstacles will reduce the range in the real environment. Therefore, the maximum placement density is one node per $500\,m$.

3.1.4 GPS

There are cheap GPS receiver modules, which can be used for the RiverMotes. One of the most import properties of the GPS receiver module is a low power consumption. There are also different supply voltages at the different modules. To ensure an easy integration in the mote, the supply voltage should be $3.3\,V$. To save power the modules should support something like a standby mode. Some modules have a backup battery that is used to keep the current state if the power is cut off. Other modules offer a special pin that must be supplied with a backup voltage. These modules can be turned off from the supply voltage and save their state via the backup supply. Some modules have an integrated GPS antenna. This saves money and the integration of the module is very easy because it is small and a special fixing of the antenna can be omitted. Therefore, the module should be mounted inside at the top of the buoy. This provides a maximum of connectivity and saves power. The material of the buoy must be appropriate for this purpose. No shielding materials such as metal must be used. Typical power consumption at a supply voltage of $3\,V$ is about $100\,mW$. The modules are usually equipped with a serial interface. This interface has a CMOS compatible voltage range. It can easily be connected to a serial interface of the microcontroller.

3.1.5 Microcontroller

The microcontroller is the main component of a mote. It must support enough computational power without consuming too much energy. Therefore, a low-power microcontroller should be used. There are special microcontroller designs for such requirements. The integrated peripherals are also important because in such embedded systems no further peripheral chips should be used. This would only increase the costs and the complexity of the hardware. The microcontroller should have for example an ADC and serial interfaces.

The programming of the mote should also be very easy. In the last years TinyOS was used to program motes. Therefore, TinyOS should be portable to the developed hardware. To keep this process as easy as possible, a microcontroller is used that is already supported by TinyOS. The design is similar to the design of the TelosB mote from Crossbow Technology®shown in [46]. The MSP430F1611 ultra low-power microcontroller from Texas Instruments®is used. The average power consumption of this microcontroller

is about $15\,mW$ at a voltage of $3.3\,V$ and a frequency of $8\,MHz$. It is based on a 16-bit RISC architecture [45].

The programming process of the microcontroller itself can be performed in different ways. First, there is a special debugging interface called JTAG. This interface can be used to program all memory of the microcontroller. The second possibility is the programming via a serial interface.

3.1.6 Power Supply

The battery-less mote must harvest enough energy from the environment. It operates outside on the surface of a river. It is exposed to the daylight every day. A solar EHD is also the most effective one as shown in Table 2.2. The other EHDs are too expensive and ineffective. A little generator using the flow of the river has been considered, too. The problem of such a system is that the propeller can be blocked by any flotsam. The node has no energy source and the blocking material must be removed manually. Therefore, a solar cell is used to harvest the energy for the mote. The needed size and consequently the output power depend on the power consumption of the whole hardware. The power estimation can be found later in Section 3.3.

3.1.7 Energy Storage

There are mainly two possibilities to store the electrical energy. First, the energy can be stored in a rechargeable battery and second it can be stored in an ultracapacitor. Batteries have much more capacity compared to the ultracapacitors. The disadvantages of the batteries are the reduced lifetime and the temperature dependencies. An ultracapacitor has typically 500000 charge-discharge cycles and a nominal lifetime of 10 years. If both values are below the limits, the maximum capacity loss is 80 % of the nominal capacity [26]. A rechargeable battery has a much shorter cycle lifetime. For example, a NiMH battery has only a lifetime of 500 charge-discharge cycles with a maximum capacity loss of 80 % [38].

It can be assumed that energy can be harvested during the day. Therefore, the energy consumed during the night must be stored in the energy storage device. This is only a short time and can be bridged with an ultracapacitor. The needed capacity depends on the power consumption of the whole hardware.

The energy stored in a capacitor can be calculated with:

$$E = \frac{1}{2} \cdot C \cdot U^2$$

The voltage U has a quadratic effect on the storable energy. Usually ultracapacitors have a very low nominal voltage. Therefore, two ultracapacitors can be connected in series. The resulting capacity will only be half the capacity of a single capacitor. However, the nominal voltage will double and this has a higher effect on the overall storable energy:

$$E = \frac{1}{2} \cdot \frac{C}{n} \cdot (U_C \cdot n)^2$$

This formula shows the storable energy of a serial connection of n equivalent capacitors. U_C is the nominal voltage of a single capacitor and C is the capacitance of a single capacitor.

The formula can be reduced to:

$$E = \frac{1}{2} \cdot C \cdot n \cdot U_C^2$$

It can be seen that the number of capacitors connected in series has direct influence on the storable energy.

Due to the advantages of ultracapacitors concerning the lifetime, they will be used as energy storage devices.

3.2 Activation Interval

To save energy, the whole system will only be activated for a certain fraction of time. The system will enter a sleep mode after all results are calculated and the communication is done. The activation interval is needed for the power estimation. An interval of $T = 15\ min$ is assumed here.

It is important to know the flow velocity of the river for determining an appropriate activation interval. The flow velocity depends on the riverbed surface, the incline of the river, the width of the river, and the discharge. The surge propagation speed is also important for the activation interval. An example value of the surge propagation speed is given in [13]. Ice blocks the river at certain position each year. A surge is released when this blocking is bursting. The river in this example has an average discharge of $500\,m^3/s$. The propagation speed of such a surge is $1.8\,m/s$. In the following, an average flow velocity of $v = 2\,m/s$ is assumed.

Now the propagation of an interval can be determined with:

$$l = T \cdot v = 900s \cdot 2m/s = 1800m$$

If the motes are placed in a distance of 1 km a surge will cover two motes in one activation interval. Because many motes are placed along the river, it would be possible to monitor the river height in an adequate resolution.

3.3 Power Estimation

In this Section, the overall power consumption of the mote will be estimated. Table 3.1 shows a list of the needed component of a mote. Figure 3.1 shows an overview of the calculation process done in this Chapter.

The name of the component can be found in column one. The activation time of each component t_a is given in the second column. The duty cycle D of each component can be calculated with the activation time and the activation interval T as follows:

$$D = \frac{t_a}{T}$$

The results are shown in column three. The power of each component in the active mode and the sleep mode are shown in column four and five. The average power consumption of each component during the activation interval can be found in the last column and is calculated with:

$$P_{avg} = D \cdot P_a + (1 - D) \cdot P_{sl}$$

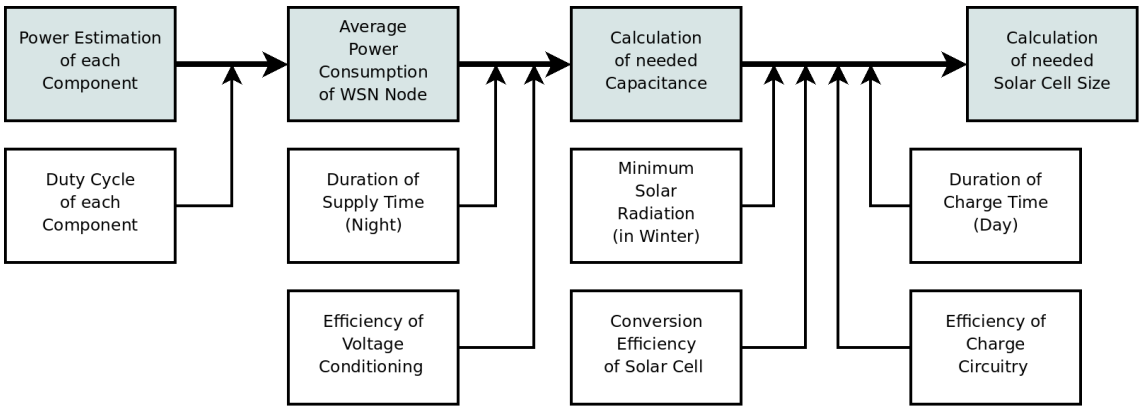

Figure 3.1: Overview of the calculation process.

Component	t_a [s]	Duty Cycle	P_a [mW]	P_{sl} [mW]	P_{avg} [mW]
Microcontr. MSP430F1611	30	0.033	15.0	0.1	0.60
MRF24J40MB Send	2	0.002	429.0	0.0	0.95
MRF24J40MB Receive	28	0.031	82.5	0.0	2.57
MRF24J40MB Sleep	30	0.033	0.0	0.1	0.10
GPS Fastrax UP300	30	0.033	120.0	0.1	4.10
Pressure Transducer	1	0.001	250.0	0.0	0.28
Ultrasonic Sensor	1	0.001	10.0	0.0	0.01
Other Hardware	30	0.033	30.0	0.1	1.10
Total Power P_{tot}					9.70

Table 3.1: Power estimation of the different components. The RF-module can be found in three different columns. This is necessary to model different sending and receiving times. The pressure transducer and the ultrasonic sensor will be switched off completely. Therefore, they have a power consumption of zero during sleep state . An activation interval of 15 min is assumed here.

During full operation mode, all components are active. This means that the mote consumes a power of $P_{max,full} = 854\ mW$ and the current can be calculated with:

$$I_{max,full} = \frac{P_{max,full}}{U_{sup}} = \frac{854mW}{3.3V} = 258.8\ mA$$

This current must be supplied by the voltage conditioning unit. Finally, the estimated total average power consumption of the mote is shown at the bottom of the Table and is 9.7 mW. For further calculation a higher value of $P_{tot} = 12\ mW$ will be assumed.

3.3.1 Power Consumption vs. Activation Interval

Figure 3.2 shows the power consumption of the mote depending on different durations of the activation interval. The calculations have been done with the power estimation shown

in Table 3.1. It can be seen that the average power consumption of the mote can be

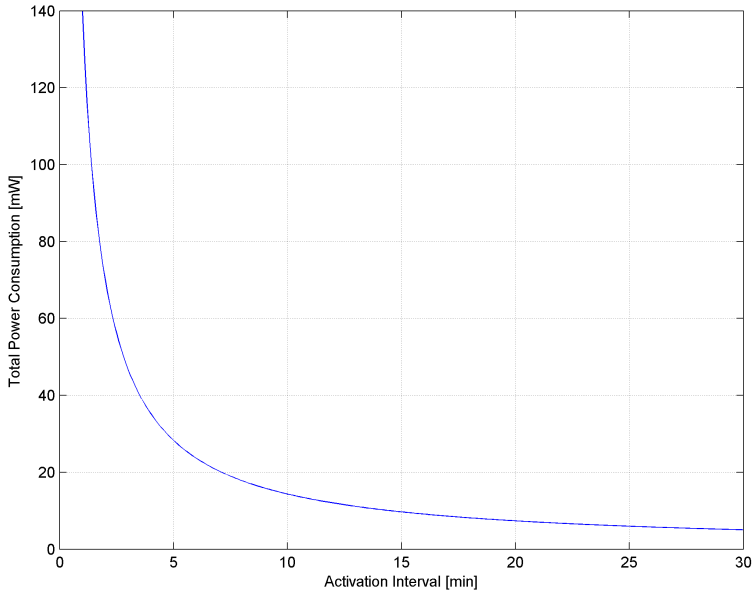

Figure 3.2: Power consumption dependent on the duration of the activation interval (from 1 to 30 minutes).

influenced by the activation interval. The mote itself can determine a proper activation interval. So an energy-neutral operation can be achieved and the mote can operate forever. Therefore, the measurement of the consumed power is necessary.

3.3.2 Energy Storage Device

Now the needed capacity of the energy storage device can be determined. The night must be bridged with energy. The longest night is during midwinter. Austria is south of the 49th latitude. The longest night lasts for about 15 hours and 40 minutes and is assumed as $t_{night} = 16\,h$ for further calculations.

During 16 hours, the mote will consume the following amount of energy:

$$E_{supply} = P_{tot} \cdot t_{night} = 12mW \cdot 16h = 691.2\,J$$

The energy stored in the capacitor must be converted to supply the mote. This conversion is not lossless and an efficiency of $\eta_{convert} = 80\%$ is assumed. Now the energy that must be stored in the capacitor can be calculated:

$$E_{needed} = \frac{E_{supply}}{\eta_{convert}} = \frac{691.2J}{0.8} = 864\,J$$

As mentioned before, it is better to connect capacitors in series to increase the storable energy. In this project, two capacitors will be connected in series. A typical nominal voltage of an ultracapacitor is $2.5\,V$. Therefore, the resulting nominal voltage is $U_n = 5\,V$.

Now the capacity of the capacitor can be calculated with:

$$C_{ideal} = \frac{2 \cdot E_{needed}}{U_n^2} = \frac{2 \cdot 864J}{(5V)^2} = 69.12\,F$$

The converter cannot discharge the capacitor completely. A rest voltage will remain in the capacitor. The converter can operate down to a voltage of $1.8\,V$. The remaining energy must be considered for the capacity calculation:

$$C_{real} = \frac{2 \cdot E_{needed}}{U_{start}^2 - U_{stop}^2} = \frac{2 \cdot 864J}{(5V)^2 - (1.8V)^2} = 79.41\,F$$

It can be seen that the increase of the capacity is low compared to the value of the remaining voltage.

In this project, an ultracapacitor called Boostcap®with a nominal voltage of $2.5\,V$ and a capacity of $310\,F$ is used. Figure 3.3 shows two of the ultracapacitors. Two of them are connected in series. This provides a usable energy of

$$E_{usable} = \frac{1}{2} \cdot C \cdot \left(U_{start}^2 - U_{stop}^2\right) = 0.5 \cdot 155F \cdot \left((5V)^2 - (1.8V)^2\right) = 1686.4\,J$$

and a maximum power consumption of the mote of

$$P_{max} = \frac{E_{usable} \cdot \eta_{convert}}{t} = \frac{1686.4J \cdot 0.8}{16h} = 23.42\,mW$$

Figure 3.3: Maxwell®Boostcap®($310\,F$, $2.5\,V$).

The leakage current of ultracapacitors must also be kept in mind. The capacitor has a maximum leakage current of $0.45\,mA$. The maximum power loss can be calculated with:

$$P_{leakage} \leq I_{leakage} \cdot U_n = 0.45mA \cdot 5V = 2.25\,mW$$

Therefore, the usable maximum power of the mote is bounded by:

$$P_{tot,max} \geq P_{max} - P_{leakage} = 23.42 - 2.25 = 21.17\,mW$$

It can be seen that the maximum power is greater than the estimated power of the mote. Therefore, continuous operation is possible.

3.3.3 Solar Cell Calculation

In this Section, the power needed and consequently the size of the solar cell will be calculated. The energy stored in the capacitor must be provided by the solar cell during the day. The storing process of the energy supplied by the solar cell is not lossless. An effectiveness of $\eta_{charge} = 80\ \%$ is assumed here. The total power consumption of the mote yields to a total energy amount during a whole day (day and night) of:

$$E_{24h} = P_{tot} \cdot (t_{day} + t_{night}) = 12mW \cdot (8h + 16h) = 1036.8\,J$$

The efficiencies of the voltage converter and the storing process must be considered. In addition, the loss of the ultracapacitor $P_{leakage}$ must not be neglected.

$$E_{24h,leakage} = P_{leakage} \cdot (t_{day} + t_{night}) = 2.25mW \cdot (8h + 16h) = 194.4\,J$$

$$E_{24h,solar} = \frac{E_{24h}}{\eta_{charge} \cdot \eta_{convert}} + \frac{E_{24h,leakage}}{\eta_{charge}} = \frac{1036.8J}{0.8 \cdot 0.8} + \frac{194.4J}{0.8} = 1863\,J$$

The total power that must be provided by the solar cell during the day can be calculated with:

$$P_{solar} = \frac{E_{24h,solar}}{t_{day}} = \frac{1863J}{8h} = 64.69\,mW$$

This power must be provided by the solar cell also during a day with bad weather conditions.

A monthly-averaged horizontal daily extraterrestrial irradiation of $P_{D,avg} = 2120\,W/m^2$ at a latitude of 50° in December is mentioned in [32]. This value could be used if the power in the energy storage device will last for longer periods. Then some dark days could be balanced by sunny days. The converting coefficient of solar light into electrical power is about $\eta_{solar} = 10\,\%$. Therefore, the needed solar radiation can be calculated with:

$$P_{radiation} = \frac{P_{solar}}{\eta_{solar}} = \frac{64.69mW}{0.1} = 646.9\,mW$$

The area of the solar cell for a monthly-averaged irradiation can be calculated as follows:

$$A_{cell,month} = \frac{P_{radiation}}{P_{D,avg}} = \frac{562.5mW}{212mW/cm^2} = 3.05\,cm^2$$

A worst-case scenario must be considered, because the ultracapacitor can only store the energy needed for one night. The minimum solar radiation (power density) at a very cloudy and rainy day is about $P_{D,min} = 3\,mW/cm^2$ [41]. This is equal to a radiation of $30\,W/m^2$. The value is coherent with the diagrams on page 37 in [32]. Now the needed area of the solar cell can be calculated with:

$$A_{cell} = \frac{P_{radiation}}{P_{D,min}} = \frac{649.9mW}{3mW/cm^2} = 215.6\,cm^2$$

The resulting size of the solar cell is suitable to integrate it into the buoy. Therefore, a compact and robust system can be built.

3.3.4 Housing

The housing of the RiverMote must fulfill several requirements: First, it must be watertight, because it is placed in the river. Second, it must float on the surface of the river. Therefore, it must be lighter than water. Third, the top of the housing must be transparent, because the solar cell is placed inside of the housing. Fourth, the housing must be robust, because it must resist all the flotsam of the river. Fifth, the housing must be able to resist ultraviolet radiation.

3.4 Hardware Design

In this Section, the concept of the RiverMote will be discussed. Figure 3.4 shows the overall system concept with different components and their interaction.

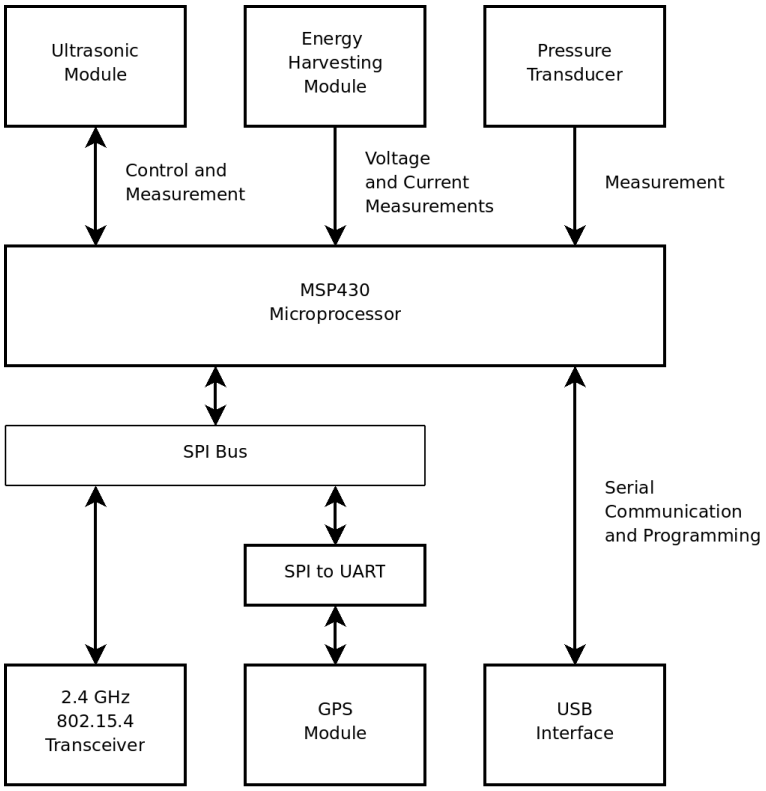

Figure 3.4: The concept of the hardware components and the communication between the modules is shown.

The main component of the mote is the microcontroller. The MSP430F1611 from Texas Instruments®low-power microcontroller is selected to do the main computations.

The GPS receiver needs an extra serial interface, because it supports only a serial point-to-point connection and no bus system. Therefore, an SPI-to-UART adapter is used. This component receives data from the SPI bus and transmits it to the GPS receiver and vice versa. This enables the communication between the microcontroller and the GPS receiver

without a direct connection to the microcontroller.

The 2.4GHz 802.15.4 Transceiver module is also connected to the SPI Bus. This supports a fast and easy communication to the transceiver module.

The ultrasonic module and the energy harvesting module are directly connected to the microcontroller. Therefore, no extra control hardware is needed, and this saves costs. The ultrasonic module needs control lines to generate the ultrasonic sound. The microcontroller detects the received sound signal to measure the water depth. The energy harvesting module does not need any control lines. This supports an error-free operation even if the microcontroller fails. The measurement of the currents and voltages can be done directly by the microcontroller.

The hardware is also equipped with a USB interface. The USB module is connected to a serial interface of the microcontroller. This enables an uncomplicated communication with a PC, because most of today's PCs have a USB interface. The MSP430 microcontroller has a bootstrap loader (BSL) that enables programming the processor via the serial interface. Therefore, the microcontroller can be programmed with every PC without special hardware. In addition, the communication with the running software is possible via the same serial interface.

3.4.1 Energy Harvesting Design

A detailed description of the energy harvesting concept will be given next. Figure 3.5 shows a block diagram of the EHS.

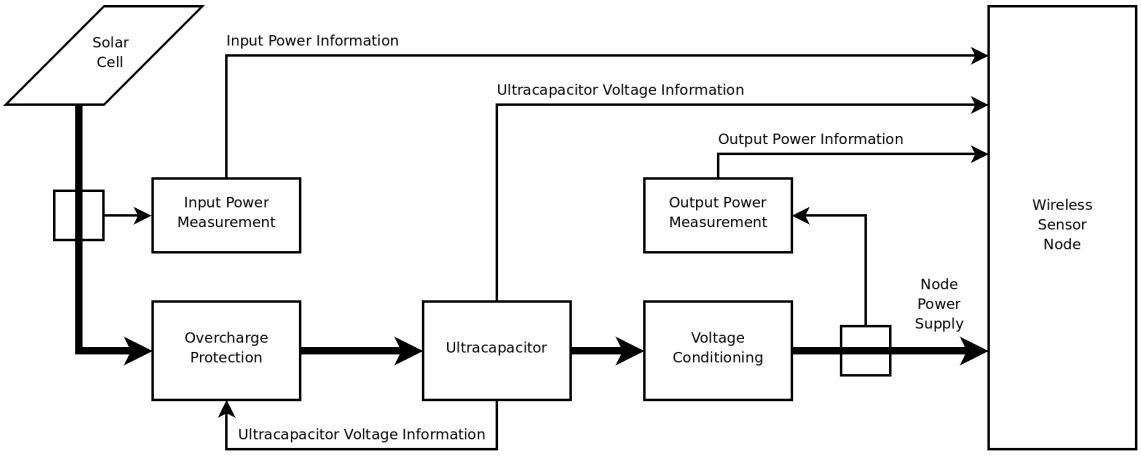

Figure 3.5: Concept of the energy harvesting hardware. The thick arrows illustrate the flow of power and the thin ones illustrate the flow of information.

The solar cell transforms the solar energy into electrical energy. It is a voltage limited current source. A short is no problem for a solar cell. The electrical power will be converted into heat in the solar cell and the connecting leads. As it can be seen in the block diagram, no voltage conditioning is done between the solar cell and the ultracapacitors. This can only be done if the solar cell is selected specially and is in line with the ultracapacitors. If various EHDs would be supported, the EHS would be more complex and more expensive.

This is why the system uses only solar cells for energy harvesting. Therefore, the solar cell must be selected properly. The voltage of the solar cell at nominal power output should be a little bit higher than the nominal voltage of the ultracapacitors. This is because some losses and a lower output voltage of the solar cell at dark light conditions must be considered. The solar cell ASI3Oo05/162/192FAmod from Schott Solar has been selected.

An overcharge protection guarantees a maximum voltage at the ultracapacitors. The power will be bypassed if the voltage at the ultracapacitors has reached the nominal voltage. The exchange of damaged ultracapacitors is expensive. Therefore, the overcharge protection must be very reliable. This protection is implemented in hardware, because then no software error can damage the ultracapacitors.

The voltage conditioning is used to generate a stable output voltage. The output voltage is set to $3.3\,V$ because most of the components are supplied with this voltage. The voltage at the ultracapacitors changes during operation and must be stabilized. The voltage ranges from $0\,V$ to $5\,V$. Therefore, a buck-boost converter should be used. A switching regulator uses a coil to transform the voltage. If the voltage of the ultracapacitors is lower than $3.3\,V$, the converter must operate in the boost mode. If the voltage is higher than $3.3\,V$, it must operate in the buck mode. This guarantees a constant output voltage.

The stored energy and the input and output power must be measured because the system needs to know the current energy state. Then the system is able to select a proper duty cycle to ensure a continuous operation. The stored energy can be calculated with the current voltage of the ultracapacitors. The microcontroller can measure the voltage and determine the stored energy. The input and output current is measured with current counters as described in [11]. These counters transform the current information into pulses. One pulse is equivalent to a specific charge. The current can be calculated knowing the equivalent charge of one pulse and the interval time. A detailed description of the current counters is given in Section 4.1.5.2 and 4.1.6.1.

3.5 Software Design

A description of the software concept of the mote can be found here. In general, the node should be as flexible as possible to be able to adapt it to specific application areas and to simplify the maintenance.

The software is used to ensure a correct functionality of the hardware in this master's thesis. Therefore, it is kept very simple. Texas Instruments®provides a free development environment called Code Composer Studio, which supports a code size of up to 10k Byte. It is based on the development environment eclipse and has a tool chain to compile C and C++ projects for the MSP430 microcontroller family. It also supports in-circuit debugging of the microcontroller via a JTAG interface. It is also possible to generate a so-called hex file that contains the binary code in a textual form. This environment is used to develop the software.

The abstraction of TinyOS (introduced in Section 2.4) is too fine grained for this project. Figure 3.6 shows the hardware abstraction of the implemented software. Each hardware module is interfaced by a single software module. This module also supports some functionality of the HAL for example conversions or buffering. Therefore, it can be used directly from the main application.

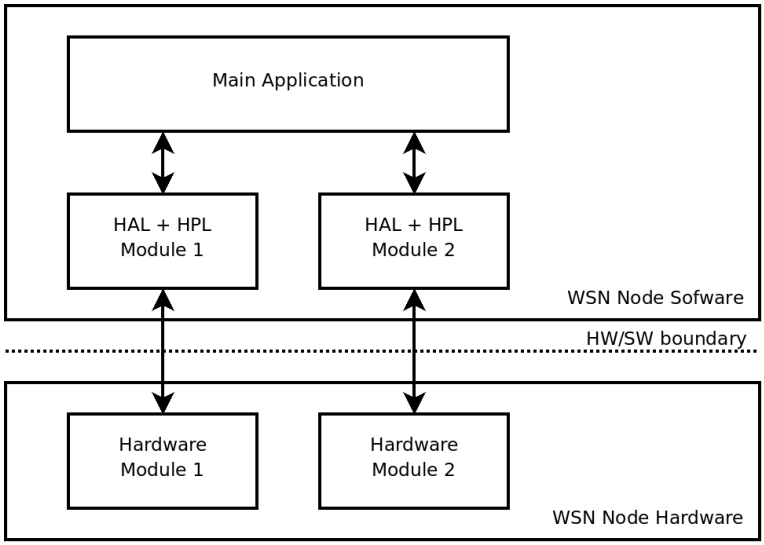

Figure 3.6: Hardware abstraction architecture of the implemented software.

3.5.1 Programming Language

The development environment supports two programming languages: C and C++. C keeps the size of the binary code lower because no object handling is necessary. Hence, C++ supports a very strong encapsulation and an object oriented programming. In addition, the maintenance is easier with C++. Therefore, C++ is used to write the test application and hardware abstraction.

3.6 Summary

This Section has shown the concept of the hardware and software. First, three different measurement principles have been selected. A pressure transducer, an ultrasonic module and a GPS receiver are envisioned for measurements. The combination of these sensors enables an accurate and reliable measurement of the river's water level. In addition, various requirements have been explained for the various sensors. Then, it has been shown that only a radio communication is practical. An RF module with a high communication range has been selected. Then, the microcontroller has been selected according to low power consumption and high flexibility. In addition, a porting of TinyOS should be possible.

Solar energy has been selected as environmental energy sources. Solar cells are able to provide enough power to operate the RiverMote. The disadvantage is the need of an energy storage device. Ultracapacitors have been selected for it, because of a very high lifetime.

Then, it has been shown that an activation interval of 15 min is enough for measuring the river's water level. The power estimation led to the result that it is possible to supply the mote during the night with the given activation interval.

The capacity of the energy storage device has been calculated according to the power estimation. Two Boostcaps®from Maxwell®with a capacity of 310 F each have been

selected. This enables an average power consumption of 21.27 mW of the mote.

Then, the hardware concept has been shown briefly. The components and the communication between the models were described. The microcontroller is used for all calculations and analysis of the measured data. This saves a lot of hardware complexity and costs. The energy harvesting concept has led to the need of an overcharge protection. This protection should be implemented in hardware to avoid software caused damage.

Finally, the concept of the software has been discussed. This software is only used for testing the proper functionality of the hardware. It has been shown that the abstraction of TinyOS is too fine grained for this software. C++ has been selected as programming language.

The concept of the hardware and software can be used for the implementation of the WSN platform.

4 Implementation of the Wireless Sensor Platform

This Chapter shows the detailed implementation of the hardware of the battery-less WSN river monitoring platform.

The hardware of a RiverMote is the corner stone of the whole system. It must support all needed features of the system and be as efficient as possible. Furthermore, the costs of the hardware should be kept as low as possible. Each hardware component, which has been developed, is described in the following Sections. The hardware setup of the RiverMote is illustrated in Figure B.2. Figure B.1 shows the RiverMote and the solar cell integrated in the housing.

4.1 Energy Harvesting Hardware

The EHS is indispensable, because the RiverMote must harvest all the needed energy from the environment. Therefore, solar cells are used as described before. They are selected specially to be able to charge the ultracapacitors directly. An overcharge protection bypasses the power if the capacitors are fully charged. A simulation of this overcharge protection can be found later in Section 4.1.1. The energy monitoring is implemented with two charge counters. The simulation of these charge counters and the calculations of the input and output power can be found in the Sections 4.1.5 and 4.1.6. The implementation of the EHS is based on the introduced design shown in Figure 3.4. The hardware is illustrated in Figure 4.1.

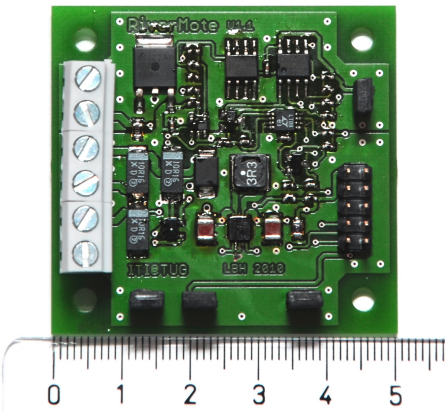

Figure 4.1: Illustration of the EHS hardware. The unit of the rule is centimeter.

4.1.1 Overcharge Protection

The overcharge protection is implemented in hardware. Therefore, no software failure can cause a destruction of the ultracapacitors. This protection circuit is simulated in LTspice IV from Linear Technology®. The circuit is shown in Figure 4.2.

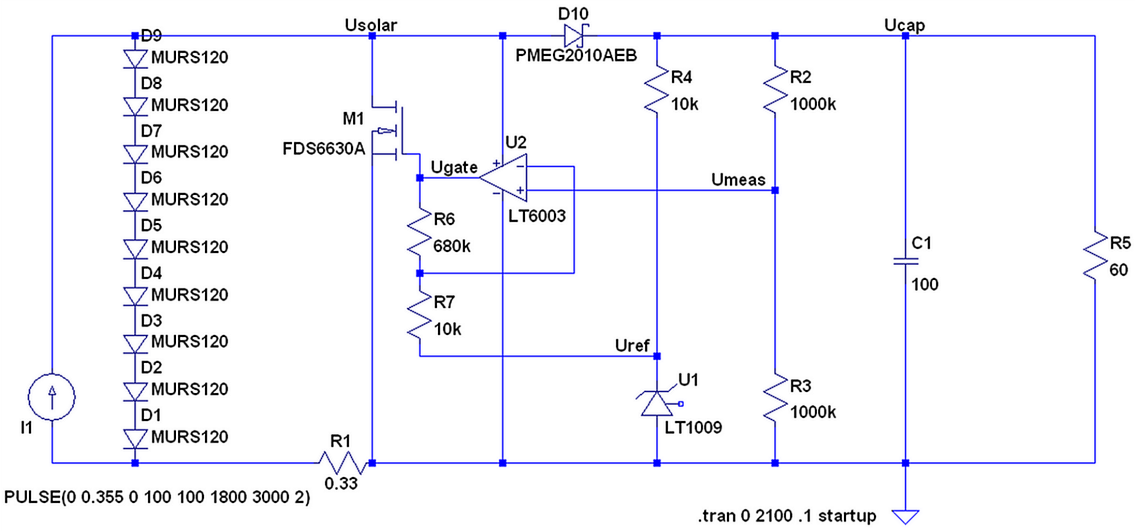

Figure 4.2: Simulation circuit of the overcharge protection.

The solar cell was substituted by a simple model. It consists of a current source and diodes. These diodes limit the output voltage. This model has a short circuit current of $0.355\,A$ and an open circuit voltage of $6.541\,V$. A detailed model is not used, because the parameter of such a model can not be found for the solar cell. Furthermore, it is not necessary to use a detailed model, because it would not enhance the insight of this simulation. The goal of the simulation is to show the functionality of the overcharge protection. Therefore, a simple model of the solar cell is sufficient. This simple model was simulated and the results are shown in Figure 4.3. It can be seen that the voltage drops slower with increasing current compared to the measured solar cell (Figure 2.8). However, it is sufficient for the simulation of the overcharge protection.

The open circuit voltage is above the nominal voltage of $5\,V$ of the ultracapacitor. To prevent a discharge of the ultracapacitor during the night via the solar cell, a diode is placed between of them. This diode should have a very low forward voltage. Therefore, a Schottky diode is used. The resistor R1 is used for current measurement. A very small resistance was chosen, in order to keep the losses low. The nominal voltage of the solar cell should be greater than or equal to the maximum operating voltage for an efficient charging:

$$U_{solar,nom} \geq U_{solar,op,max}$$

$$\begin{aligned} U_{solar,op,max} &= U_{capacitor,nom} + U_{D,forward} + R_1 \cdot I_{solar,nom} \\ &= 5V + 0.4V + 0.33\Omega \cdot 0.355A \\ &= 5.517\,V \end{aligned}$$

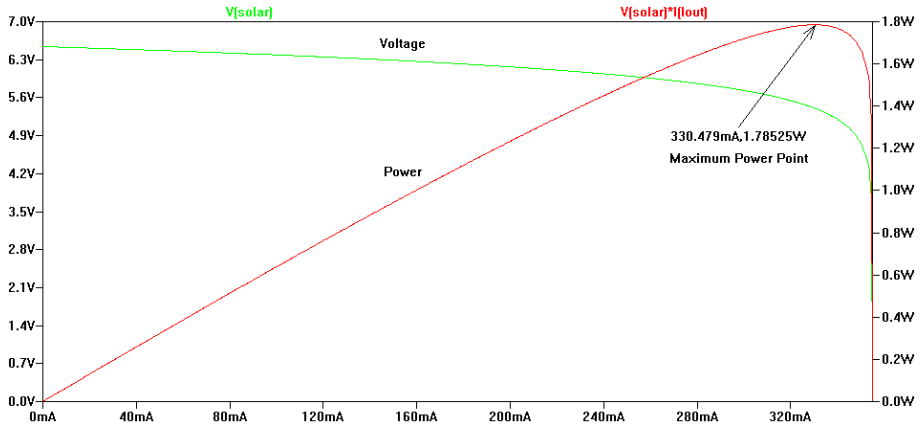

Figure 4.3: U-I diagram of the simulated solar cell model. The green trace shows the output voltage and the red trace shows the output power of the solar cell model.

Since the open circuit voltage is higher than the nominal voltage of a solar cell, the ultracapacitors must be protected. The excess power is bypassed by the overcharge protection. The simulation results can be seen in Figure 4.4. Note that a capacitor with $100\,F$ is used for a better visualization. It can be seen that the voltage of the ultracapacitors does not exceed the $5\,V$ limit. The overshoot of the solar voltage, just before the ultracapacitors are fully loaded, is caused by the Schottky diode. The current decreases through the diode, when the capacitors are fully charged. Therefore, the voltage drop of the Schottky diode decreases. The overcharge protection reduces the solar voltage to keep the voltage of the capacitors below $5\,V$.

The maximum input current for charging is assumed to $I_{charge,max} = 0.5\,A$. This is more than the short circuit current of the selected solar cell. The ultracapacitor ($C = 155\,F$) can be charged with this current in $3400\,s$. Now the maximum ratings and other important values of the components can be calculated.

MOSFET The MOSFET is used to bypass the excess power. The operating voltage is $U_{MOSFET} = U_{capacitor,nom} + U_{D,forward} = 5.4\,V$. The power dissipation can be calculated with:

$$P_{D,MOSFET} = U_{MOSFET} \cdot I_{charge,max} = 5.4V \cdot 0.5A = 2.7\,W$$

Shunt Resistor The shunt resistor is used for measuring the current of the solar cell. The power dissipation can be calculated with:

$$P_{D,Rshunt} = I^2_{charge,max} \cdot R = (0.5A)^2 \cdot 0.33\Omega = 0.0825\,W$$

Therefore, a standard 1/8 or 1/4 Watt resistor can be used. The maximum voltage drop is:

$$U_{Rshunt,max} = I_{charge,max} \cdot R = 0.5A \cdot 0.33\Omega = 0.165\ V$$

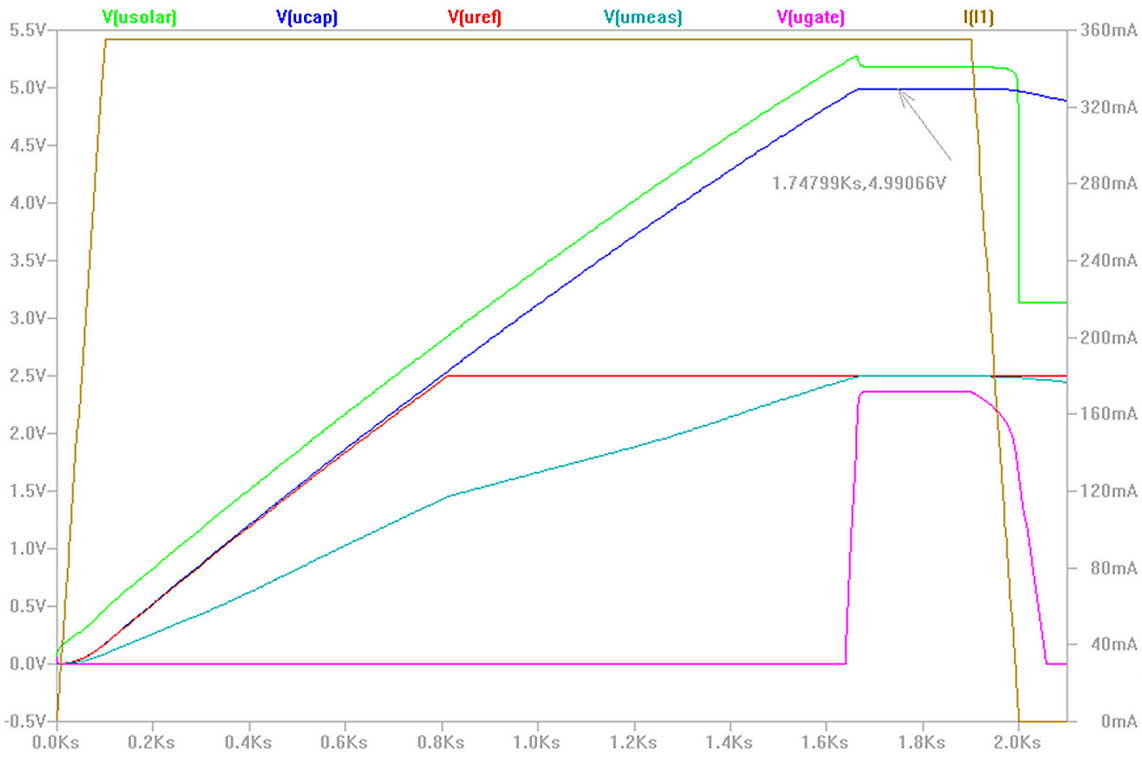

Figure 4.4: Simulation results of the overcharge protection circuit using a capacitor with a value of 100 F. The resistor R_5 represents the mote with a current of 83.3 mA.

Diode The Schottky diode prevents reverse discharging of the ultracapacitor. The maximum power dissipation is:

$$P_{D,diode} = U_{D,forward} \cdot I_{charge,max} = 0.4V \cdot 0.5A = 0.2\ W$$

Voltage Divider The power dissipation of the voltage divider is not critical. It is important that the current is as low as possible. The input resistance of the operational amplifier affects the voltage of the divider as it can be seen in Figure 4.4. During low operation voltage it draws a significant current. Therefore, a worst-case estimation can be done with assuming the input resistance as 0 Ω. Then, the current through the voltage divider is:

$$I_{voltdiv,max} = \frac{U_{capacitor,nom}}{R_2} = \frac{5V}{1M\Omega} = 5\ \mu A$$

This is much lower than the leakage current of the ultracapacitor and thus acceptable.

Operational Amplifier It is used as non-inverting amplifier with an additional reference voltage. Only if the input voltage at the positive input pin is higher than the reference voltage the amplifier will have a nonzero output. The gain of the amplifier is dependent on the two resistors R_6 and R_7. It can be calculated with:

$$gain = 1 + \frac{R_6}{R_7} = 1 + \frac{680k}{10k} = 69$$

4.1.2 Voltage Conditioning

The voltage conditioning is done by a DC-DC switching converter. This enhances the efficiency to a maximum, because no power is lost in linear regulators. The TPS63001 from Texas Instruments®is used. This buck-boost converter operates within an input voltage range from $1.8\,V$ to $5.5\,V$. The maximum efficiency is 96 % in buck mode and the maximum output current that can be delivered over the full input voltage range is about $500\,mA$. A sample circuit of the TPS63001 is shown in Figure 4.5. A key feature of this

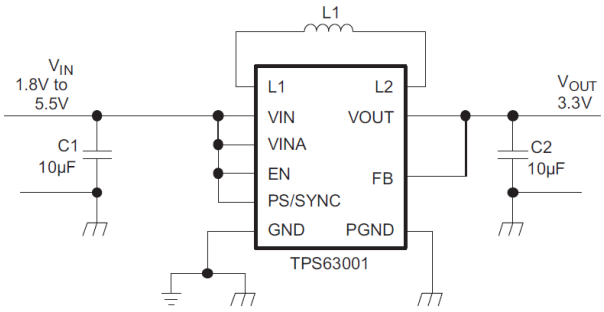

Figure 4.5: Sample circuit of the TPS63001 buck-boost converter from [44]. Note that the pin PS/SYNC must be connected to ground to enable the power saving mode.

DC-DC converter is the requirement of only 3 external components. The two capacitors are used for stabilizing the input and output voltage. A value of $10\,\mu F$ is sufficient for both capacitors. The value of the inductor must be calculated according to the data sheet [44]:

$$L_{min,buck} = \frac{U_{out} \cdot (U_{in,max} - U_{out})}{U_{in,max} \cdot f \cdot 0.3A} = \frac{3.3V \cdot (5V - 3.3V)}{5V \cdot 1.25MHz \cdot 0.3A} = 2.992\,\mu H$$

$$L_{min,boost} = \frac{U_{in,min} \cdot (U_{out} - U_{in,min})}{U_{out} \cdot f \cdot 0.3A} = \frac{1.8V \cdot (3.3V - 1.8V)}{3.3V \cdot 1.25MHz \cdot 0.3A} = 2.182\,\mu H$$

The higher minimum inductance is the significant value. This means that the minimum inductance is $2.992\,\mu H$. The recommended range of the inductor is from $1.5\,\mu H$ to $4.7\,\mu H$. Therefore, an inductance of $L = 3.3\,\mu H$ is chosen.

The maximum current through the inductor is needed to select it. This current can be calculated with:

$$\begin{aligned} I_{L,max,buck} &= \frac{I_{out,max}}{0.8} + \frac{U_{out} \cdot (U_{in,max} - U_{out})}{2 \cdot U_{in,max} \cdot f \cdot L} \\ &= \frac{0.5A}{0.8} + \frac{3.3V \cdot (5V - 3.3V)}{2 \cdot 5V \cdot 1.25MHz \cdot 3.3\mu H} \\ &= 0.761\,A \end{aligned}$$

$$\begin{aligned} I_{L,max,boost} &= \frac{U_{out} \cdot I_{out,max}}{0.8 \cdot U_{in,min}} + \frac{U_{in,min} \cdot (U_{out} - U_{in,min})}{2 \cdot U_{out} \cdot f \cdot L} \\ &= \frac{3.3V \cdot 0.5A}{0.8 \cdot 1.8V} + \frac{1.8V \cdot (3.3V - 1.8V)}{2 \cdot 3.3V \cdot 1.25MHz \cdot 3.3\mu H} \\ &= 1.245\,A \end{aligned}$$

It must be considered that the inductor should not be in saturation at the maximum current of $I_{L,max} = 1.245\,A$.

4.1.2.1 Startup

The DC-DC converter starts operating at an input voltage of $U_{start} = 1.8\,V$. Thus, the other hardware starts also normal operation and the microcontroller will boot. This boot sequence should be completed, because the microcontroller should not stay in an undefined state or store only fragments of data in the flash memory. The only thing that could interrupt the boot sequence is a switch-off of the DC-DC converter. This occurs if the input voltage drops under the so-called under voltage lockout threshold of $U_{lockout} = 1.5\,V$. Therefore, the boot sequence must be completed within a certain time. The available energy can be calculated with:

$$\begin{aligned} E_{boot} &= \frac{1}{2} \cdot C \cdot (U_{start}^2 - U_{lockout}^2) \cdot \eta_{convert} \\ &= \frac{1}{2} \cdot 155F \cdot ((1.8V)^2 - (1.5V)^2) \cdot 0.8 \\ &= 61.38\,J \end{aligned}$$

This means that the boot sequence must consume no more energy than $61.38\,J$. The time can be calculated with the power consumption of the mote:

$$t_{boot} = \frac{E_{boot}}{P_{max,full}} = \frac{61.38J}{854mW} = 71.87\,s$$

If the mote does not activate the radio module at startup, the booting time can be extended to (activated components: microcontroller, GPS module, ultrasonic sensor):

$$t_{boot} = \frac{E_{boot}}{P_{max,reduced}} = \frac{61.38J}{175mW} = 350.7\,s = 5.85\,min$$

This should be enough time to save data and switch into a power saving mode.

4.1.3 Capacitor Balancing

The balancing of the ultracapacitor voltages is necessary because of the tolerances and the different leakage currents. One of the easiest and most effective ways to balance the voltages is to use a voltage inverter. This inverter converts the input voltage into the exact negative output voltage. It can be used to halve the full capacitor voltage and so to balance both capacitors. Figure 4.6 shows the application circuit of such an inverter. The MAX828 voltage inverter is used in this project. The maximum output current of the inverter is 25mA and it operates at a voltage range between $1.5\,V$ and $5.5\,V$. The switching frequency is $f = 12\,kHz$ and the output resistance is $R_i = 26\,\Omega$. The capacitors C3 and C5 are only necessary if the inverter chip is used for very accurate measurement applications. Therefore, they can be omitted here. The switched capacitor C2 has a capacity of $C_{sw} = 10\,\mu F$.

The time constant can be determined with:

$$\tau = R_i \cdot C_{sw} = 26 \cdot 10\mu F = 260\,\mu s$$

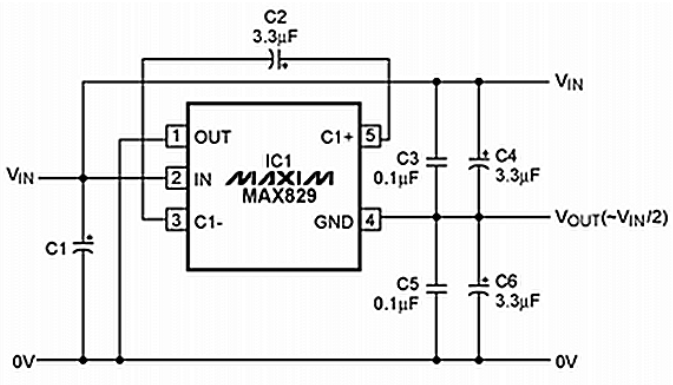

Figure 4.6: Application circuit of a voltage inverter, which is used as voltage splitter from [25].

The switching time is:

$$t_{sw} = \frac{1}{f} = \frac{1}{12kHz} = 83\,\mu s$$

This time represents one period. Therefore, the switched capacitor is connected to the input during the first half of t_{sw} and to the output during the second half. Therefore, the connection time of the capacitor is:

$$t_{con} = \frac{t_{sw}}{2} = 41.67\,\mu s$$

It can be seen that the switched capacitor will not be charged or discharged completely during the connection time. The discharge can be calculated by assuming the initial switched capacitor voltage:

$$U_{sw,t0} = \frac{U_{ucap1} + U_{ucap2}}{2}$$

U_{ucap1} and U_{ucap2} are the voltages of both ultracapacitors. The difference of the ultracapacitor voltages can be defined as:

$$U_{diff} = U_{ucap1} - U_{ucap2}$$

The voltage difference after connecting the switched capacitor a ultracapacitor is:

$$U_{sw,diff} = \frac{U_{diff}}{2}$$

The discharge process can be described with:

$$u_{sw}(t) = U_{sw,diff} \cdot e^{-\frac{t}{\tau}}$$

The absolute change of the voltage is

$$\Delta u_{sw} = U_{sw,diff} - u_{sw}(t = t_{con})$$

and the relative change of the voltage is:

$$f_{usw,rel} = \frac{U_{sw,diff} - u_{sw}(t = t_{con})}{U_{diff}} = 1 - e^{-\frac{t_{con}}{\tau}} = 1 - e^{-\frac{41.67}{260}} = 14.8\,\%$$

Now the change of the charge can be calculated with:

$$\Delta Q_{sw} = C_{sw} \cdot \Delta u_{sw}(t = t_{con}) = C_{sw} \cdot U_{sw,diff} \cdot \left(1 - e^{-\frac{t_{con}}{\tau}}\right)$$

The current is the charge divided by the switching time:

$$I_{balance}(U_{diff}) = \frac{Q_{sw}}{t_{con}} = \frac{C_{sw} \cdot U_{diff}}{2 \cdot t_{con}} \cdot \left(1 - e^{-\frac{t_{con}}{\tau}}\right)$$

This is only an estimation of the lower limit because the real voltage difference at the switched capacitor is higher than half the voltage difference of the ultracapacitors. The expected balancing current of the real hardware is higher than the calculated one.

The maximum charge current of the ultracapacitors can be calculated with the previous result. The tolerance is $\pm 20\,\%(d = 0.2)$ for the capacitors. The worst-case scenario is:

$$C_{ultra,1} = C \cdot (1 - d)$$

$$C_{ultra,2} = C \cdot (1 + d)$$

The resulting total capacity is:

$$C_{tot} = \frac{C_{ultra,1} \cdot C_{ultra,2}}{C_{ultra,1} + C_{ultra,2}} = C \cdot \frac{1 - d^2}{2}$$

The total charge is equal to the charge of the single ultracapacitors:

$$Q_{tot} = Q_{uc1} = Q_{uc2} = U_{full,charge} \cdot C \cdot \frac{1 - d^2}{2} = 5V \cdot 310F \cdot \frac{1 - 0.2^2}{2} = 744\,As$$

The expected voltage of the smaller capacitor after charging is:

$$U_{uc1} = \frac{Q_{uc1}}{C_{ultra,1}} = U_{full,charge} \cdot \frac{1 + d}{2} = 5V \cdot \frac{1.2}{2} = 3\,V$$

The difference to the surge voltage of the ultracapacitor is:

$$\Delta U_{max} = U_{uc1} - U_{max} = 3V - 2.7V = 0.3V$$

The charge difference is:

$$\Delta Q = \Delta U_{max} \cdot C_{ultra,1} = 0.3V \cdot 310F \cdot 0.8 = 74.4\,As$$

Now the minimum charging time can be calculated with the charge that must be balanced and the balancing current. The calculated balancing current at a voltage difference of $\Delta U_{balance} = (U_{max} - U_{uc,nom}) \cdot 2 = 0.4V$ is $I_{bal,0.4V} = 7.2\,mA$. The charging time is:

$$t_{charge} = \frac{\Delta Q}{I_{bal,0.4V}} = \frac{74.4As}{7.2mA} = 10333\,s = 2.87\,h$$

The maximum charging current can now calculated with the total charge and the charging time:

$$I_{charge} = \frac{Q_{tot}}{t_{charge}} = \frac{744As}{10333s} = 72\,mA$$

This means that the maximum charging current should not exceed $72\,mA$ if the expected balancing current is not higher than the calculated one. Therefore, the selected solar cells should not be used.

4.1.4 Energy Monitoring

The energy monitoring should also be as simple as possible. Therefore, the MSP430 microcontroller is used to calculate the input and output power and the available energy. The microcontroller provides the calculation and measurement functionality and so no further resources and consequently energy are wasted. The following three Sections (4.1.5, 4.1.6 and 4.1.7) show the measurement and calculation of the input and output power and the available energy.

4.1.5 Input Power Measurement

The calculation of the input power needs the measurement of the solar voltage and the solar current. Section 4.1.5.1 and 4.1.5.2 overview the measurement principles and the expected errors.

4.1.5.1 Solar Voltage Measurement

The voltage can be measured directly via a voltage divider. This is necessary, because the microcontroller operates with a voltage of $U_{sup} = 3.3\,V$. More than $U_{sup} + 0.3V = 3.6\,V$ at any pin will damage it [45]. The voltage divider consists of two resistors with $R_1 = R_2 = 33\,k\Omega$ and a tolerance of 1 % each. The microcontroller is able to measure the reduced voltage $U_{meas,solar}$. The voltage at the solar cell can be calculated with:

$$U_{solar} = U_{meas,solar} \cdot \frac{R_1 + R_2}{R_1} = f(U_{meas,solar}, R_1, R_2)$$

In this case the equation can be reduced and the solar voltage can be calculated easily:

$$U_{solar} = U_{meas,solar} \cdot 2$$

The result depends on more than one source of error. Therefore, the error propagation must be considered (non-reduced equation):

$$\Delta Y_{er} \approx \pm \sum_{j=1}^{v} \left| \frac{\partial f}{\partial Y_j} \cdot \Delta Y j \right|$$

$$\begin{aligned}\Delta U_{solar,err} &\approx \pm\left(\left|\frac{\partial f}{\partial U_{meas,solar}}\cdot\Delta U_{meas,solar}\right|+\left|\frac{\partial f}{\partial R_1}\cdot\Delta R_1\right|+\left|\frac{\partial f}{\partial R_2}\cdot\Delta R_2\right|\right)\\ &\approx \pm\left(\left|\frac{R_1+R_2}{R_1}\cdot\Delta U_{meas,solar}\right|+\left|-\frac{U_{meas,solar}\cdot R_2}{R_1^2}\cdot\Delta R_1\right|+\right.\\ &\quad\left.\left|\frac{U_{meas,solar}}{R_1}\cdot\Delta R_2\right|\right)\end{aligned}$$

The value and the tolerance of both resistors result in an error of $\Delta R_1 = \Delta R_2 = 33k\Omega \cdot 0.01 = 330\,\Omega$. The total unadjusted error of the 12-bit ADC of the MSP430 microprocessor is $\Delta Er_{LSB} = 5\ LSB$. The corresponding voltage can be calculated with:

$$\Delta U_{meas,solar} = U_{sup}\cdot\frac{\Delta Er_{LSB}}{2^{12}} = 3.3V\cdot\frac{5LSB}{2^{12}} = 4.03\,mV$$

Now the error of the calculation can be determined with:

$$\begin{aligned}\Delta U_{solar,err} &\approx \pm\left(\left|\frac{33k\Omega+33k\Omega}{33k\Omega}\cdot 4.03\,mV\right|+\left|-\frac{U_{meas,solar}\cdot 33k\Omega}{(33k\Omega)^2}\cdot 330\Omega\right|+\right.\\ &\quad\left.\left|\frac{U_{meas,solar}}{33k\Omega}\cdot 330\Omega\right|\right)\\ &\approx \pm\left(|2\cdot 4.03mV|+|-U_{meas,solar}\cdot 0.01|+|U_{meas,solar}\cdot 0.01|\right)\\ &\approx \pm\left(U_{meas,solar}\cdot 0.02+8.06\,mV\right)\end{aligned}$$

This means that the absolute error has a maximum at the maximum solar voltage. The maximum operating voltage of the solar cell is $U_{solar,op,max} = 5.517\ V$. This leads to a maximum absolute error of:

$$\Delta U_{solar,err,max} \approx \pm\left(\frac{5.517V}{2}\cdot 0.02+8.06mV\right) = 63.23\,mV$$

The relative error at the maximum solar voltage can be calculated with:

$$f_{err,min,Usolar} = \frac{\Delta U_{solar,err,max}}{U_{solar,op,max}} = \frac{63.23mV}{5.517V} = 1.15\,\%$$

The minimum solar voltage during operation (loading the ultracapacitor) is $U_{lockout} = 1.6\,V$. During continuous operation, this voltage should not be under-run. So the corresponding solar voltage is $U_{solar,op,min} = U_{lockout} + U_{D,forward} + R_1\cdot I_{solar,nom} = 2.12\,V$. The absolute error is here:

$$\Delta U_{solar,err,min} \approx \pm\left(\frac{2.12V}{2}\cdot 0.02+8.06mV\right) = 29.26\,mV$$

The relative error at the minimum solar voltage can be calculated with:

$$f_{err,max,Usolar} = \frac{\Delta U_{solar,err}}{U_{solar,op,min}} = \frac{29.26mV}{2.12V} = 1.38\,\%$$

If the solar voltage drops under the voltage of the ultracapacitor, it will not be loaded. No current flows through the solar current counter. Therefore, the measurement accuracy of the solar voltage in the range of $0\,V$ to $1.5\,V$ is irrelevant.

Note: This maximum error can only be ensured if the minimum sampling time at the microcontroller is kept. The minimum sampling time can be calculated with [43]:

$$\begin{aligned} t_{sample} &> (R_S + R_I) \cdot ln(2^{13}) \cdot C_I + 800ns \\ &> (33k\Omega + 2k\Omega) \cdot 9.011 \cdot 40pF + 800ns \\ &> 13.4\,\mu s \end{aligned}$$

4.1.5.2 Solar Current Measurement

The measurement of the current is a little bit more difficult. The value of the current can change abruptly. Therefore, a sampling of the current is not possible with the hardware. The solution is an integration of the current over the time. It can be done with a simple inverting integrator using an operational amplifier. The measurement circuit can be seen in Figure 4.7. The principle of this circuit is simple. The input voltage of the integrator

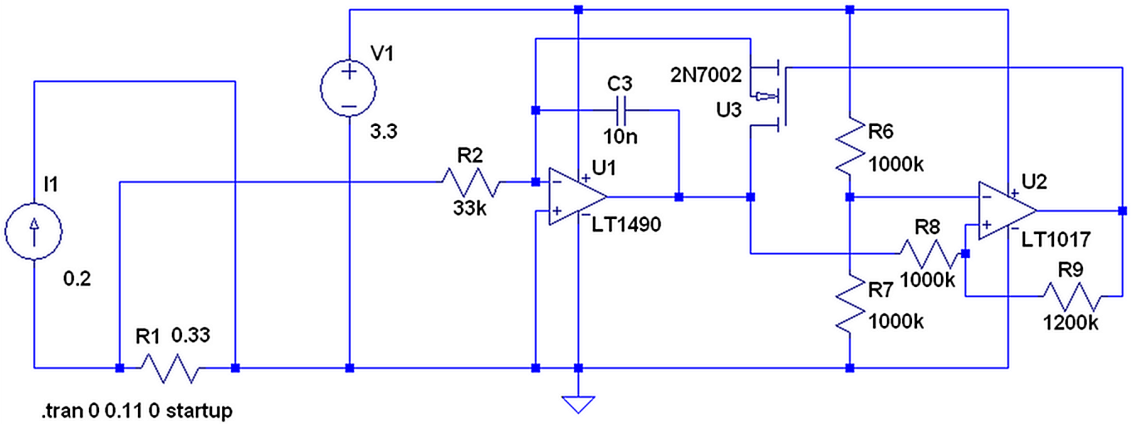

Figure 4.7: Simulation model of the solar charge counter. The main parts are the inverting integrator and the Schmitt trigger [4].

is proportional to the current through the shunt resistor R_1. This voltage is accumulated by the integrator until a certain threshold is reached. This threshold is given by the upper threshold of the Schmitt trigger. If it is reached, the capacitor of the integrator is discharged over the MOSFET. The MOSFET discharges the capacitor until the lower threshold of the Schmitt trigger is reached. Then, the normal accumulation starts again. During the discharge, a pulse is generated that can be used as charge counter.

The input of the inverting integrator has a lower potential than the reference ground of it. This potential difference causes a current flow out of the integrator. The current can only flow through the capacitor C_3 and charges it. Therefore, the voltage at the capacitor is equivalent to the solar current I_{solar}, which should be measured:

$$I_{input} = \frac{I_{solar} \cdot R_1}{R_2} = \frac{I_{solar} \cdot 0.33\Omega}{33k\Omega} = I_{solar} \cdot 10^{-5}$$

The threshold voltages of the Schmitt trigger can be calculated with:

$$U_V = U_{sup} \cdot \frac{R_7}{R_6 + R_7}$$

$$U_{th+} = U_V \cdot \frac{R_8 + R_9}{R_9}$$

$$U_{th-} = U_V \cdot \frac{R_8 + R_9}{R_9} - U_{sup} \cdot \frac{R_8}{R_9}$$

The real resistor values result in the following thresholds:

$$U_{th+} = 1.65V \cdot \frac{1M\Omega + 1.2M\Omega}{1.2M\Omega} = 3.025\,V$$

$$U_{th-} = 1.65V \cdot \frac{1M\Omega + 1.2M\Omega}{1.2M\Omega} - 3.3V \cdot \frac{1M\Omega}{1.2\Omega} = 0.275\,V$$

The difference of the two thresholds is significant for the charge counter and is:

$$U_{th,diff} = U_{th+} - U_{th-} = 3.025V - 0.275V = 2.75\,V$$

This results in an electrical charge that is necessary for charging the capacitor C_3:

$$Q_{C3} = C_3 \cdot U_{th,diff} = 10nF \cdot 2.75V = 27.5\,nAs$$

Now the charging time of the integrating capacitor C_3 can be calculated with the charge and the current through the capacitor:

$$t_{chargecnt} = \frac{Q_{C3}}{I_{input}} = \frac{C_3 \cdot U_{th,diff}}{\frac{I_{solar} \cdot R_1}{R_2}} = \frac{C_3 \cdot U_{th,diff} \cdot R_2}{I_{solar} \cdot R_1} = \frac{2.75\,mAs}{I_{solar}}$$

Therefore, one pulse is equivalent to a charge of $Q_{chargecnt,solar} = 2.75\,mAs$. The expected time of charging it ($I_{solar} = 0.2\,A$) is:

$$t_{chargecnt} = \frac{2.75mAs}{0.2A} = 13.75\,ms$$

Figure 4.8 shows the simulation result with a solar current of 200 mA. The simulated

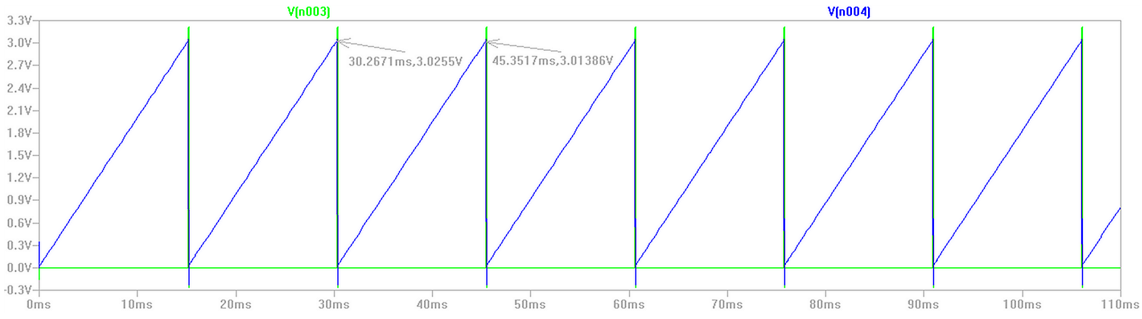

Figure 4.8: Simulation of the solar charge counter with a solar current of 200 mA. The blue trace shows the output of the integrator and thus the voltage of the capacitor C_3. The green trace shows the output of the Schmitt trigger and thus the charge counter output.

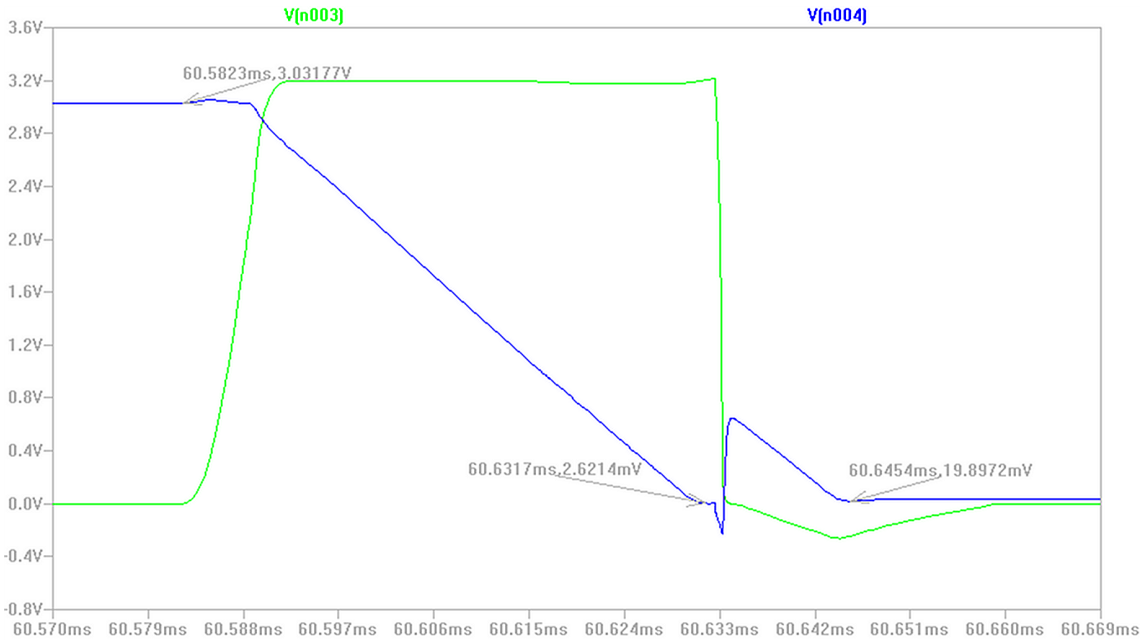

Figure 4.9: Detailed view of one discharge cycle of the integration capacitor C_3. The blue trace shows the output of the integrator and thus the voltage of the capacitor C_3. The green trace shows the output of the Schmitt trigger and thus the charge counter output.

charging time is $15.08\,ms$. It equates to an error of:

$$f_{err,tcharge} = \frac{13.75ms - 15.08ms}{15.08ms} \cdot 100\% = -8.82\ \%$$

A detailed zoom of one output pulse and discharge cycle is shown in Figure 4.9. It can be seen that the capacitor is discharged to a voltage of $19.9, mV$. The reason is the finite speed of the operational amplifier, the Schmitt trigger and the MOSFET. Now the charging time can be recalculated with the new difference between the two thresholds $U_{th,diff} = 3.012\,V$:

$$Q_{C3} = C_3 \cdot U_{th,diff} = 10nF \cdot 3.012V = 30.12\,nAs$$

$$t_{chargecnt} = \frac{C_3 \cdot U_{th,diff} \cdot R_2}{I_{solar} \cdot R_1} = \frac{3.012\,mAs}{I_{solar}}$$

One pulse is equivalent to a charge of $Q_{chargecnt,solar} = 3.012\,mAs$. Now the expected time for charging at a current of $I_{solar} = 0.2\,A$ is:

$$t_{chargecnt} = \frac{3.012mAs}{0.2A} = 15.06\,ms$$

It equates to an error of:

$$f_{err,tcharge} = \frac{15.06ms - 15.08ms}{15.08ms} \cdot 100\% = -0.13\ \%$$

It can also be seen that the discharge process is completed in 63.1 μs (= 0.42 % of the charging time). It is very fast compared to the charging time and can be neglected.

A detailed error propagation calculation is very complex here. Moreover, the main source of error is given by the tolerance of the capacitor C_3 that is 10 %. The tolerances of the other components (resistors) are kept at 1 %. Therefore, the calculation can be omitted here. The relative error of the charge counter is assumed to be 10 %.

4.1.5.3 Input Power Calculation

The input power can be calculated at the MSP430 microcontroller. Therefore, the measurement of the current and voltage of the solar cell are needed. The measurements have been discussed in detail in the previous Sections. The solar voltage can be measured directly. The current can be measured via the elapsed time between two pulses of the charge counter. Therefore, the power can be calculated with:

$$P_{solar} = \frac{Q_{chargecnt} \cdot U_{solar}}{t_{pulse}}$$

The error propagation provides the following result:

$$\begin{aligned}
\Delta P_{err,solar} &\approx \pm \left(\left| \frac{U_{solar} \cdot \Delta Q_{chargecnt}}{t_{pulse}} \right| + \left| \frac{Q_{chargecnt} \cdot \Delta U_{solar}}{t_{pulse}} \right| + \right. \\
&\quad \left. \left| - \frac{Q_{chargecnt} \cdot U_{solar} \cdot \Delta t_{pulse}}{t_{pulse}^2} \right| \right) \\
&\approx \pm \left(\left| \frac{Q_{chargecnt} \cdot U_{solar}}{t_{pulse}} \cdot \frac{\Delta Q_{chargecnt}}{Q_{chargecnt}} \right| + \left| \frac{Q_{chargecnt} \cdot U_{solar}}{t_{pulse}} \cdot \frac{\Delta U_{solar}}{U_{solar}} \right| + \right. \\
&\quad \left. \left| - \frac{Q_{chargecnt} \cdot U_{solar}}{t_{pulse}} \cdot \frac{\Delta t_{pulse}}{t_{pulse}} \right| \right) \\
&\approx \pm P_{solar} \cdot \left(\left| \frac{\Delta Q_{chargecnt}}{Q_{chargecnt}} \right| + \left| \frac{\Delta U_{solar}}{U_{solar}} \right| + \left| \frac{\Delta t_{pulse}}{t_{pulse}} \right| \right)
\end{aligned}$$

The ratio $\Delta Q_{chargecnt}/Q_{chargecnt}$ represents the relative error of the charge counter and is 10 %. Because the charge $Q_{chargecnt}$ is constant, the ratio is also constant.

The ratio $\Delta U_{solar}/U_{solar}$ represents the relative error of the voltage measurement. This error depends on the measured voltage. The solar voltage changes during the charge state of the ultracapacitors and may not be considered constant. The voltage can be measured with an absolute error of $\Delta U_{solar,err} = 63.23\ mV$. The operating voltage range is between $U_{cap} = 1.6\ V$ and $U_{cap} = 5\ V$. So the solar voltage is between $U_{solar,op,min} = 2.12\ V$ and $U_{solar,op,max} = 5.517\ V$. The relative error at these voltages is:

$$f_{err,min,Usolar} = 1.15\,\%$$

$$f_{err,max,Usolar} = 1.38\,\%$$

Therefore, the maximum relative error of the voltage measurement occurs at the minimum solar voltage and is 1.38 %.

The ratio $\Delta t_{pulse}/t_{pulse}$ represents the relative error of the time measurement. The error Δt_{pulse} consists of two parts. First of the error of the crystal oscillator and second of the latency of the interrupt service routine. The resulting error is:

$$\Delta t_{pulse} = t_{pulse} \cdot f_{err,crystal} + f_{err,uC}$$

The error of the microcontroller is given by half the cycle time of the clock frequency.

$$\Delta t_{pulse} = t_{pulse} \cdot 25ppm + \frac{1}{2} \cdot \frac{1}{6MHz}$$

The maximum absolute error can be calculated with the longest duration between two pulses (about $t_{pulse,max} = 5\,s$):

$$\Delta t_{pulse} \leq 5s \cdot 25ppm + \frac{1}{2} \cdot \frac{1}{6MHz} = 125.1\,\mu s$$

For a maximum interval of $5\,s$ ($I_{solar} = 0.6\,mA$) the relative error is:

$$f_{err,time} = \frac{\Delta t_{pulse}}{t_{pulse}} = \frac{125.1\mu s}{5s} = 25.02\,ppm$$

For a minimum interval of $6\,ms$ ($I_{solar} = 0.5\,A$) the relative error is:

$$f_{err,time} = \frac{\Delta t_{pulse}}{t_{pulse}} = \frac{108ns}{6ms} = 108.3\,ppm$$

The maximum relative error occurs at the minimum duration between two pulses and is $108.3\,ppm = 0.01\,\%$.

The estimation of the upper bounds of the resulting absolute error of the power calculation provides:

$$\begin{aligned} \Delta P_{err,solar} &\approx \pm P_{solar} \cdot \left(\frac{\Delta Q_{chargecnt}}{Q_{chargecnt}} + \frac{\Delta U_{solar}}{U_{solar}} + \frac{\Delta t_{pulse}}{t_{pulse}} \right) \\ &\leq \pm P_{solar} \cdot (0.1 + 0.0138 + 0.0001) \\ &\leq \pm P_{solar} \cdot 0.114 \end{aligned}$$

4.1.6 Output Power Measurement

The calculation of the output power requires the measurement of the current consumed by the mote. Section 4.1.6.1 overviews the measurement principle and the expected error. The output voltage is kept constant within a tolerance of ±1 % by the voltage conditioning unit. Figure 4.10 shows the output voltage depending on the output current.

4.1.6.1 Output Current Measurement

The measurement of the output current is equivalent to the measurement of the solar current described in Section 4.1.5.2. The measurement circuit is a little bit different and can be seen in Figure 4.11. The principle here is the same as the principle of the solar

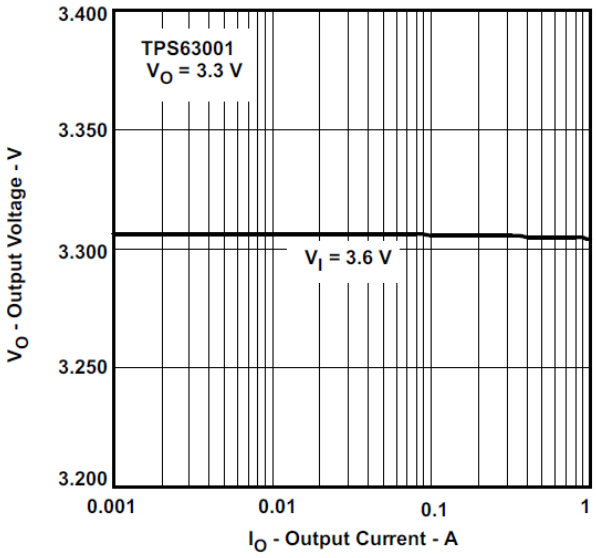

Figure 4.10: Output voltage vs. output current of the DC-DC switching regulator TPS63001 from Texas Instruments®(from [44]).

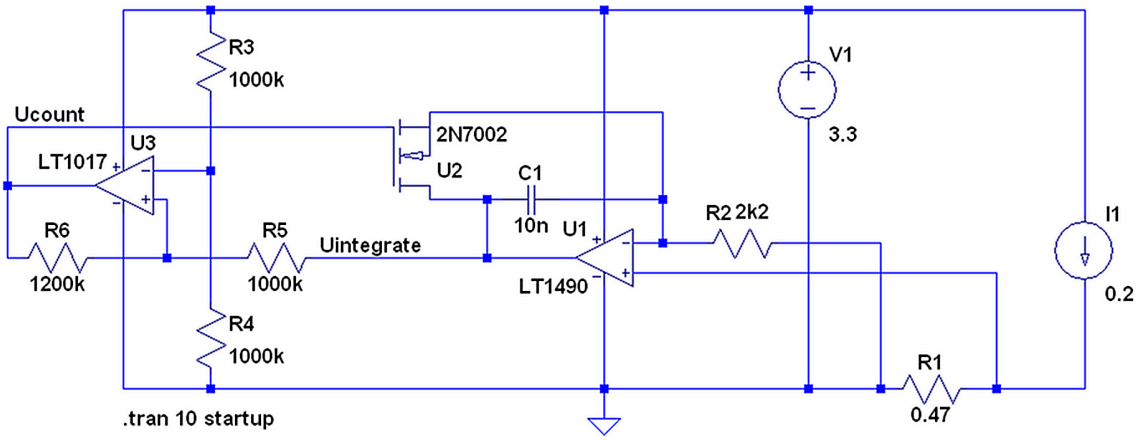

Figure 4.11: Simulation model of the output charge counter. The main parts are the inverting integrator and the Schmitt trigger. [4]

charge counter.

The input of the inverting integrator has a lower potential than the reference ground of it. This potential difference causes a current flow out of the integrator. The current can only flow through the capacitor C_1 and charges it. Therefore, the voltage at the capacitor is equivalent to the output current I_{out}, which should be measured:

$$I_{input} = \frac{I_{out} \cdot R_1}{R_2} = \frac{I_{out} \cdot 0.47\Omega}{2.2k\Omega} = I_{out} \cdot 2.14 \cdot 10^{-4}$$

The threshold voltages of the Schmitt trigger are the same, because the resistor values

have not changed:

$$U_{th+} = 3.025\,V$$

$$U_{th-} = 0.275\,V$$

$$U_{th,diff} = 2.75\,V$$

This results in an electrical charge that is necessary for charging the capacitor C_1 of:

$$Q_{C1} = C_1 \cdot U_{th,diff} = 10nF \cdot 2.75V = 27.5\,nAs$$

Now the charging time of the integrating capacitor C_1 can be calculated with the charge and the current through the capacitor:

$$t_{chargecnt} = \frac{Q_{C1}}{I_{input}} = \frac{C_1 \cdot U_{th,diff}}{\frac{I_{out} \cdot R_1}{R_2}} = \frac{C_1 \cdot U_{th,diff} \cdot R_2}{I_{out} \cdot R_1} = \frac{128.7\,\mu As}{I_{out}}$$

The expected time for charging ($I_{mote} = 0.2\,A$) is:

$$t_{chargecnt2} = \frac{128.7\mu As}{0.2A} = 0.644\,ms$$

Therefore, one pulse is equivalent to a charge of $Q_{chargecnt2} = 128.7\,\mu As$.

Figure 4.12 shows the simulation result with a mote current of $200\,mA$. The simulated

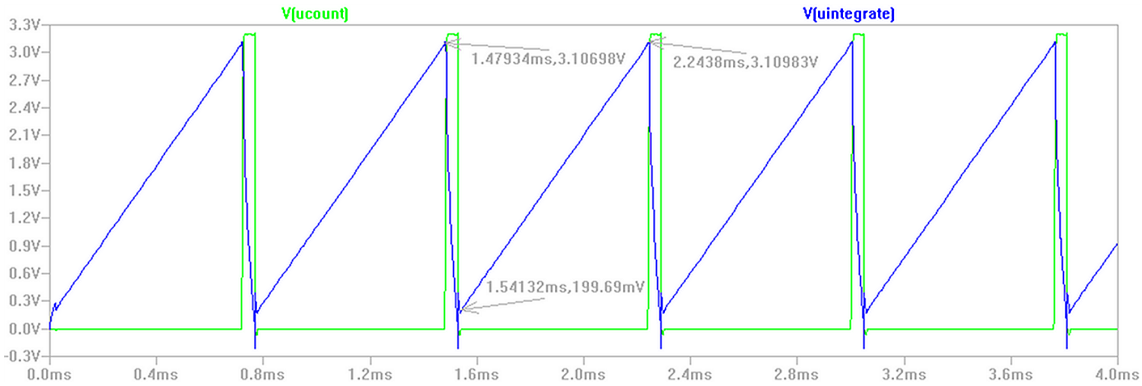

Figure 4.12: Simulation of the output charge counter with a current of $200\,mA$. The blue trace shows the output of the integrator and thus the voltage of the capacitor C_1. The green trace shows the output of the Schmitt trigger and thus the charge counter output.

charging time is $0.702\,ms$. It equates to an error of:

$$f_{err,tcharge2} = \frac{0.644ms - 0.702ms}{0.702ms} \cdot 100\% = -8.26\,\%$$

It can be seen that the simulated voltage difference is $U_{th,diff} = 2.91\,V$. The reason is the finite speed of the operational amplifier and the Schmitt trigger. Now the charging time can be recalculated with the new difference between the two thresholds $U_{th,diff} = 2.91\,V$:

$$Q_{C1} = C_1 \cdot U_{th,diff} = 10nF \cdot 2.91V = 29.1\,nAs$$

$$t_{chargecnt} = \frac{C_1 \cdot U_{th,diff} \cdot R_2}{I_{out} \cdot R_1} = \frac{136.2\,\mu As}{I_{out}}$$

One pulse is equivalent to a charge of $Q_{chargecnt2} = 136.2\,\mu As$. Now the expected time for charging at a current of $I_{out} = 0.2\,A$ is:

$$t_{chargecnt2} = \frac{136.2\mu As}{0.2A} = 0.681\,ms$$

It equates to an error of:

$$f_{err,tcharge2} = \frac{0.681ms - 0.702ms}{0.702ms} \cdot 100\% = -2.99\ \%$$

The remaining error is caused by the leakage current of the MOSFET.

It can also be seen that the discharge process is completed in $61.98\,\mu s$ (= 8.8 % of the charging time). This time cannot be neglected here. The discharging time must be considered in power calculation of the microcontroller.

A detailed error propagation calculation is very complex here. Moreover, the main source of error is given by the tolerance of the capacitor C_1 that is 10 %, too. The tolerances of the other components (resistors) are kept at 1 %. Therefore, the calculation can also be omitted here. The relative error of the charge counter is assumed to be 10 %.

4.1.6.2 Output Power Calculation

The output power can be calculated at the MSP430 microcontroller. Therefore, the measurement of the output current is needed. The measurement has been discussed in detail in the previous Section. The voltage can be assumed constant. The current can be measured via the elapsed time between two pulses of the charge counter. Therefore, the power can be calculated with:

$$P_{out} = \frac{Q_{chargecnt2} \cdot U_{sup}}{t_{pulse2}}$$

The error propagation provides the same result:

$$\Delta P_{err,out} \approx \pm P_{out} \cdot \left(\frac{\Delta Q_{chargecnt2}}{Q_{chargecnt2}} + \frac{\Delta U_{sup}}{U_{sup}} + \frac{\Delta t_{pulse2}}{t_{pulse2}} \right)$$

The ratio $\Delta Q_{chargecnt2}/Q_{chargecnt2}$ represents the relative error of the charge counter and is 10 %. Because the charge $Q_{chargecnt2}$ is constant, the ratio is also constant.

The ratio $\Delta U_{sup}/U_{sup}$ represents the relative error of the supply voltage. This error is given by the tolerance of the DC-DC converter and is 1 % [44].

The ratio $\Delta t_{pulse2}/t_{pulse2}$ represents the relative error of the time measurement. The considerations of the input power calculation can be taken here as well. The relative error is at a minimum interval of 0.681 ms ($I_{out} = 0.2\,A$):

$$f_{err,time} = \frac{\Delta t_{pulse}}{t_{pulse}} = \frac{108ns}{0.681ms} = 108.3\,ppm$$

The maximum relative error occurs at the minimum duration between two pulses and is $147\,ppm = 0.015\,\%$.

The estimation of the upper bounds of the resulting absolute error of the power calculation provides:

$$\begin{aligned}\Delta P_{err,out} &\approx \pm P_{out} \cdot \left(\frac{\Delta Q_{chargecnt2}}{Q_{chargecnt2}} + \frac{\Delta U_{sup}}{U_{sup}} + \frac{\Delta t_{pulse2}}{t_{pulse2}} \right) \\ &\leq \pm P_{out} \cdot (0.1 + 0.01 + 0.00015) \\ &\leq \pm P_{out} \cdot 0.11015\end{aligned}$$

4.1.7 Available Energy Measurement

The measurement of the available energy, which is stored in the ultracapacitors, can only be done indirectly. The energy can be calculated with the voltage of the capacitors:

$$E = \frac{1}{2} \cdot C \cdot U_{cap}^2$$

The capacity C is known and the voltage U_{cap} can be measured. The full capacitor voltage cannot be measured by the microcontroller, because it is too high. One possibility is to reduce the capacitor voltage with a voltage divider. Another possibility is to use voltage of the capacitor balancing circuit $U_{cap,half}$. If the capacitors are balanced this voltage is exactly half the total capacitor voltage U_{cap}.

The tolerance of the ultracapacitors is $d = 20\,\%$. If the capacity of both ultracapacitors is nearly the same, they will be balanced very well. The maximum voltage difference occurs if one of them is charged up to the maximum voltage of $U_{max} = 2.7\,V$ and the other one to $2.3\,V$. The measured voltage is $2.3V$ or $2.7V$. The expected stored energy is:

$$E_{store,min} = \frac{1}{2} \cdot 155F \cdot (2 \cdot 2.3V)^2 = 1639.9\,J$$

$$E_{store,max} = \frac{1}{2} \cdot 155F \cdot (2 \cdot 2.7V)^2 = 2259.9\,J$$

The real stored energy is:

$$E_{store,real} = \frac{1}{2} \cdot C \cdot \frac{1 - d^2}{2} \cdot (5V)^2 = 1860\,J$$

The relative error is:

$$f_{err,1} = \frac{E_{store,min} - E_{store,real}}{E_{store,real}} = \frac{1639.9J - 1860J}{1860J} = -11.8\,\%$$

$$f_{err,2} = \frac{E_{store,max} - E_{store,real}}{E_{store,real}} = \frac{2259.9J - 1860J}{1860J} = -21.5\,\%$$

The ADC of the microcontroller has a measurement error of $\Delta U_{meas} = 4.03\,mV$. The relative error at full charged and balanced ultracapacitors is

$$f_{err,Ucap} = \frac{\Delta U_{meas}}{U_meas} = \frac{4.02mV}{2.5} = 0.16\,\%$$

and can be neglected. Other measurement errors can also be neglected because of the high tolerance of the ultracapacitors.

It can be seen that the error of the available energy measurement can be very high if the capacitors are not balanced. Otherwise, it is the easiest method and saves energy and components. If the total ultracapacitor voltage is measured via a voltage divider, an additional current would discharge the ultracapacitors. Therefore, the more inaccurate but simpler and more efficient solution is chosen.

4.2 Wireless Sensor Node

This Section gives a detailed description of the implemented hardware of the mote. Each main functional group is explained in the following Sections. The implementation of the mote is based on the introduced design shown in Figure 3.4. The hardware is illustrated in Figure 4.13.

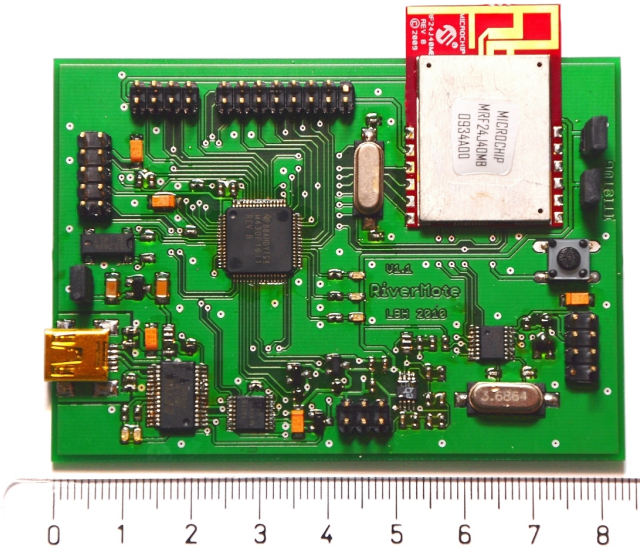

Figure 4.13: Illustration of the mote hardware. The unit of the rule is centimeter.

4.2.1 Microcontroller

The MSP430F1611 microcontroller itself does not need many external components to ensure a proper functionality.

To ensure low-power operation during sleep mode, a low frequency oscillator crystal is used. This oscillator has a frequency of $f_{low} = 32768\,Hz$. It is the reference for the so-called auxiliary clock signal of the microcontroller.

A second high frequency crystal oscillator is used during normal workload. This oscillator has a frequency of $f_{high} = 6\,MHz$. It is the reference for the main clock signal of the microcontroller.

The ADC module has an internal reference generator. This generator can be used to generate one of two supported reference voltages ($1.5\,V$ and $2.5\,V$). The generated reference voltage must be stabilized externally. Therefore, the reference voltage pin is connected with two capacitors. The first capacitor is used for stabilizing the voltage during conversions and has a capacity of $4.7\,\mu F$. The second capacitor is used for absorbing high frequency (HF) disturbances and has a capacity of $100\,nF$.

Furthermore, the analog input pins are also equipped with $100\,nF$ capacitors. They are used for absorbing high frequency disturbances.

The microcontroller has two universal synchronous/asynchronous receive/transmit (USART) peripheral interface modules. The first module (USART0) is used to communicate with the PC and is configured asynchronously. Therefore, it is connected with the USB interface module. The second module is used for SPI communication. It is connected to the local bus and can communicate with more than one device. It is connected with the radio module, the GPS receiver and the expansion connector.

The microcontroller can be programmed via the JTAG interface and the BSL. The BSL is used here, because the JTAG interface would need additional hardware. The BSL uses two special pins (P1.1 and P2.2) for serial communication. Therefore, these pins are also connected to the transmission lines of the serial interface (beside the transmission lines of the USART0). This is possible, because during the BSL start procedure, the microcontroller is reset and the USART0 is disabled.

4.2.2 USB Interface

This module is used for communication between a PC and the mote. The main component is the FT232RL interface chip. It provides a serial interface similar to the RS232 interface but at CMOS level. It is used for communication and for programming. Therefore, it is connected to the USART0 of the microcontroller and the BSL pins. Two LEDs are indicating the reception and transmission of data.

The USB interface module is decoupled from the rest of the mote. An analog switch cuts the communication lines between the microcontroller and the interface chip if the USB is disconnected.

The USB module is supplied from the PC via the USB. It can also be used to supply the mote. Therefore, a jumper (USBPWR) must be applied. This jumper must not be applied if the mote is supplied by the EHS.

4.2.3 LEDs

The mote is equipped with three LEDs that can be controlled by the microcontroller. The series resistors of the LEDs are designed to keep the current drain of the LEDs low.

Green LED: The minimum forward voltage of the green diode is $1.8\,V$ [20]. A series resistor of $1\,k\Omega$ leads to a maximum current of:

$$I_{max,green} = \frac{3.3V - 1.8V}{1k\Omega} = 1.5\,mA$$

Red LED: The minimum forward voltage of the red diode is $1.6\,V$ [21]. A series resistor of $1.5\,k\Omega$ leads to a maximum current of:

$$I_{max,red} = \frac{3.3V - 1.6V}{1.5k\Omega} = 1.13\,mA$$

Yellow LED: The minimum forward voltage of the yellow diode is $1.6\,V$ [19]. A series resistor of $1.5\,k\Omega$ leads to a maximum current of:

$$I_{max,yellow} = \frac{3.3V - 1.7V}{1.5k\Omega} = 1.06\,mA$$

4.2.4 Radio Module

As discussed in Section 3.1.3, the MRF24J40MB transceiver module is used. This module can be controlled via the SPI bus. It has also an interrupt pin to notify the microcontroller and a wake-up pin that is used to stop the sleeping mode of the module. The reset pin is used to clear all settings of the module. It is connected to the reset-signal of the mote. The chip select pin is used for the SPI communication. To accept data from the SPI bus or put data on the SPI bus, this signal must be enabled.

4.2.5 GPS Module

The GPS module provides a serial interface similar to the RS232 interface but at CMOS level. Because both USART modules are already used, an SPI compatible UART is used. It is the MAX3100 from MAXIM®. This UART is connected to the SPI bus. It provides the serial interface, which is connected to the GPS module. An interrupt pin is used to notify the microcontroller about events.

The GPS module itself has two special power supply pins. The first one is used for backup. It should be connected permanently to the power supply of the mote. This guarantees a fast position fix. The second one is used for power supply. If it is supplied, the GPS module starts working. The GPS enable signal of the microcontroller controls the state of the GPS module and of the UART. If it is low, the UART is kept in sleep mode and the power supply of the GPS module is cut off. The backup supply remains. If the signal is high the UART and the GPS module starts working normally.

The UART must be configured to the supported speed of the GPS module, before it could be used. The chip select pin is used for the SPI communication. To accept data from the SPI bus or put data on the SPI bus this signal must be enabled.

4.2.6 Ultrasonic Module

The ultrasonic module is integrated in the mote hardware. The whole module can be enabled with the ultrasonic enable signal. If the module is disabled, none of its components are supplied. The module is split into two parts and is described in the following two Sections.

4.2.6.1 Pulse Generation Circuit

The first part is used for generating the ultrasonic pulse. The circuit is shown in Figure 4.14. The four MOSFETs form a so-called H-bridge. So the resonator can be supplied with positive and negative supply voltage. The reachable peak-to-peak voltage at the resonator is about $6.6\,V$ at a supply voltage of $3.3\,V$. The simulation results are shown in Figure 4.15. It can be seen that the peak-to-peak voltage difference at the resonator is

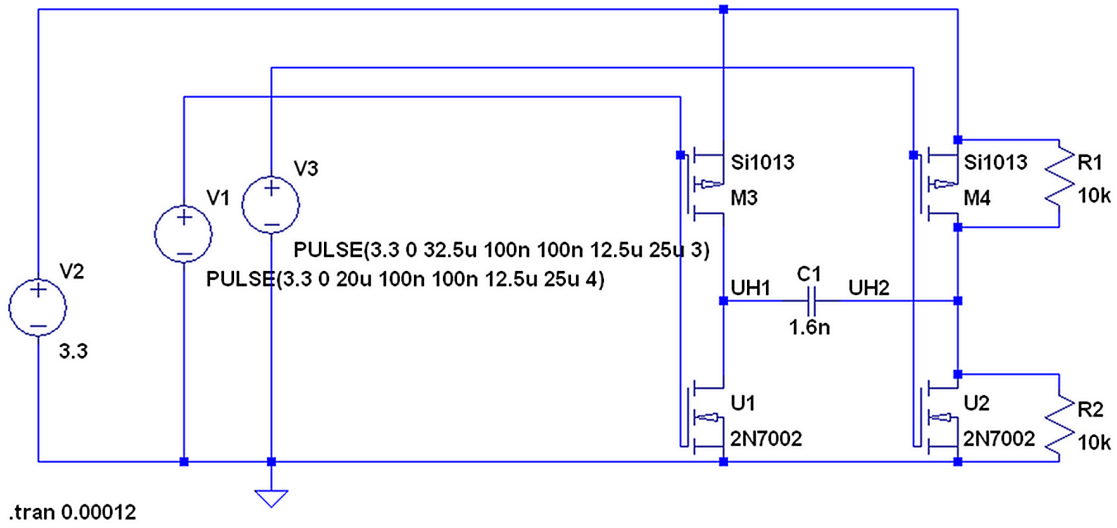

Figure 4.14: Circuit for ultrasonic pulse generation. C1 represents the transceiver.

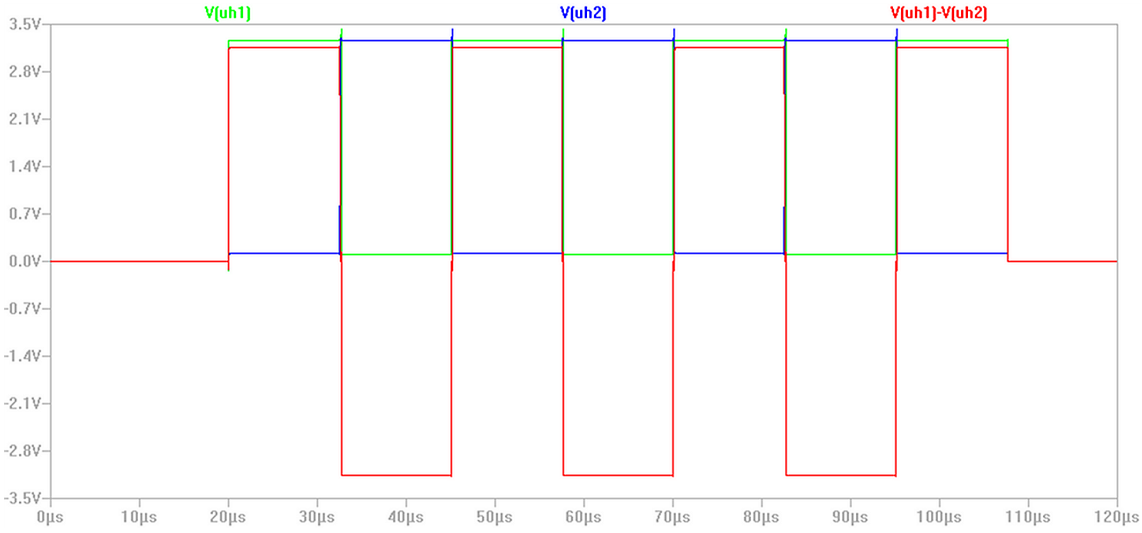

Figure 4.15: Simulation of the H-bridge that is used for ultrasonic pulse generation. The green trace and the blue trace represent the voltages at both pins of the resonator. The red trace represents the voltage difference at the resonator.

about 6.6 V. A detailed view of the transition is shown in Figure 4.16. It can be seen that there are two current peaks. The reason is that both transistors at one side are switched simultaneously. This should be omitted to reduce the power consumption. The solution is a unique control signal for each transistor. Then, the first transistor can be switched off before the second one is switched on.

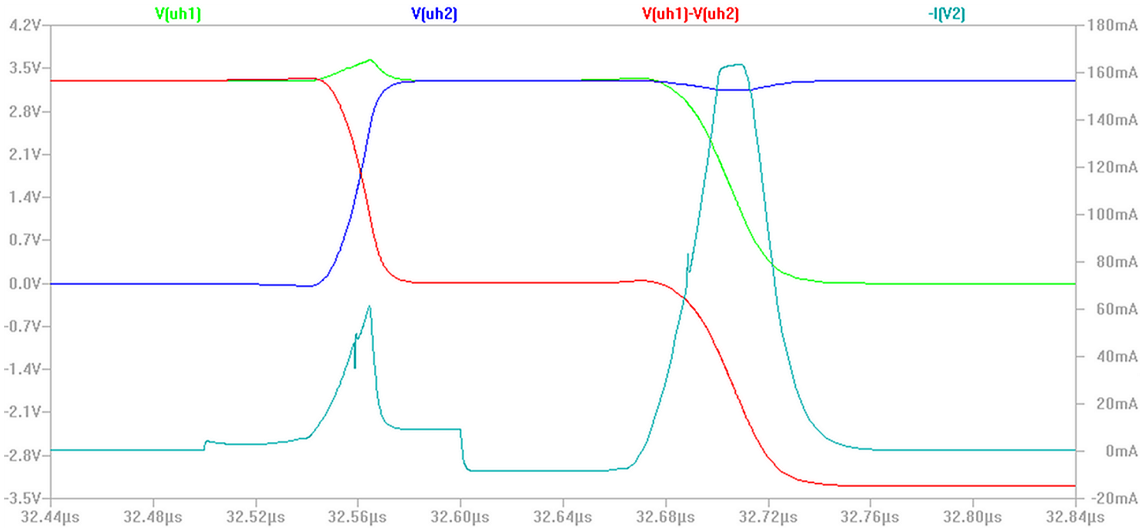

Figure 4.16: Detailed view of a transition at the resonator. The green trace and the blue trace represent the voltages at both pins of the resonator. The red trace represents the voltage difference at the resonator. The turquoise trace represents the current at the voltage source V2.

4.2.6.2 Measurement Circuit

The second part of the ultrasonic module is the measurement circuit. It is used to detect the incoming ultrasonic waves. Figure 4.17 shows the circuit diagram. It can be seen that the measurement circuit consists of two band-pass amplifiers. Both are first order amplifiers. A simplified circuit of a band-pass filter is shown in Figure 4.18. It can be seen that it consists of a high-pass and a low-pass filter. The expected voltage gain can be determined with:

$$g_{U,bp} = \frac{R_f}{R_n} = \frac{R_4}{R_3} = \frac{22k}{1k} = 22$$

The voltage gain of the both amplifiers is:

$$g_{U,tot} = g_{U,bp}^2 = 484 = 53.69\,dB$$

A detailed explanation of band-pass amplifiers can be found in [4].

The AC analysis simulation is shown in Figure 4.19. It must be considered that the input voltage is $U_{in} = 1\,mV$. The value in dB can be calculated with:

$$U_{in,dB} = 20 \cdot \log(U_{in}) = 20 \cdot \log(1mV) = -60\,dB$$

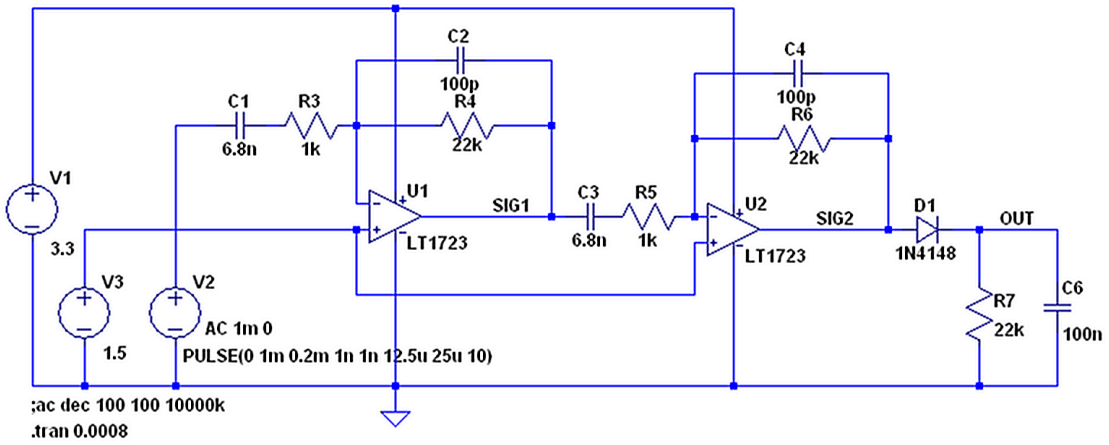

Figure 4.17: Measurement circuit for the incoming ultrasonic waves.

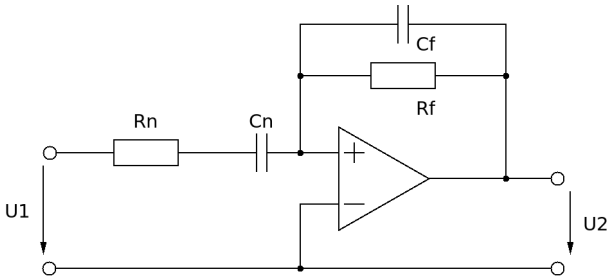

Figure 4.18: First order band-pass circuit from [4].

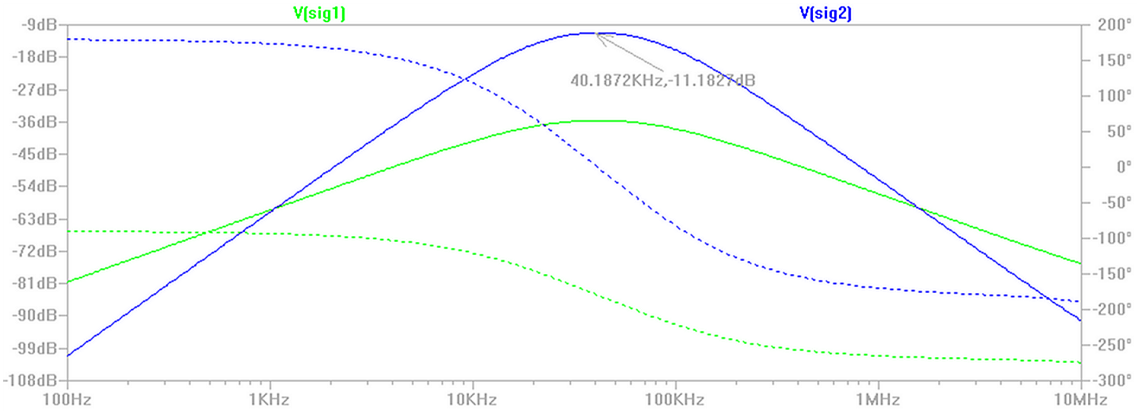

Figure 4.19: AC analysis simulation of the ultrasonic measurement circuit. The green trace is the frequency response of the first amplifier. The blue trace is the frequency response of both amplifiers.

Now the voltage gain in dB can be determined with the simulated output voltage $U_{out,dB} = -11.18\,dB$:

$$g_{U,dB} = U_{out,dB} - U_{in,dB} = -11.18dB + 60dB = 48.82\,dB$$

It equates to a voltage gain of:

$$g_U = 10^{\frac{g_{U,dB}}{20}} = 10^{\frac{48.82}{20}} = 276.06$$

The difference to the calculated one is:

$$g_{diff} = g_{U,tot} - g_{U,dB} = 53.69dB - 48.82dB = 4.88\,dB$$

The reason of the lower simulated voltage gain is the fact that the high-pass and low-pass filter have a lower gain than the calculated one.

The transient simulation of the measurement circuit is shown in Figure 4.20. The

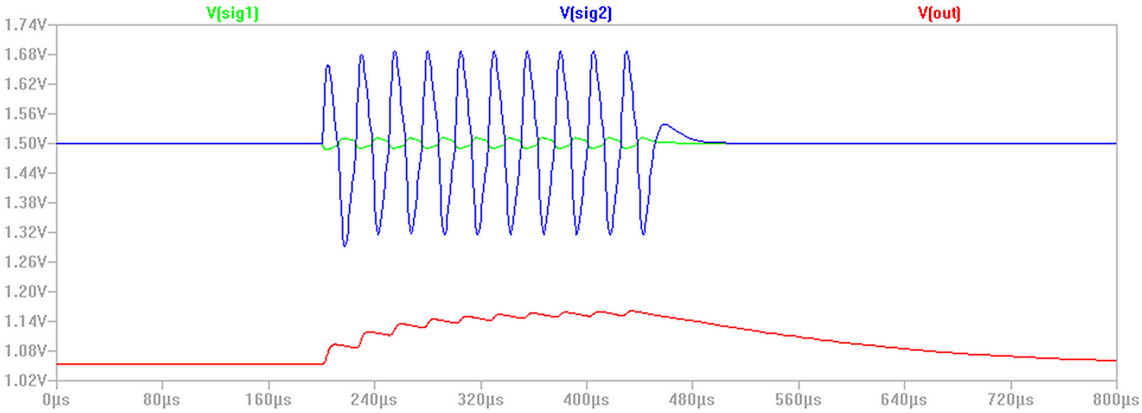

Figure 4.20: Transient simulation of the ultrasonic measurement circuit. The green trace is the output voltage of the first amplifier. The blue trace is the output voltage of the second amplifier. Finally, the red trace is the rectified and smoothed output voltage.

smallest measurable voltage difference of the microcontroller is:

$$U_{meas,min} = \frac{3.3V}{2^{12}} = 0.806\,mV$$

It can be seen that this is enough to detect even small signals.

4.3 Software Implementation

This Chapter shows the implementation of the software of the battery-less WSN river monitoring platform. As mentioned before, the program is written in C++. Therefore, the functionality can be encapsulated in classes. Figure 4.21 shows an overview of the classes and their dependencies.

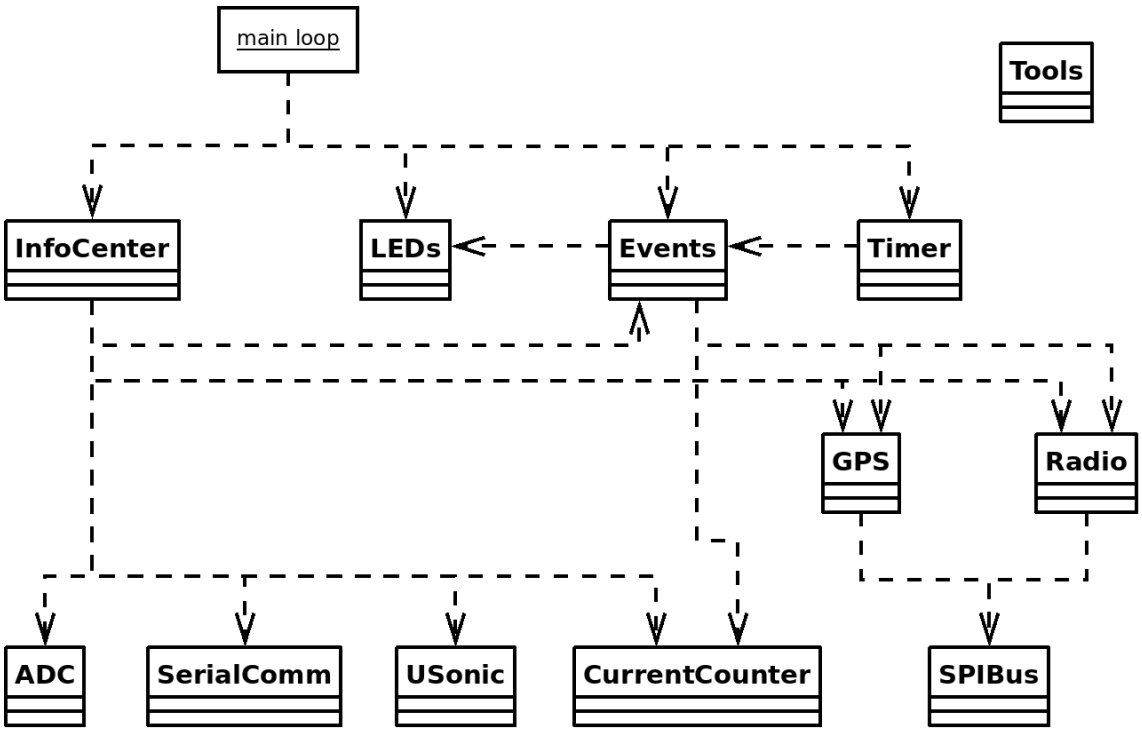

Figure 4.21: Overview of the classes and their dependencies. The class Tools is used by most of the other classes. The dependencies are omitted because of readability.

Each hardware module (e.g. Timer, LEDs, ADC ...) is encapsulated in a single class. These classes represent the functionality of the hardware. They also hide the complexity of the hardware and specific register access. Therefore, the modules can be used very easy.

The basic idea is to keep the microcontroller in sleep mode as long as possible. Only if an event occurs, it is woken up. The microcontroller supports different low-power modes (LPMs), which disable different components. The LPM 3 is used here. It keeps only the timer active during sleep. All other components are switched off. This guarantees very low-power consumption. The timer generates an interrupt and the microcontroller starts working again after a certain time.

4.3.1 Class Description

A short description of each class is listed in the following:

ADC: This class converts analog signals to digital values.

CurrentCounter: This class contains the counting variables of both current counters. They are incremented by interrupt service routines.

Events: This class stores the state of the events of the software.

GPS: This class is used for buffering and decoding the GPS data. It uses the class SPIBus for communication with the hardware module.

InfoCenter: This class gathers all needed information from the other components. After the gathering is completed, the data is sent.

LEDs: This class is used to control the three LEDs of the hardware.

Radio: This class is used for RF communication. It uses the class SPIBus for communication with the hardware module.

SerialComm: This class communicates with the PC.

SPIBus: This class interfaces the local SPI bus.

Timer: This class is used to control the timers of the microcontroller.

Tolls: This class contains useful functions, e.g. software reset.

USonic: This class controls the ultrasonic hardware and measures the received signal.

4.3.2 Operation

The basic operation of the software is described in the following. Figure 4.22 shows the simplified program flow of the main function. This function is called after a reset of the microcontroller and after powering on. The main program activates the LPM 3 of the microcontroller after initializing all modules. Then, the program polls the triggering event and executes the specific instructions after a wake-up from an interrupt service routine (ISR). Then, the LPM 3 is activated again.

The program starts with the gathering process of the data after the activation interval time is over. The following data is measured before the GPS module is activated:

- Solar current counter value (`solarCnt`)
- Mote current counter value (`moteCntBeforGPS`)
- Reduced solar voltage (`vSolarR`)
- Half ultracapacitor voltage (`vCapHalfBeforGPS`)
- Temperature of the microcontroller (`chipTemperatur`)

Then the GPS module is activated. The program activates LPM 3 and waits for the data of the GPS module. After receiving a specified number of positions, the gathering process is continued. The following data is measured:

- Mote current counter value (`moteCntAfterGPS`)
- Half ultracapacitor voltage (`vCapHalfAfterGPS`)

Now the gathering process is completed. This triggers the event "information gathering complete".

This event starts the post processing. Finally, all data is sent and the program activates LPM 3 again. The communication protocol can be found in Section 4.3.4.

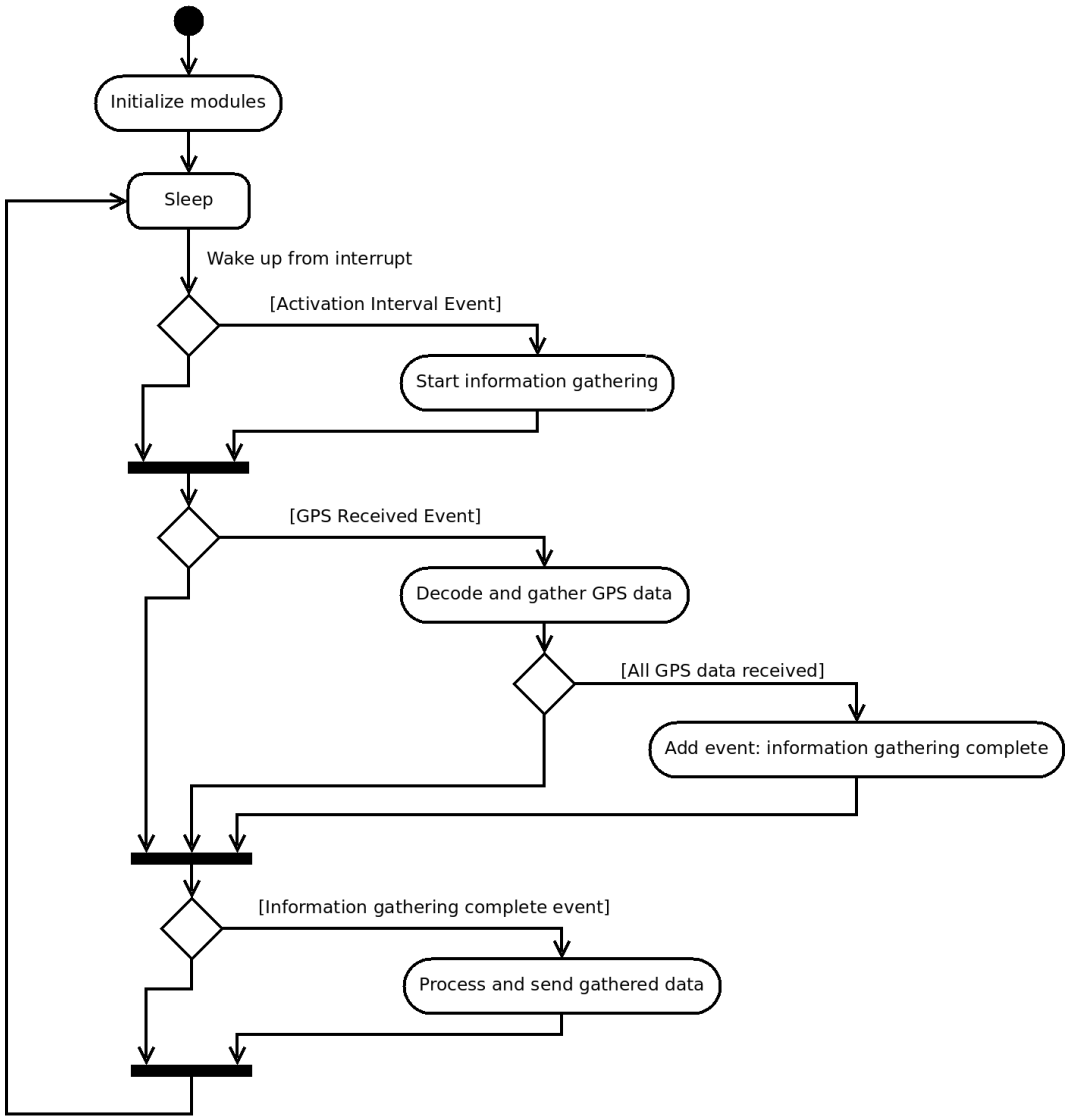

Figure 4.22: Simplified program flow of the main function.

4.3.3 Interrupts

Interrupts are used to detect events during the sleep mode of the microcontroller. Two different interrupts are needed. The first one is the timer interrupt. It is used to determine the time for the activation interval. The second one is the port interrupt. It detects events from the external peripherals. Both current counters, the GPS module and the RF module are connected to an interrupt pin.

4.3.3.1 Timer Interrupt

Figure 4.23 shows the flow of the interrupt service routine of the timer. The timer is

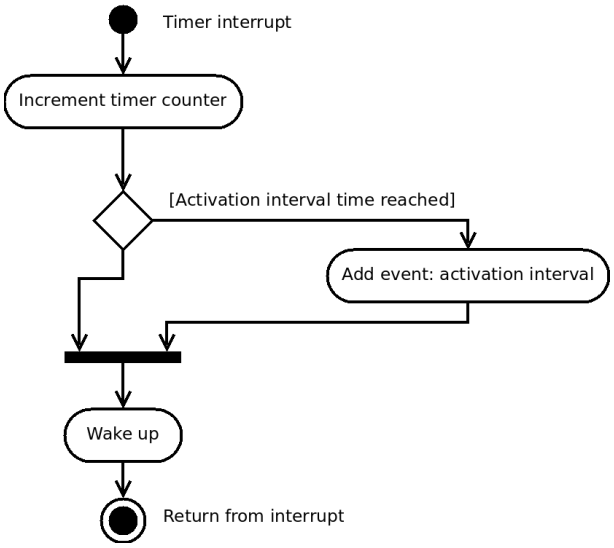

Figure 4.23: Simplified flow of the interrupt service routine of the timer.

programmed to generate a timer interrupt every two seconds. A counter is used to store the number of interrupts. After incrementing, the value of the counter is compared with the activation interval time. If the time is over, the ISR triggers the event "activation interval". Then, the microcontroller is woken up to check whether an event has occurred or not.

4.3.3.2 Port Interrupt

Four different port interrupts are implemented. Figure 4.24 shows the flow of the interrupt service routine of the port. There is no distinction between the triggering input pins. So it must be polled to find out which pin has triggered. First, the current counter pins are polled. If one of them has generated a pulse, the respective current counter variable is incremented. Then, the RF communication interrupt is polled. The RF module generates this interrupt if it has received a message. Finally, the GPS communication interrupt pin is polled. If the UART of the GPS module has received a character, it generates an interrupt pulse. The ISR reads the character via the SPI bus and checks if a line has finished. If so, the event "GPS received" is triggered and the microcontroller is woken up.

4.3.4 Communication Protocol

The communication protocol is explained in this Section. The mote sends a packet to the base station each activation interval. The basic 802.15.4 data packet format can be found in Table 4.1. The sender and the receiver are located in the same personal area network (PAN). The checksum of the data packet is calculated automatically by the RF module.

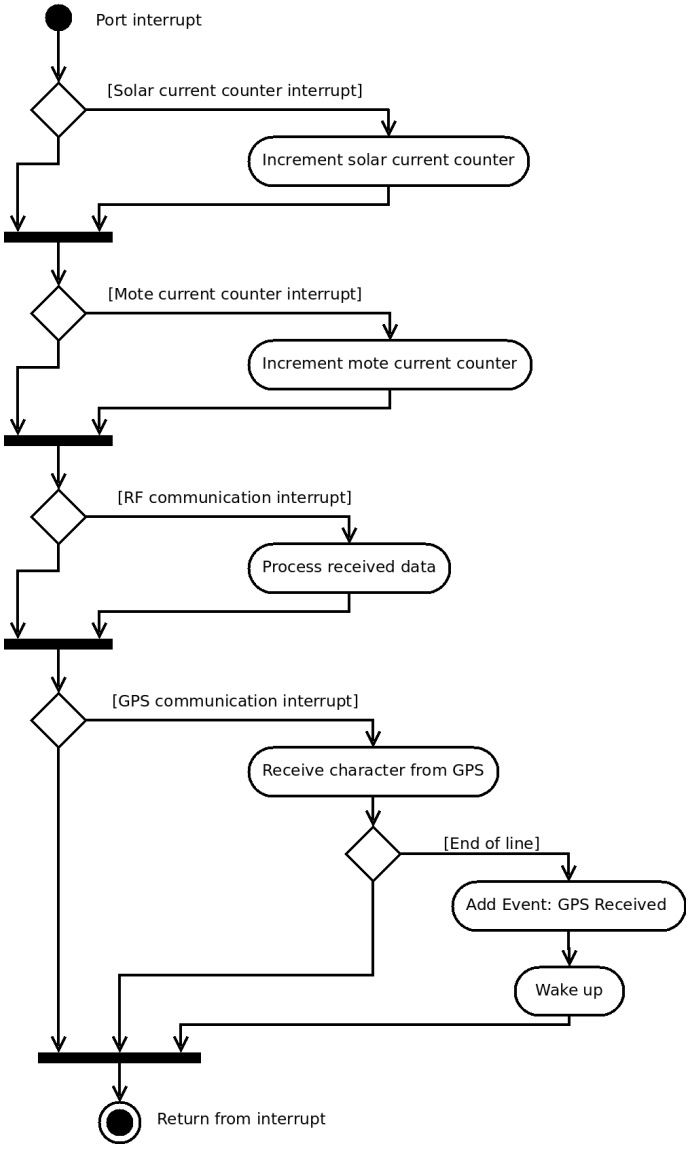

Figure 4.24: Simplified flow of the interrupt service routine of the port.

Description:		Frame header	Sequence number	Dest. PAN	Dest. addr.	Src. PAN	Src. addr.	Payload	Check sum
Bytes:		2	1	2	2	2	2	n	2

Table 4.1: Frame format of the 802.15.4 data packet.

The payload of the packet is an ASCII formatted data string. Therefore, it can be read easily. The format of the data string is:

```
RM10,<activation interval>,<solar count>,<mote count 1>,<mote count 2>,
<supply voltage>,<solar voltage>,<cap.  voltage 1>,<cap.  voltage 2>,
<chip temperature>,<valid GPS count>,<mean altitude>,<usonic>
```

The meaning of each data field is described in Table 4.2.

Data Field	Description
activation interval	Time of activation interval in seconds
solar count	Value of the solar current counter
mote count 1	Value of the mote current counter before GPS activation
mote count 2	Value of the mote current counter after GPS activation
supply voltage	Supply voltage in [mV]
solar voltage	Solar voltage in [mV]
cap. voltage 1	Voltage of the ultracapacitors in [mV] before GPS activation
cap. voltage 2	Voltage of the ultracapacitors in [mV] after GPS activation
chip temperature	ADC value of the on chip temperature measurement
valid GPS count	Number of valid GPS signals during GPS activation
mean altitude	Average altitude of the valid GPS altitude measurements
usonic	Measured distance of the ultrasonic measurement in [mm]

Table 4.2: Description of the data fields.

4.4 Design flow and Start-up

This Section shows the design flow of creating a new application for RiverMote. As described in Section 3.5, the development environment Code Composer Studio Core Edition (version: 4.0.2.01003) is used to create C or C++ applications.

All developed applications can be found in the directory `software\ccworkspace`. The application `RiverMoteBasicTest` uses the most hardware components of the RiverMote. Therefore, it is a good application to learn from and can be used as the basis for feature applications. The application `RiverMoteBaseStation` receives packets from other motes and sends the data to the PC.

If the classes of the `RiverMoteBasicTest` application are used in new projects, the C system stack size and the heap size for C/C++ dynamic memory allocation must be increased to at least 2048 bytes. This is needed because the objects of the classes are instanced during the program start-up. These settings can be found under: *Project Properties → C/C++ Build → Tool Settings → MSP430 Linker → Basic Options.*

The first step of creating a new application is to think about which hardware components are needed. Then, the specific classes can be included in the new project. After writing the application specific code, the program can be compiled. It is necessary to create a

Texas Instruments®hex-file. This can be enabled under: *Project Properties → C/C++ Build → Build Steps → Post-build step → Apply Predifined Step → Create flash image: TI-TXT*. This file is needed to transmit the machine code to the microcontroller.

Before programming the microcontroller, the RiverMote has to be connected to the PC. Therefore, a standard USB cable can be used (Type A to Type B Mini). The RiverMote needs a Virtual Com Port Driver to be able to communicate with the PC. This driver can be found in the zip file:
`software\FTDI USB Driver CDM 2.06.00 WHQL Certified.zip`.
Note that before connecting the RiverMote to the PC it must be ensured that it is supplied either from the USB module or from the EHS. Therefore, the jumper `USBPWR` (mote) and `SUPVCC` (EHS) must be set properly. The hardware may be damaged if both jumpers are set and the USB cable is connected.

A Java application has been written to transmit the hex-file to the microcontroller. This application is called BSLprogrammer and it can be found in the directory:
`software\eworkspace\BSLprogrammer`.
The current version is 1.0. It uses the open source library rxtx library to access the serial interface of the PC (version 2.1-r7). It has been only tested under WindowsXP. The application `RiverMoteBasicTest` includes also a patch file that is used to transmit the generated hex-file to the microcontroller (`zz_programm.bat`). It starts the BSLprogrammer automatically. The syntax to start the BSLprogrammer is: `java -jar BSLprogrammer.jar <COM port> <hex-file>`.

The BSLprogrammer initializes the BSL of the microcontroller by sending the BSL entry sequence. Then, the microcontroller is unlocked by sending the password. The standard password consists of 32 bytes. Each byte has the value `0xFF`. The unlocking is necessary to be able to write into the flash memory of the microcontroller. Then, the machine code is transmitted. Finally, the microcontroller is reset to start normal operation.

A second Java application has been developed to communicate with the RiverMote. It is called RiverMoteListener and it can be found in the directory:
`software\eworkspace\RiverMoteListener`.
It is configured to open the serial port COM4. This can only be changed in the source code. The RiverMoteListener receives the data of the connected RiverMote and displays it. All received data is stored in the log-file `C:\RiverMoteLogAll.txt`. The data of the mote application `RiverMoteBasicTest` is sent in a specific format as described in Section 4.3.4. This protocol is processed by the RiverMoteListener. For example, it calculates the current from the current counter value and also the temperature. These calculated values are displayed for a better understanding of the state of the RiverMote. The raw data values are stored in the separate log-file `C:\RiverMoteLog.txt`.

The measurement data of the log file can be analyzed with a MATLAB script. The scripts are written in MATLAB R2007a. An example script can be found in:
`measurements\longtime\2010-02-19 longtime\longtimeanalysis.m`

The RiverMote application starts immediately after programming. If this should be omitted, the USB connector or the EHS connector must be removed after programming.

The ultracapacitors can be charged by an external power supply. Therefore, the solar cell must be disconnected. The power supply is connected to the solar cell connector of the EHS. The maximum charge current is $200\,mA$. After charging, the power supply can be disconnected.

Table 4.3 shows the content of the directories of this master's thesis.

Directory	Content
datasheets	Datasheets of the components of the hardware
doku	LaTeX source code and pdf of the documentation
hardware	Schematic, PCB layout file and part list of the RiverMote hardware
images	Images of the prototype hardware
infos	Additional information
matlab	MATLAB scripts for various calculations
measurements	Measurement data and MATLAB scripts for analysis
papers	Relevant papers for this master's thesis
simulation	Simulation files of the implemented circuits
software	RiverMote applications, BSLprogrammer and RiverMoteListener

Table 4.3: Content of the directories of this master's thesis.

5 Experimental Results

This Chapter shows the results of the measurements of the WSN platform hardware.

5.1 Ultracapacitor

The ultracapacitor is the energy storage unit of the RiverMote. Therefore, it should have a low leakage current. Figure 5.1 shows the measurement of the voltage and the charging

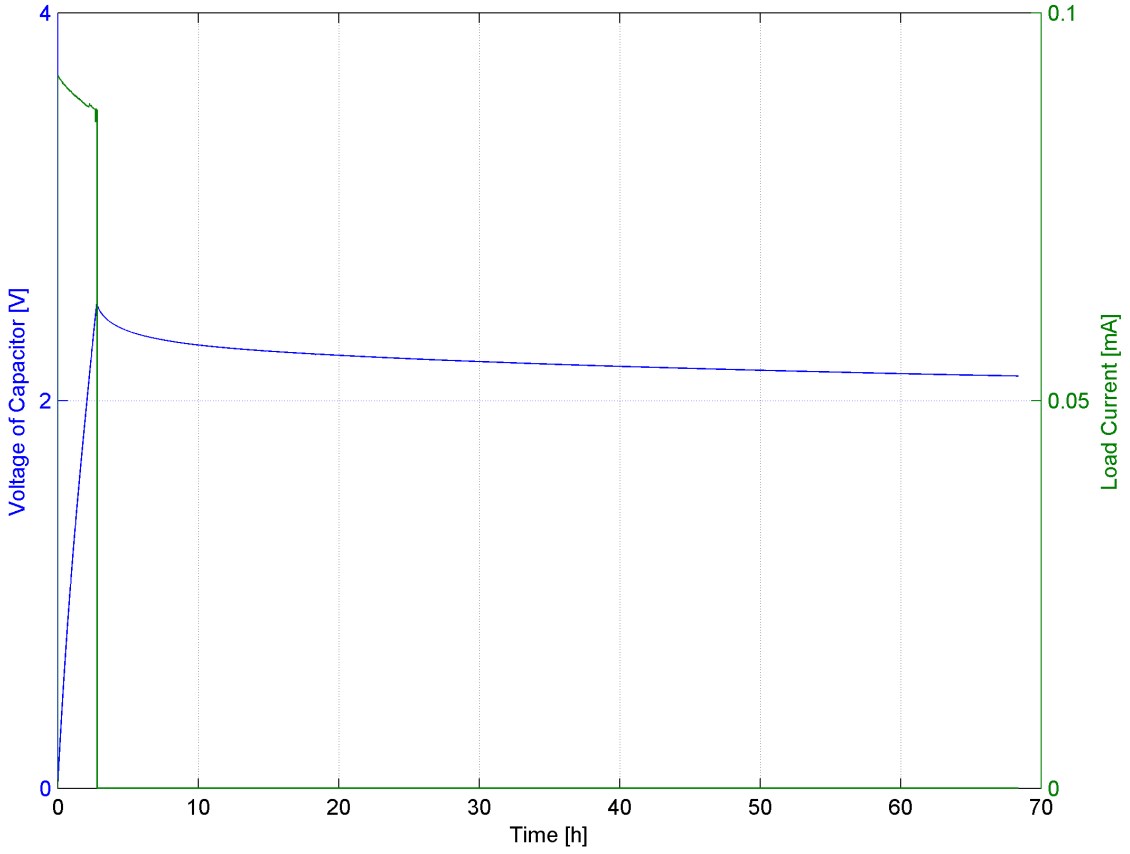

Figure 5.1: Long-term measurement of a single ultracapacitor BC310 P250 T10 from Maxwell with a capacitance of $C = 310\,F$. The voltage of the ultracapacitor and the charging current have been measured for nearly 3 days. After charging the ultracapacitor to a voltage of $2.5\,V$, the power supply was disconnected.

current of a single ultracapacitor. The measurement hardware consists of the National Instruments®DAQ NI PXI-6221. The ultracapacitor is connected to a current source.

One analog input channel of the measurement device is used to measure the voltage of the ultracapacitor. A second channel is used to measure the voltage drop at a shunt resistor. So, the charging current can be measured indirectly. After charging, the ultracapacitor is disconnected from the current source. Therefore, the measured current is equal to zero.

The average current into the ultracapacitor during the charging phase (0 to 2.8 h) was 89.25 mA. The energy delivered from the power supply during this phase was $E_{supply} = 1246.62\,J$. It can be calculated with:

$$E_{supply} = \sum_{n=1}^{N} (U_{cap,n} \cdot I_{charge,n} \cdot \Delta t)$$

N is the number of samples, $U_{cap,n}$ is the voltage of the ultracapacitor at the sample n, $I_{charge,n}$ is the charging current of the ultracapacitor at the sample n, and Δt is the time between two samples $(1/samplingrate)$.

It can be seen that the initial voltage decrease is higher than the decrease after 16 hours. Figure 5.2 shows the leakage current after disconnecting the power supply. The leakage

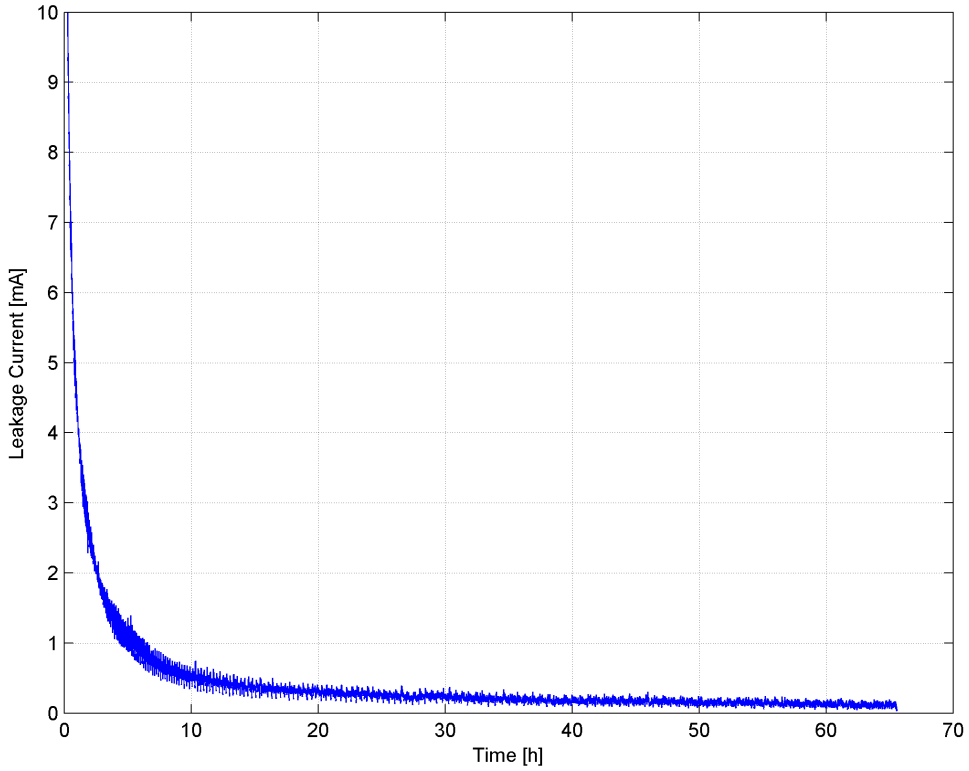

Figure 5.2: Leakage current measurement of a single ultracapacitor BC310 P250 T10 from Maxwell with a capacitance of 310 F. The ultracapacitor was charged to a voltage of 2.5 V and was disconnected from the power supply.

current can be calculated with the measured voltage:

$$I_{leakage} = C \cdot \frac{\Delta U_{cap}}{\Delta t} = C \cdot (U_{cap,n+1} - U_{cap,n}) \cdot samplingrate$$

The average leakage current during the whole measurement was $0.487\,mA$. The expected leakage current from the data sheet was only $0.45\,mA$ [26]. However, the significant value of the leakage current is the average leakage current of the first 16 hours after disconnecting the power supply. This time must be bridged with the ultracapacitor. The average leakage current during this interval was $1.398\,mA$.

It must be considered that the ultracapacitor was disconnected immediately after reaching the maximum voltage of $2.5\,V$. A second measurement was done. The maximum voltage was kept constant for one day. After this time, the ultracapacitor was disconnected and the leakage current was measured. The result is shown in Figure 5.3.

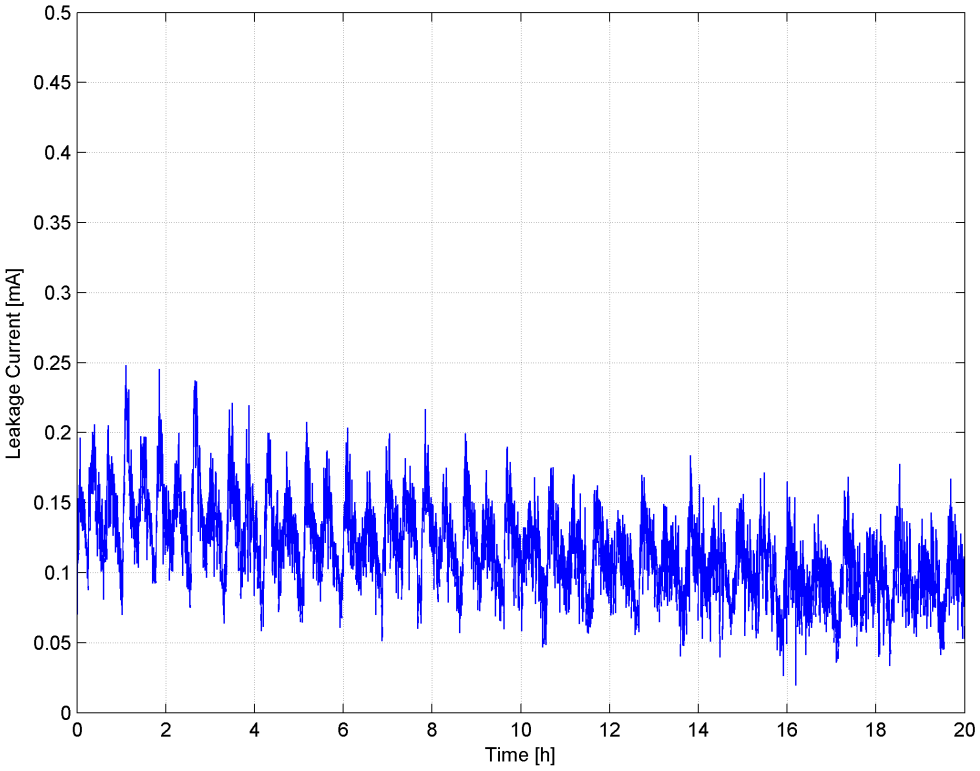

Figure 5.3: Leakage current measurement of the ultracapacitor BC310 P250 T10 from Maxwell with a capacitance of $310\,F$. The leakage current was measured after keeping the voltage at the ultracapacitor constant for one day.

The average leakage current at the first 16 hours is $0.121\,mA$. This is a very good result because it is only a fourth of the value of the data sheet. However, it must be considered that the maximum voltage at this measurement was $2.3\,V$. Therefore, the real value is between the measured values of $0.121\,mA$ and $1.398\,mA$. The real value depends also on the temperature, which was not measured here. This would go beyond the scope of this master's thesis.

The long-term measurements will show if the ultracapacitors are suited to supply the RiverMote.

5.2 Balancing Circuit

The balancing circuit is needed to keep both ultracapacitors at the same voltage. Figure 5.4 shows measurement setup. The voltage $U1$ is kept a constant value. The voltage $U2$

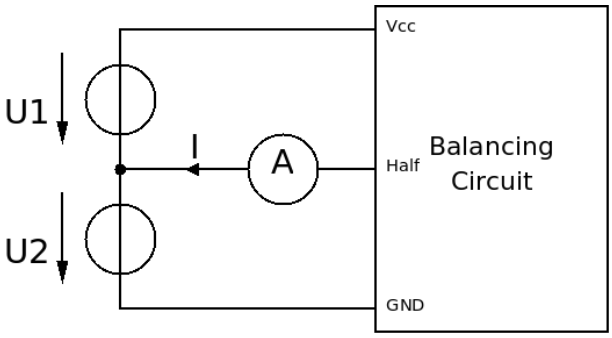

Figure 5.4: Setup for the measurement of the balancing current.

is varied to get the wanted voltage difference. An ampere meter is used to measure the balancing current.

Figure 5.5 shows the balancing current measured for three different voltages of $U1$ (fixed voltage). It can be seen that this balancing current is much higher than the calculated on.

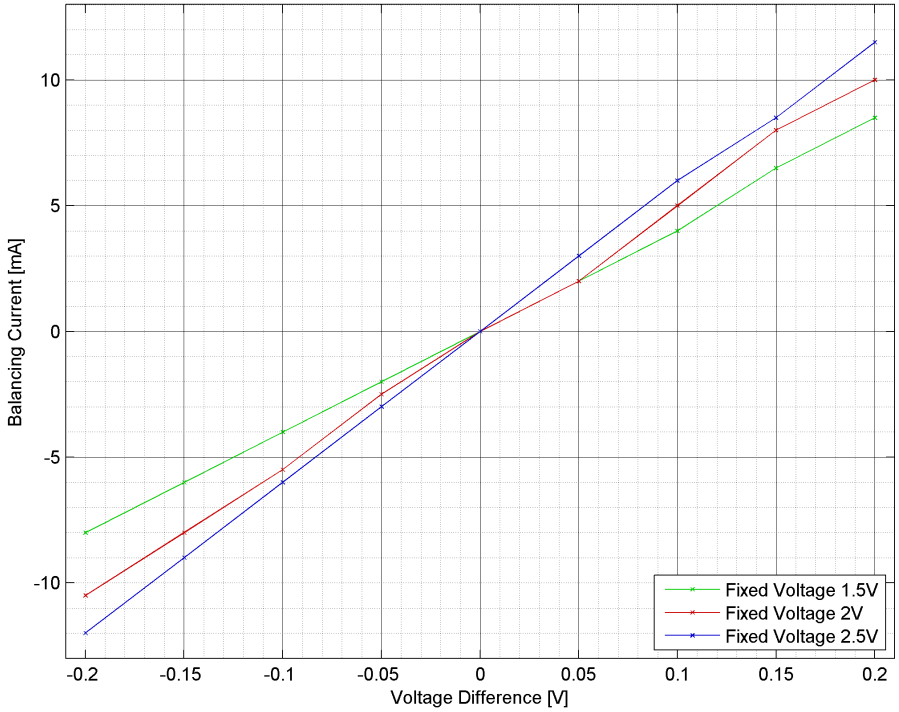

Figure 5.5: Measurement of the balancing current for three different fixed voltages.

For example, the calculated balancing current at a voltage difference of $0.2\,V$ is:

$$I_{bal,calc,0.2V} = 3.6\,mA$$

The average balancing current at a voltage difference of $0.2\,V$ is:

$$I_{bal,meas,0.2V} = 10\,mA$$

The reason is that the calculation is only an estimation of the lower limit. Now the maximum charging current can be recalculated as described in Section 4.1.3:

$$t_{charge} = \frac{\Delta Q}{I_{bal,0.4V}} = \frac{\Delta Q}{I_{bal,meas,0.2V} \cdot 2} = \frac{74.4As}{20mA} = 3720, s = 1.03\,h$$

The maximum charging current is:

$$I_{charge} = \frac{Q_{tot}}{t_{charge}} = \frac{744As}{3720} = 200\,mA$$

This means that the maximum charging current should not exceed $200\,mA$. However, this value is the limit for a complete charging process. This means the initial voltage of the ultracapacitor is $0\,V$. During normal operation, such a low voltage cannot be reached. Therefore, the maximum charging current increases and the selected solar cells can be used.

A second measurement was done to show the balancing process of two ultracapacitors with different initial voltages. It demonstrates the functionality of the balancing circuit. Figure 5.6 displays the voltages of each capacitor. The charging current was $50\,mA$. It was interrupted after two hours to prevent damage of the ultracapacitors. The voltage ratio can be calculated with

$$ratio = \frac{U_{ucap1}}{U_{ucap2}}$$

and is shown in Figure 5.7. It can be seen that the ratio function corresponds approximately to a charging function of a capacitor. The reason is the lower balancing current at lower voltage differences.

The charge current of the capacitors can be calculated by assuming the capacity of both ultracapacitors with $C_{ucap} = 310\,F$:

$$I_{charge,n} = \frac{\Delta Q_{ucap,n}}{\Delta t_n} = \frac{C_{ucap} \cdot \Delta U_{ucap,n}}{\Delta t_n} = \frac{C_{ucap} \cdot (U_{ucap,n+1} - U_{ucap,n})}{t_{n+1} - t_n}$$

The difference of the charging current of both ultracapacitors is equivalent to the balancing current:

$$I_{bal,n} = I_{charge,n,ucap1} - I_{charge,n,ucap2}$$

This current depends on the voltage difference and is shown in Figure 5.8.

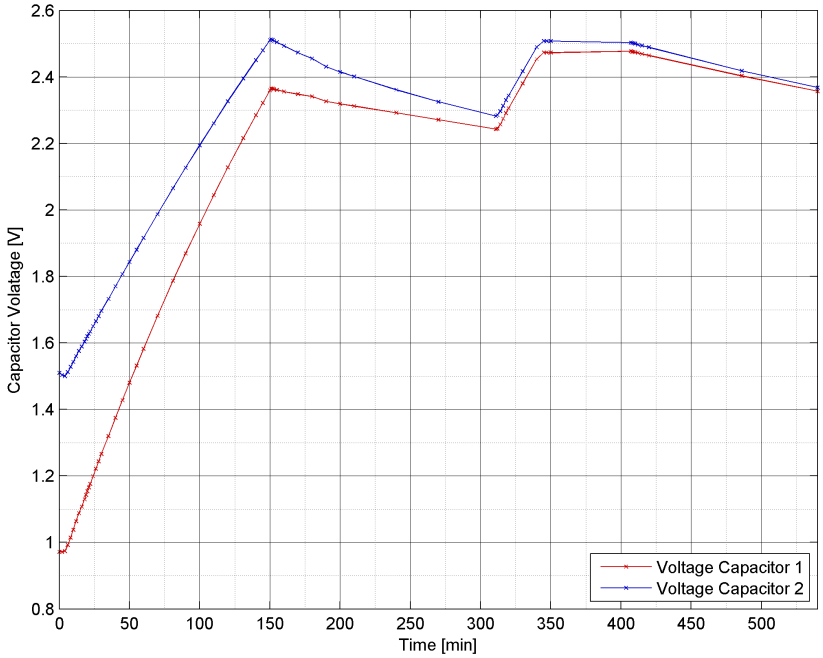

Figure 5.6: Voltage of both ultracapacitors during balancing process.

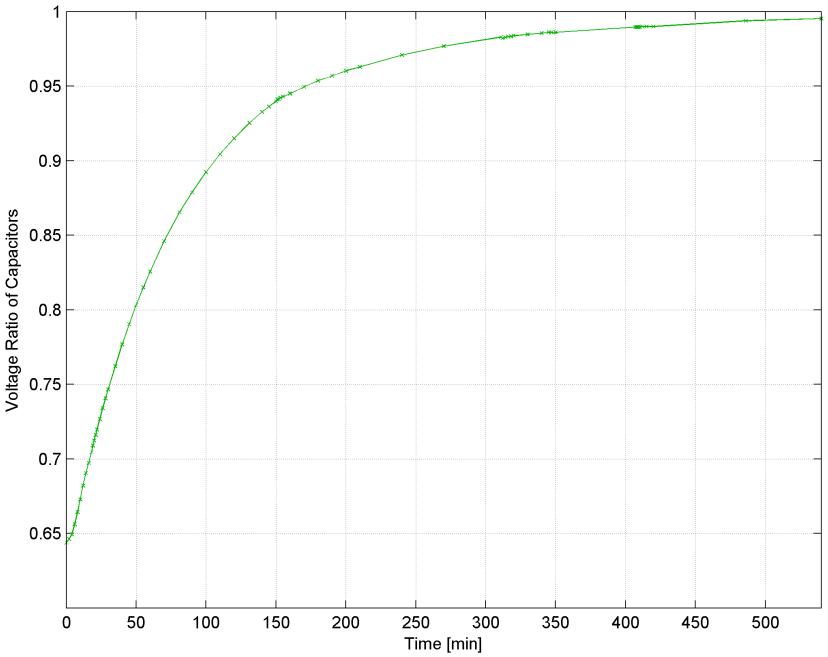

Figure 5.7: Voltage ratio of both ultracapacitors during balancing process.

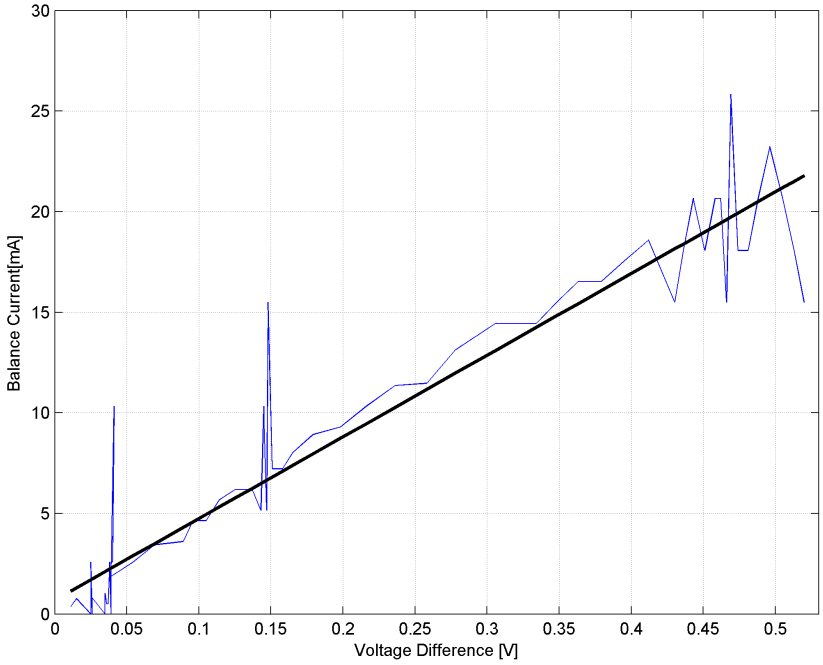

Figure 5.8: Balancing current depending on the voltage difference of the ultracapacitors.

5.3 Current Counters

This Section presents the results of the measurements of both current counters. Section 5.3.1 and 5.3.2 show the measurements of the solar current counter and the mote current counter.

5.3.1 Solar Current Counter

Figure 5.9 shows the setup of the solar current counter measurement. The EHS is supplied with a constant voltage of $U = 3.2\,V$. This voltage is connected to the input of the ultracapacitors. The variable voltage source U_{var} is used to set a given current I. This current represents the current of the solar cell. The measurement resistor $R_{meas} = 10\,\Omega$ is used to measure the voltage drop U_{meas} at this resistor. This is needed, because the resistor limits the measurement current and it can be adjusted more exactly.

The measurement current I flows also through the shunt resistor $R_{solar} = 0.33\,\Omega$ of the EHD. The solar current counter uses this resistor to measure the solar current. As described in Section 4.1.5.2, the current counter integrates the voltage drop of the shunt resistor. The measurement of the integration time $t_{integr,solar}$ was done with the oscilloscope unit DSO-2090 from Voltcraft®. The input channel was connected to the integration capacitor of the solar current counter.

Figure 5.10 shows one integration cycle of the solar current counter. The measured time of one cycle is $t = 381.11\,ms$ and the difference of the integration voltage is $U_{diff,meas} = 3.03\,V$. The simulated voltage difference is $U_{th,diff} = 3.012\,V$ and the simulated time of one cycle is $t_{cl,sim} = 371\,ms$ (see Section 4.1.5.2). These are very good results and

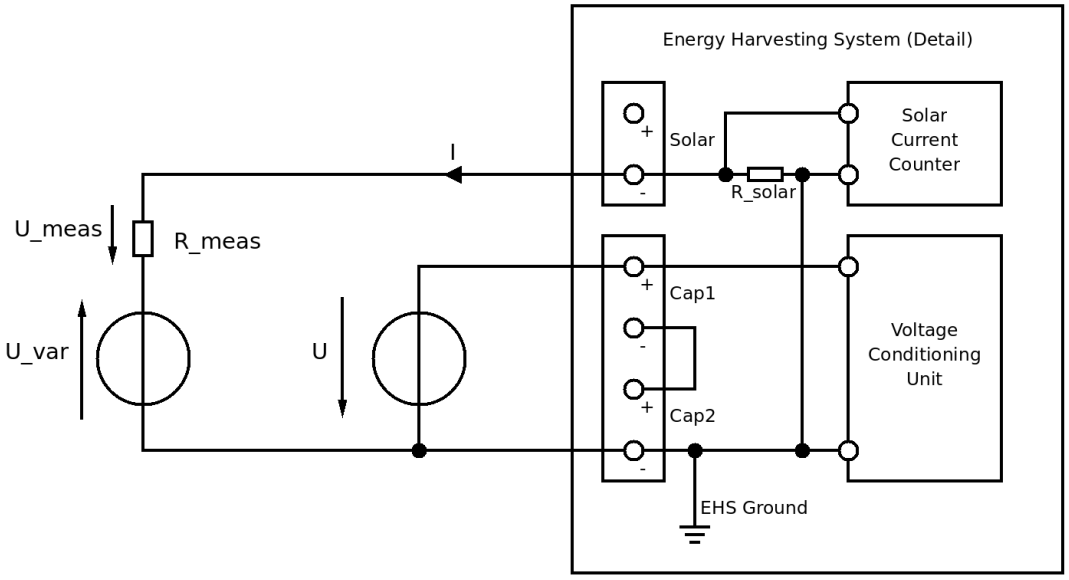

Figure 5.9: Setup for the measurement of the solar current counter.

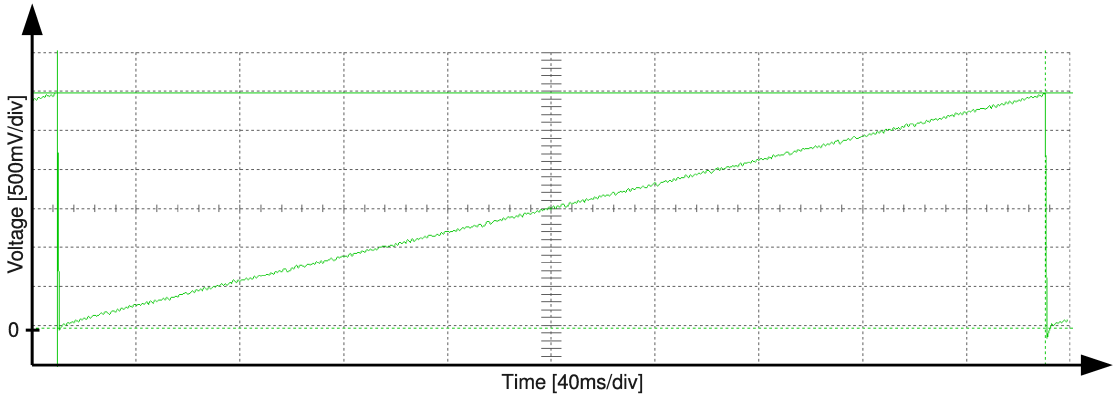

Figure 5.10: One integration cycle of the solar current counter at a solar current of $I = 8.3\,mA$.

they show that the Schmitt trigger and the MOSFET of the solar current counter works properly.

The equivalent charge of one pulse can be calculated with:

$$Q_{pulse,solar} = I \cdot t_{integr,solar}$$

In this case it is:

$$Q_{pulse,solar} = 8.3mA \cdot 381.11ms = 3.16\,mAs$$

The error to the calculated charge per pulse is:

$$f_{err,pulse,solar} = \frac{Q_{chargecnt,solar} - Q_{pulse,solar}}{Q_{pulse,solar}} = \frac{3.012mAs - 3.16mAs}{3.16mAs} = -4.68\,\%$$

Figure 5.11 shows the measurements of the solar current counters of all three prototypes. Since the current is measured indirectly by the voltage drop U_{meas} at the measurement

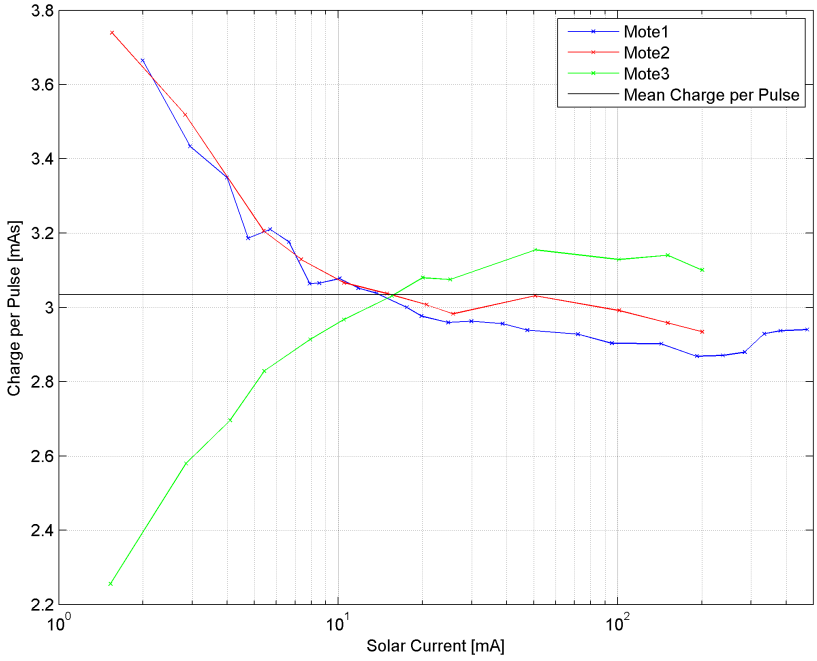

Figure 5.11: Equivalent charge of one pulse depending on the solar current. The average charge per pulse is $Q_{solar,pulse,mean} = 3.049\,mAs$

resistor R_{meas}, the equivalent charge can be calculated with:

$$Q_{pulse,solar} = \frac{U_{meas}}{R_{meas}} \cdot t_{integr,solar}$$

It can be seen that the error of the current counter is higher at lower values of the solar current. The reason is the influence of leakage currents of the MOSFET, the operational amplifiers and the integration capacitor. These leakage currents have a higher influence on the current counter at low values of the solar current.

The average equivalent charge of one pulse is $Q_{solar,pulse,mean} = 3.049\,mAs$ of all three motes. The difference to the calculated charge per pulse is:

$$\Delta Q_{solar} = Q_{chargecnt,solar} - Q_{solar,pulse,mean} = 3.012mAs - 3.049mAs = -0.037\,mAs$$

$$f_{err,charge,solar} = \frac{Q_{chargecnt,solar} - Q_{solar,pulse,mean}}{Q_{solar,pulse,mean}} = \frac{3.012mAs - 3.049mAs}{3.049mAs} = 1.2\,\%$$

The error depending on different solar currents is shown in Figure 5.12. It is referring to

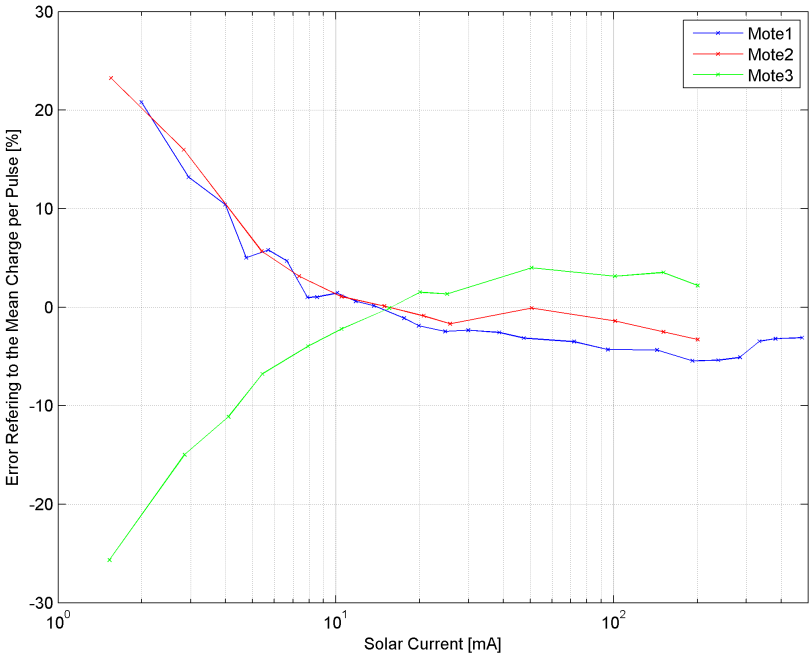

Figure 5.12: Error of the equivalent charge of one pulse depending on the solar current.

the average equivalent charge of one pulse. This value is used for all following calculations to enhance the accuracy. It can be seen that the error is more than 20 % at low solar currents. However, it can be said that the solar current counter works properly at high enough solar currents.

The solar current is higher than $10\,mA$ during the daytime even at bad weather conditions. Therefore, the error of the solar current counter is better than 10 % during the daytime.

5.3.2 Mote Current Counter

Figure 5.13 shows the setup of the mote current counter measurement. The EHS is supplied with a constant voltage of $U = 3.2\,V$. This voltage is connected to the input of the ultracapacitors. The variable voltage source U_{var} is used to set a given current I. This current represents the current of the mote. The measurement resistor $R_{meas} = 10\,\Omega$ is used to measure the voltage drop U_{meas} at this resistor. This is needed, because the resistor limits the measurement current and it can be adjusted more exactly.

The measurement principle is the same as those of the solar current counter measurement. The measurement current I flows through the shunt resistor $R_{mote} = 0.47\,\Omega$ of the EHD. The mote current counter uses this resistor to measure the mote current. As described in Section 4.1.6.1, the current counter integrates the voltage drop of the shunt resistor.

The measurement of the integration time $t_{integr,mote}$ was done with the oscilloscope unit DSO-2090 from Voltcraft®, too. The input channel was connected to the integration capacitor of the mote current counter.

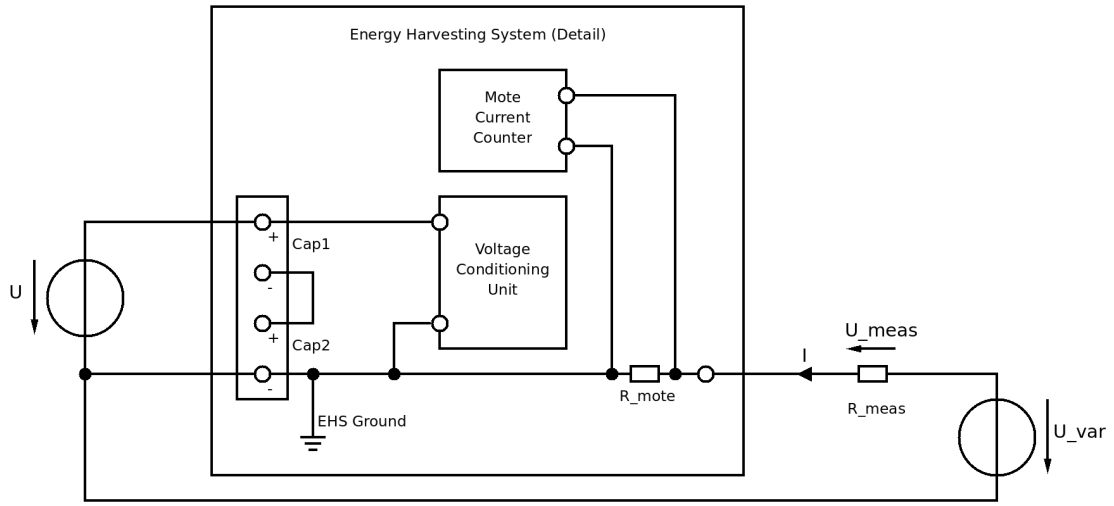

Figure 5.13: Setup for the measurement of the mote current counter.

Figure 5.14 shows one integration cycle of the mote current counter. The measured time

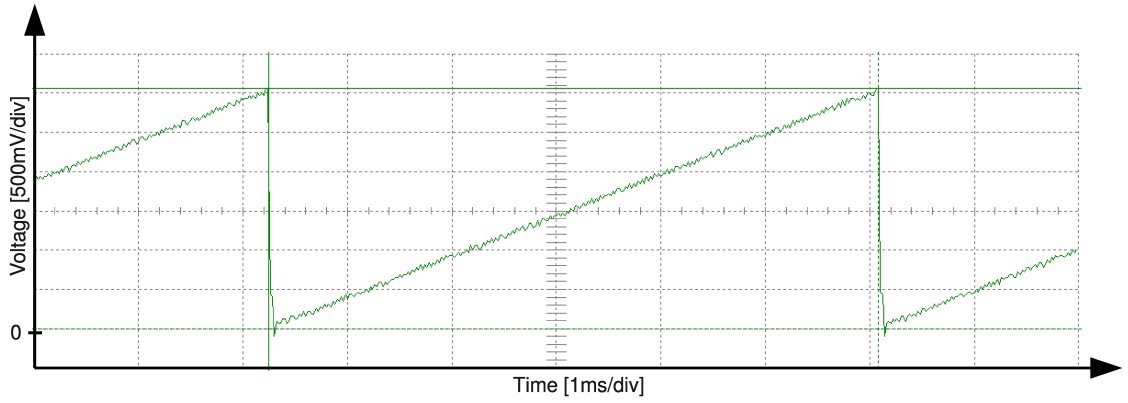

Figure 5.14: One integration cycle of the mote current counter at a mote current of $I = 25\,mA$.

of one cycle is $t = 5.84\,ms$ and the difference of the integration voltage is $U_{diff,meas} = 3.07\,V$. The simulated voltage difference is $U_{th,diff} = 3.012\,V$ and the simulated time of one cycle is $t_{cl,sim} = 5.7\,ms$ (see Section 4.1.5.2). These are very good results and they show that the Schmitt trigger and the MOSFET of the mote current counter works properly, too.

The equivalent charge of one pulse can be calculated in the same way here:

$$Q_{pulse,mote} = I \cdot t_{integr,mote}$$

In this case it is:

$$Q_{pulse,mote} = 25mA \cdot 5.84ms = 146\,\mu As$$

The error to the calculated charge per pulse is here:

$$f_{err,pulse,mote} = \frac{Q_{chargecnt,mote} - Q_{pulse,mote}}{Q_{pulse,mote}} = \frac{128.7\mu As - 146\mu As}{146\mu As} = -11.85\,\%$$

Figure 5.15 shows the measurements of the mote current counters of all three prototypes. The current is measured indirectly by the voltage drop U_{meas} at the measurement resistor

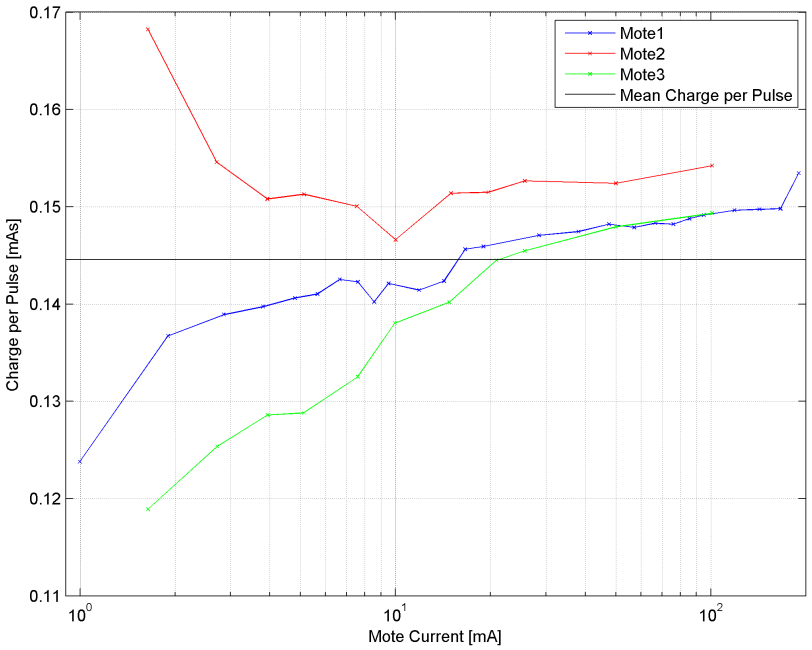

Figure 5.15: Equivalent charge of one pulse depending on the mote current. The average charge per pulse is $Q_{mote,pulse,mean} = 144.3, \mu As$

R_{meas}. The equivalent charge can be calculated with:

$$Q_{pulse,mote} = \frac{U_{meas}}{R_{meas}} \cdot t_{integr,mote}$$

It can be seen that the error of the mote counter is higher at lower values of the mote current. The reason is the influence of leakage currents of the MOSFET, the operational amplifiers and the integration capacitor, too. These leakage currents have a higher influence on the current counter at low values of the mote current.

The average equivalent charge of one pulse is $Q_{mote,pulse,mean} = 144.3\,\mu As$ of all three motes. The difference to the calculated charge per pulse is:

$$\Delta Q_{mote} = Q_{chargecnt,mote} - Q_{mote,pulse,mean} = 128.7\mu As - 144.3\mu As = -15.6\,\mu As$$

It equates to a relative error of:

$$f_{err,charge,mote} = \frac{Q_{chargecnt,mote} - Q_{mote,pulse,mean}}{Q_{mote,pulse,mean}} = \frac{128.7\mu As - 144.3\mu As}{144.3\mu As} = 10.81\,\%$$

The error depending on different mote currents is shown in Figure 5.16. It is referring to the average equivalent charge of one pulse. This value is used for all following calculations to enhance the accuracy. It can be seen that the error is up to 20 % at low mote currents. However, it can be said that the mote current counter works properly at high enough mote currents. Due to the fact that the current of the mote is about $1.5\,mA$ in LPM 3, the error of the current measurement is 20 %.

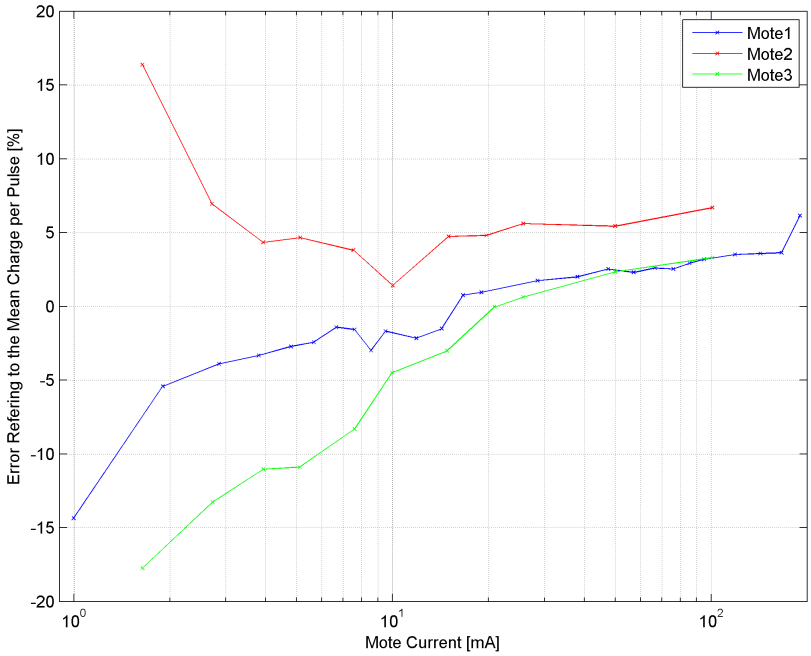

Figure 5.16: Error of the equivalent charge of one pulse depending on the mote current.

5.4 EHS Efficiency

This Section shows the results of the efficiency measurements of the EHS. The measurement hardware consists of the National Instruments®DAQ NI PXI-6221. The main advantage of this measurement device is the high number of input channels. Eight differential input channels can be used with a collective sample rate of $250\,kHz$ and each with a minimal input range from $-200\,mV$ to $200mV$ [33]. Figure 5.17 shows the setup of the efficiency measurement.

Five differential input channels are necessary here. The sample rate is reduced to $1\,kHz$ to keep the amount of measurement data low.

The EHD is emulated by a constant current source. Therefore, the measurement setup conditions can be reconstructed.

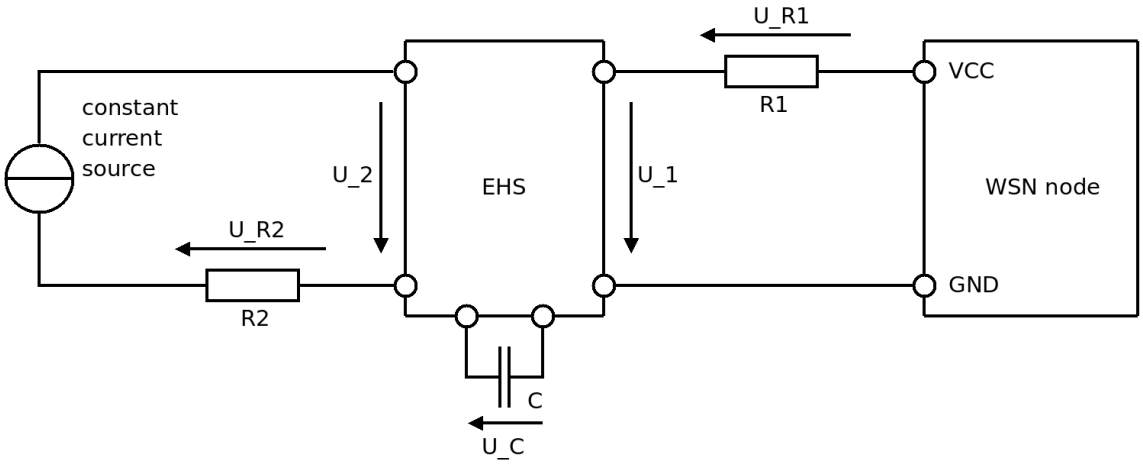

Figure 5.17: Setup of the efficiency measurement.

The input voltage U_2 and the output voltage U_1 can be measured directly. One differential input channel of the measurement device is used to measure each voltage. The currents can only be measured indirectly. Therefore, a shunt resistor is needed. The voltage drop of the shunt resistor is measured with a differential input channel of the measurement device, too. The shunt resistor between the current source and the EHS is placed at low side. The shunt resistor between the EHS and the mote is placed at high side. The reason is the voltage drop at the shunt resistor. The output voltage of the EHD U_1 is constant. If the resistor is placed at low side, the voltage drop would influence the internal voltage measurements of the mote. If it is placed at high side, only the supply voltage of the mote is reduced. This can be corrected with the measurement of the supply voltage.

The input power and the output power can be calculated with:

$$P_{input} = U_2 \cdot \frac{U_{R_2}}{R_2}$$

$$P_{output} = U_1 \cdot \frac{U_{R_1}}{R_1}$$

The efficiency of the EHS is:

$$\eta_{EHS} = \frac{P_{output}}{P_{input}}$$

Finally the stored energy can be calculated with:

$$E_{stored} = \frac{1}{2} \cdot C \cdot U_C^2$$

A measurement program was written specially for the following measurements. Two thresholds can be set to control the voltage of the ultracapacitors. This is needed to measure the efficiency of the EHS at different voltages of the ultracapacitors. If the upper threshold is reached, a high power mode is activated and all power intensive modules (GPS,

communication module) of the mote under test are switched on. This leads to a discharge of the ultracapacitors. If the lower threshold is reached, the LPM is activated and the modules are switched off. The ultracapacitors are loaded again to the upper threshold.

A precondition is the proper value of the input current of the EHS. First, it must be high enough to load the ultracapacitors during the LPM. Second, it must be low enough that the ultracapacitors can be discharged during the high power mode.

5.4.1 Efficiency at Low Capacitor Voltage

This Section shows the result of the efficiency measurement at low voltages of the ultracapacitors. The upper threshold is set to $3\,V$ and the lower threshold to $2.5\,V$. Figure 5.18 shows two charge-discharge cycles of the ultracapacitors.

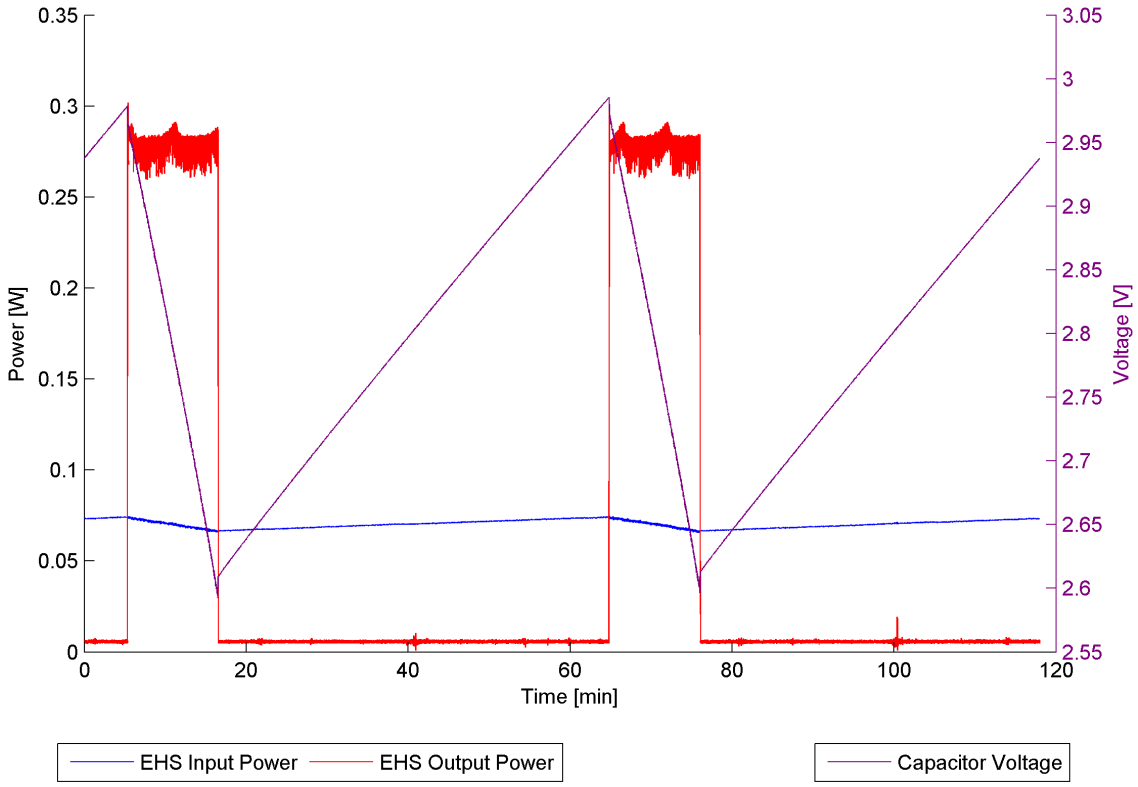

Figure 5.18: Result of the efficiency measurement of the EHS at low capacitor voltages.

The key results of this measurement are listed in Table 5.1.

It can be seen that the true voltage difference of the ultracapacitors (dynamic voltage) is only $0.39\,V$. The reason is the inaccuracy of the voltage measurement of the microcontroller at high mote currents. These high currents cause a higher voltage drop at the shunt resistor for the measurement and the shunt resistor of the EHS.

The input current during the whole measurement was $I_{in} = 22.79\,mA$. The small variation of the input power is caused by the changing voltage of the ultracapacitors. The

Description	Value
Maximum stored energy in the capacitor	$690.76\,J$
Minimum stored energy in the capacitor	$520.91\,J$
Dynamic energy of the capacitor	$169.85\,J$
Maximum capacitor voltage	$2.99\,V$
Minimum capacitor voltage	$2.59\,V$
Dynamic voltage of the capacitor	$0.39\,V$
Duration of a high-power period	$11.21\,min$
Duration of a low-power period	$47.79\,min$
Duty-Cycle	0.23
Average input current	$22.79\,mA$
Average input power	$70.35\,mW$
Average output power	$57.42\,mW$
Total Efficiency of the EHS	$81.62\,\%$

Table 5.1: Key results of the measurement of the EHS efficiency at low voltages of the capacitor.

higher this voltage is the higher is also the input power. The constant input current causes a straight increase of the voltage of the ultracapacitors.

The duty-cycle depends on the average input power, the power consumption of the mote and the efficiency of the EHS. The duty-cycle is 0.23 here.

The resulting efficiency of $\eta_{EHS,low} = 81.62\,\%$ is better than the assumed efficiency. The assumed efficiency consists of the efficiency of input circuit and the efficiency of the output circuit. Both were assumed to be $80\,\%$. The resulting efficiency of the EHS is $\eta_{EHS,assumed} = 64\,\%$. Therefore, the real circuit is much better than expected.

5.4.2 Efficiency at Middle Capacitor Voltage

This Section shows the result of the efficiency measurement at middle voltages of the ultracapacitors. The upper threshold is set to $4\,V$ and the lower threshold to $3.5\,V$. Figure 5.19 shows two charge-discharge cycles of the ultracapacitors.

The key results of this measurement are listed in Table 5.2. It can be seen that the true voltage difference of the ultracapacitors (dynamic voltage) is only $0.40\,V$. The reason is the inaccuracy of the voltage measurement of the microcontroller at high mote currents, too.

The small variation of the input power is caused by the variation of the voltage of the ultracapacitors. The input current is constant at $21.57\,mA$.

The duty-cycle is 0.33 at this measurement. This is higher than the duty-cycle of the previous measurement, because the average input power is higher here. The reason is the higher voltage of the ultracapacitors.

A second consequence of the higher voltage of the ultracapacitors is the higher dynamic

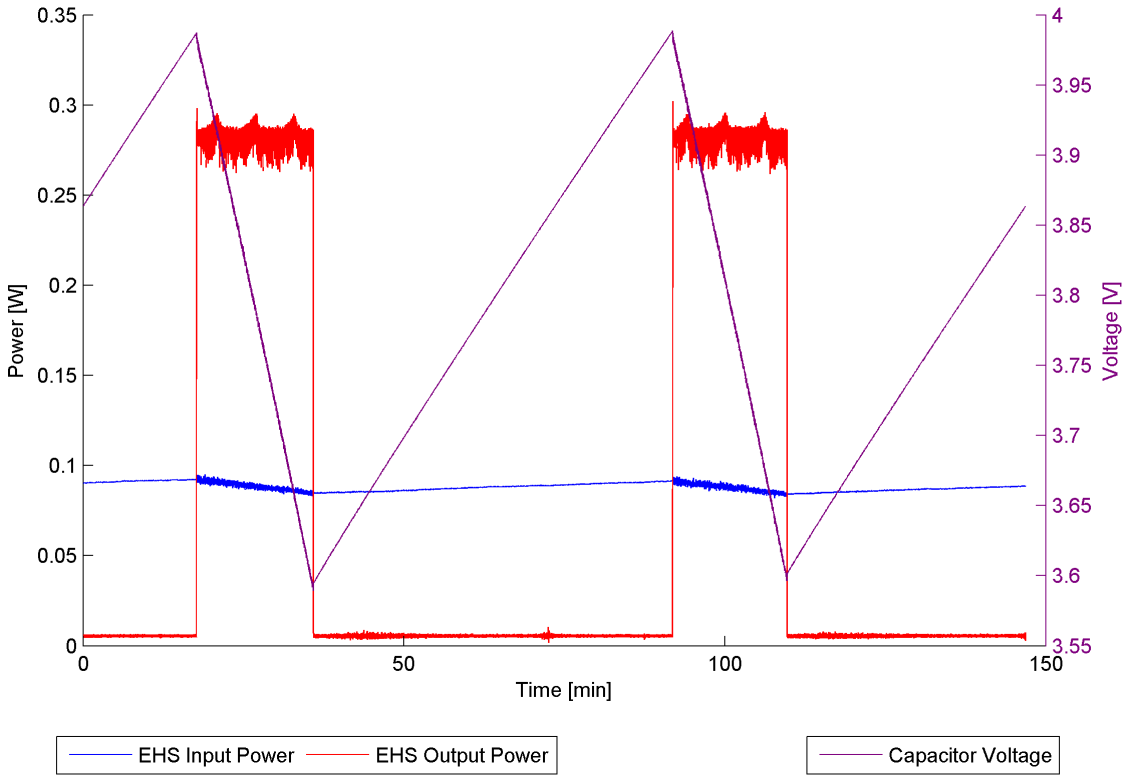

Figure 5.19: Result of the efficiency measurement of the EHS at middle capacitor voltages.

Description	Value
Maximum stored energy in the capacitor	1233.10 J
Minimum stored energy in the capacitor	998.52 J
Dynamic energy of the capacitor	234.57 J
Maximum capacitor voltage	3.99 V
Minimum capacitor voltage	3.59 V
Dynamic voltage of the capacitor	0.40 V
Duration of a high-power period	18.02 min
Duration of a low-power period	55.41 min
Duty-Cycle	0.33
Average input current	21.57 mA
Average input power	88.07 mW
Average output power	73.24 mW
Total Efficiency of the EHS	83.16 %

Table 5.2: Key results of the measurement of the EHS efficiency at middle voltages of the capacitor.

energy. The increase can be calculated with:

$$\frac{234.57J - 169.85J}{169.85J} = 38.1\,\%$$

The resulting efficiency of $\eta_{EHS,middle} = 83.16\,\%$ is better than the assumed efficiency, too. It is even better than the measured efficiency at low voltages of the ultracapacitors. The reason is the lower influence of the Schottky diode. A constant voltage drops at it and therefore it is independent of the input voltage. The higher the input voltage the lower is the influence of this diode.

5.4.3 Efficiency at High Capacitor Voltage

This Section shows the result of the efficiency measurement at high voltages of the ultracapacitors. The upper threshold is set to $4.8\,V$ and the lower threshold to $4.3\,V$. Figure 5.20 shows two charge-discharge cycles of the ultracapacitors.

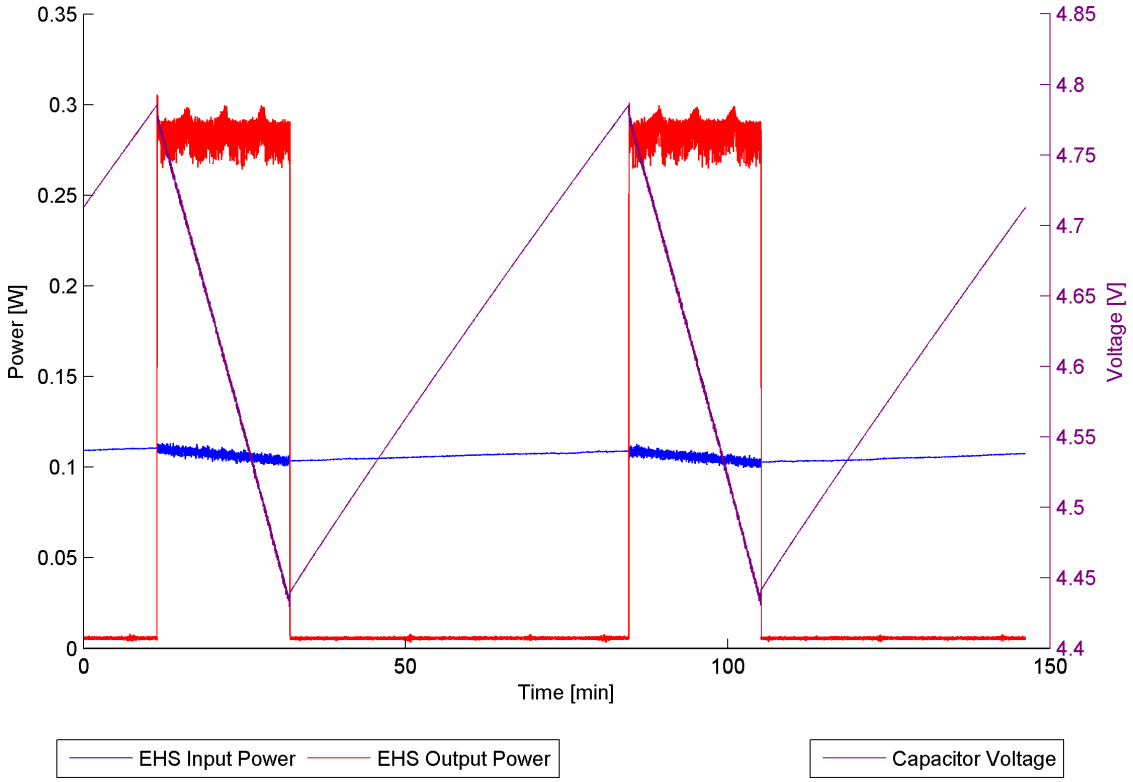

Figure 5.20: Result of the efficiency measurement of the EHS at high capacitor voltages.

The key results of this measurement are listed in Table 5.3.

It can be seen that the true voltage difference of the ultracapacitors (dynamic voltage) is only $0.36\,V$. The reason is the inaccuracy of the voltage measurement of the microcontroller at high mote currents, too.

Description	Value
Maximum stored energy in the capacitor	$1775.01\,Ws$
Minimum stored energy in the capacitor	$1520.90\,Ws$
Dynamic energy of the capacitor	$254.11\,Ws$
Maximum capacitor voltage	$4.79\,V$
Minimum capacitor voltage	$4.43\,V$
Dynamic voltage of the capacitor	$0.36\,V$
Duration of a high-power period	$20.55\,min$
Duration of a low-power period	$52.53\,min$
Duty-Cycle	0.39
Average input current	$21.67\,mA$
Average input power	$106.17\,mW$
Average output power	$84.00\,mW$
Total Efficiency of the EHS 79.11 %	

Table 5.3: Key results of the measurement of the EHS efficiency at high voltages of the capacitor.

The small variation of the input power is caused by the variation of the voltage of the ultracapacitors. The input current is constant at $21.67\,mA$.

The duty-cycle is 0.39 at this measurement. This is higher than the duty-cycle of both previous measurements, because the average input power is higher here. The reason is the higher voltage of the capacitor, too.

The increase of the higher dynamic energy compared to the measurement at low voltages can be calculated with:

$$\frac{254.11J - 169.85J}{169.85J} = 49.1\,\%$$

This is an enhancement compared to the measurement at middle voltages, although the dynamic voltage is lower.

The resulting efficiency of $\eta_{EHS,high} = 79.11\,\%$ is better than the assumed efficiency, too. The measurement at middle voltages shows an enhancement of the efficiency. This is what has been expected here. The reason of the low decrease could be the leakage current of the ultracapacitors. The higher the voltage of the ultracapacitors the higher is the leakage current.

Since the energy storage system should harvest as much energy as possible, the ultracapacitors should be fully charged if possible. Furthermore, the energy reserves are higher at fully charged ultracapacitors.

5.5 Solar Cell Characterization

The results of the characterization of the solar cell are presented in this Section. Figure 5.21 shows the measurement setup. The adjustable resistor R_{var} is used to set a specific current of the solar cell. The results are shown in Figure 5.22. The solar cell was placed

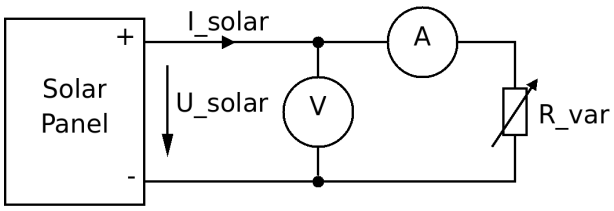

Figure 5.21: Measurement setup of the solar cell characterization.

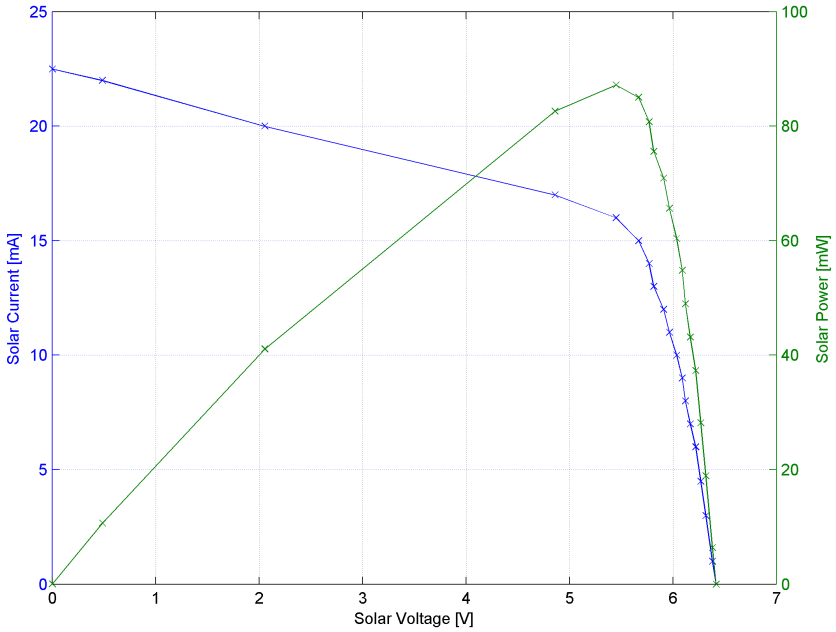

Figure 5.22: Characterization of the solar cell.

5 cm under a standard lighting bulb with 75 W. It equates to very dark lighting conditions, for example on a cloudy day in December. The power is calculated with:

$$P_{solar} = U_{solar} \cdot I_{solar}$$

It can be seen that the maximum power point is at a solar voltage of 5.5V. This is the maximum power point of the solar cell at dark lighting conditions. Therefore, it is suitable very well for the introduced EHS.

The maximum power can be harvested if the ultracapacitors are fully charged.

5.6 Solar Charging Measurement

This Section shows the results of the solar charging measurement. The solar cell was placed 5 cm under a standard lighting bulb with 75 W. The initial voltage of the ultracapacitors was 0 V. The measurement setup is similar to the setup of the efficiency measurement and

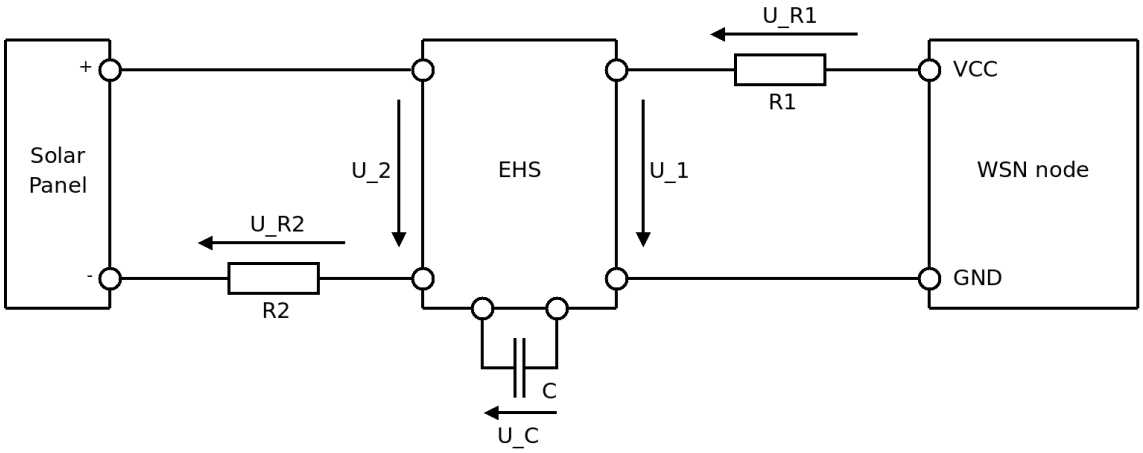

Figure 5.23: Setup of the solar charging measurement.

is shown in Figure 5.23. The only difference is that the constant current source is replaced by the solar cell. A detailed explanation of measurement setup and of the calculations can be found in Section 5.4.

Figure 5.24 shows the full charging process. It can be seen that the voltage of the ultracapacitors rises evenly until the voltage conditioning unit starts working. Then the mote starts its normal operation and the output power of the EHS is unequal to zero. This leads to a slower rising of the voltage. The high peak of the output power is caused by the GPS unit of the mote. It is activated during initialization of the microcontroller for a very short time.

The drops of the input power are caused by changes of the lighting conditions of the solar cell. They are not caused by the charging process or the supply of the mote.

The key results are shown in Table 5.4. The energy efficiency η_{energy} is calculated with:

Description	Value
EHS total input energy	$3069.07\,J$
EHS total output energy	$329.26\,J$
Maximum stored energy in the capacitor	$1917.74\,J$
Energy efficiency	73.2%
Maximum capacitor voltage	$4.97\,V$
Minimum capacitor voltage	$0.02\,V$
Duration of charging	$953.8\,min$
Average input current	$17.38\,mA$
Average input power during whole measurement	$53.63\,mW$
Average output power during whole measurement	$5.75\,mW$

Table 5.4: Key results of the measurement of the solar charging process.

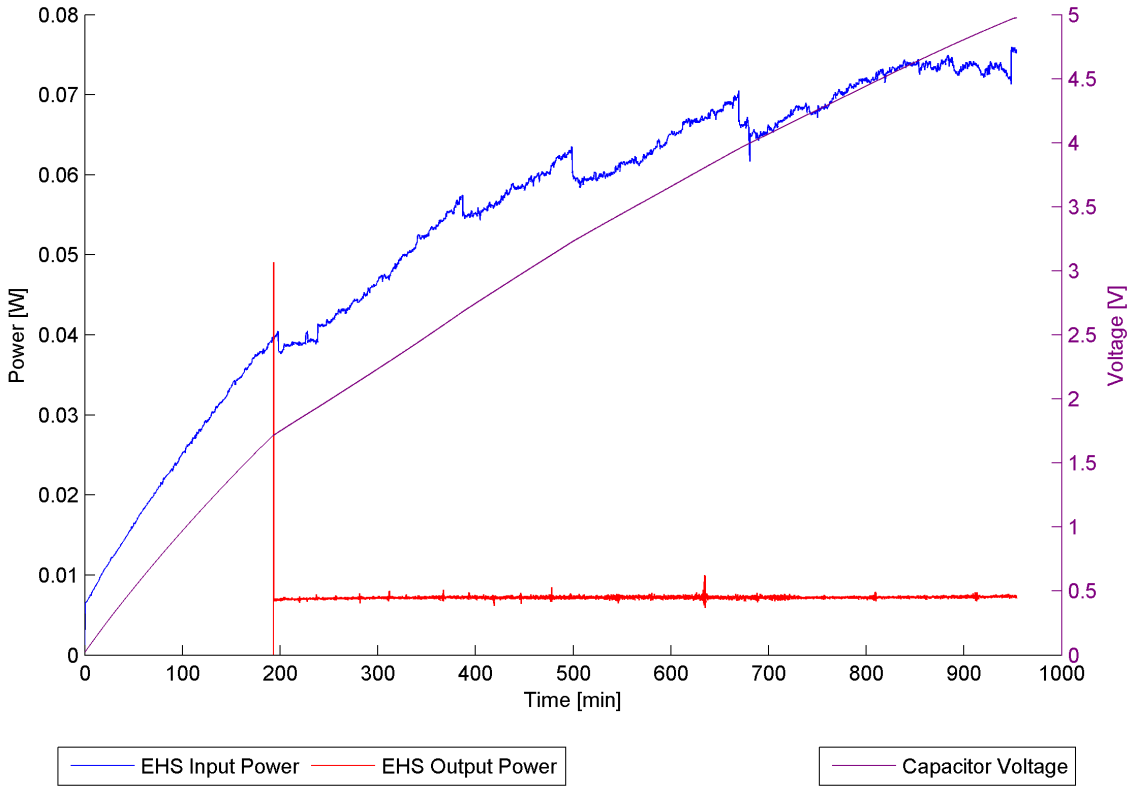

Figure 5.24: Full charging process of the ultracapacitor by the solar cell.

$$\eta_{energy} = \frac{E_{stored,max} + E_{output}}{E_{input}} = 73.2\,\%$$

This means that 28.6 % of the input energy are lost in the circuits and in the charging process of the ultracapacitors.

The charging time is higher than the daytime in December. It is $15.9\,h$. The reason is that the solar cell is not designed to charge both ultracapacitors during one day. It is only designed to compensate the consumed energy of the night during daytime at bad weather conditions.

The measurement data was used to characterize the solar cell a second time. Figure 5.25 shows the result. It can be seen that it is very similar to the results shown in Section 5.5.

Finally, Figure 5.26 shows the solar efficiency during the charging process. The solar efficiency was calculated by assuming the maximum power point of the input power as 100 %:

$$\eta_{solar} = \frac{P_{solar}}{max(P_{solar})} \cdot 100\%$$

It can be seen that the solar efficiency is better than 80 % if the voltage of the ultracapacitors is higher than $3\,V$. In this case, the solar voltage is about $U_{solar} = 3.4$, because

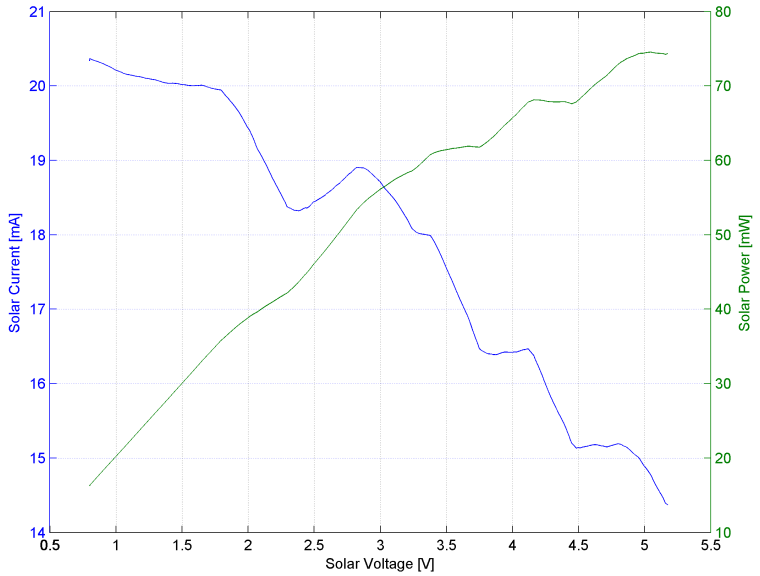

Figure 5.25: Characterization of the solar cell during the charging process.

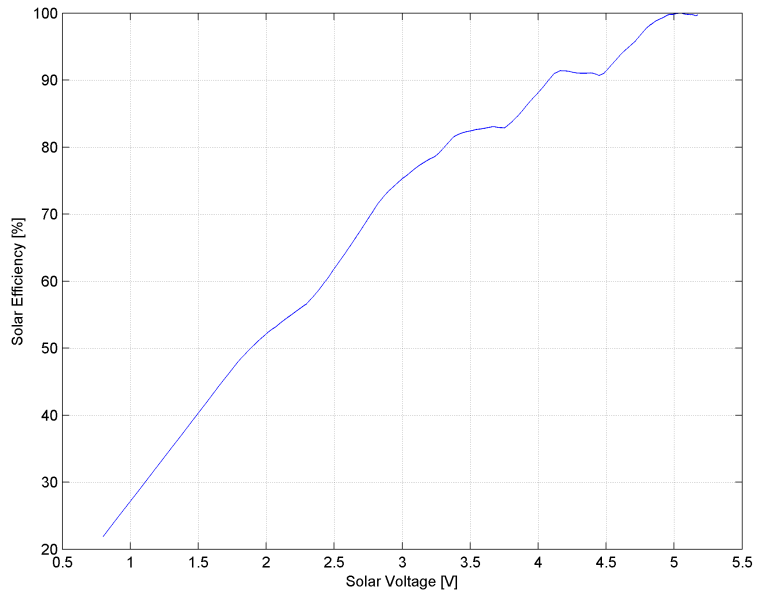

Figure 5.26: Solar efficiency during the charging process.

of the forward voltage of the Schottky diode. Therefore, the voltage of the ultracapacitors should be kept as high as possible.

This result can also be applied to the overall energy harvesting efficiency. The resulting total efficiency can be calculated with:

$$\eta_{EHS,tot} = \eta_{solar} \cdot \eta_{EHS,middle} = 0.8 \cdot 0.832 = 66.56\,\%$$

It is slightly above the assumed efficiency $\eta_{EHS,assumed} = 64\,\%$. Therefore, it is possible to harvest enough energy to supply the RiverMote during day and night.

5.7 Ultrasonic Measurements

This Section presents the results of the measurements of the ultrasonic unit. The measurements were done with two motes. The first one was used as transmitter and the second one as receiver. This reduces the disturbances to a minimum.

The test environment consists of a basin ($42\,cm$ length and $27\,cm$ width) filled with clear water ($12\,cm$). The transceivers of both motes were fixed in a floating cellular plastic, heading into the water. The distance of both transceivers is $8.5\,cm$. One of the transceivers is connected to the transmitting mote and the other one to the receiving mote. The floating cellular plastic was placed in the middle of the basin.

The measurements were done with the oscilloscope unit DSO-2090 from Voltcraft®. Figure 5.27 shows the output signal, which is used to generate ultrasonic waves. Five cycles have been generated. The resulting peak-to-peak voltage at the transceiver is about

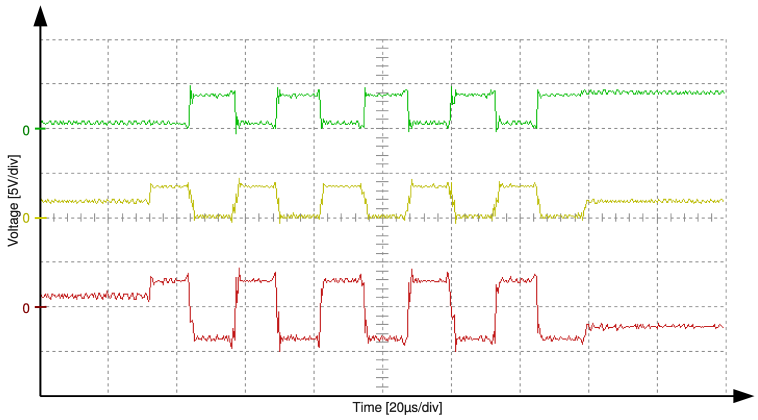

Figure 5.27: Output signal of the ultrasonic unit without a transceiver. It shows the functionality of the generation of the ultrasonic signal. The green trace is the voltage of the first output pin and the yellow trace of the second output pin. The red trace represents the differential signal.

$Upp = 6.2\,V$ and the frequency is $f = 40\,kHz$.

The propagation speed in water at $20\,°C$ is $v = 1482\,m/s$ [8]. The expected latency between transmitting and receiving depends on the propagation speed v and the distance d. The distance can be calculated with:

$$d = \sqrt{\left(\frac{sensordistance}{2}\right)^2 + (waterdepth)^2} \cdot 2 = \sqrt{\left(\frac{8.5cm}{2}\right)^2 + (12cm)^2} \cdot 2 = 25.46\,cm$$

The latency can be calculated with:

$$t_{latency,12cm} = \frac{d}{v} = \frac{0.2546m}{1482m/s} = 171.8\,\mu s$$

Figure 5.28 shows the output signal with a connected transceiver. Only 2 cycles have been generated.

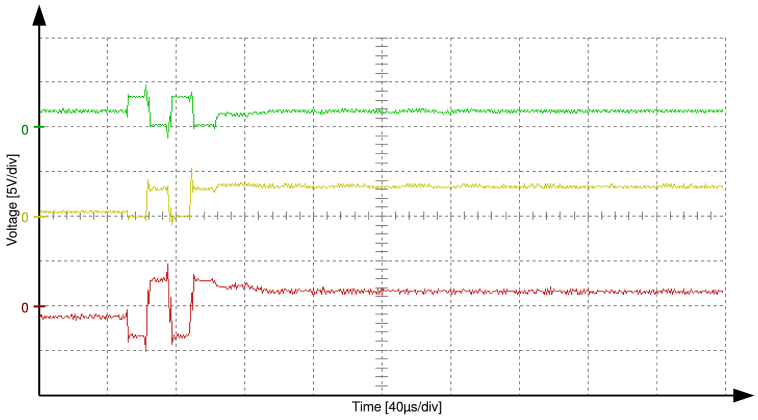

Figure 5.28: Output signal of the ultrasonic unit. The transceiver was connected and placed in the water. The green trace is the voltage of the first output pin and the yellow trace of the second output pin. The red trace represents the differential signal.

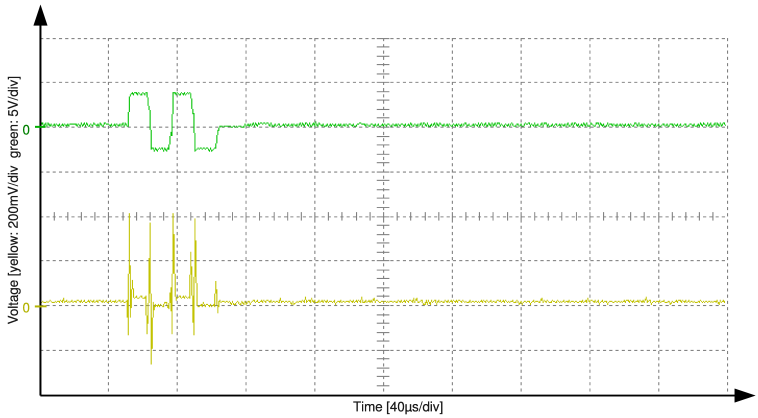

Figure 5.29: Received signal of the second ultrasonic transceiver. The green trace is the generated output signal of the first transceiver and the yellow trace is the received signal of the second transceiver.

The reason is the very low water level in the test environment. In this case, the resulting time of transmission is:

$$t_{transmission} = 2 \cdot \frac{1}{f} = 2 \cdot \frac{1}{40kHz} = 50\,\mu s$$

The time difference of the end of the transmission and the expected start of receiving is $171,8\mu s - 50\mu s = 121,8\mu s$. This is enough time to be able to measure the distance.

Figure 5.29 shows the received signals of the second ultrasonic transceiver. The high peaks of the yellow trace are electromagnetic disturbances, because they are synchronous to the switching operation of the transmitting mote. They are caused by the unshielded connection cables of the ultrasonic transceivers. Therefore, the ultrasonic transceivers should be equipped with shielded connection cables.

Figure 5.30 shows the output of the amplifier at the receiving mote. It can be seen that the electromagnetic disturbances generate high peaks initially.

Figure 5.31 shows the amplified signal of the second ultrasonic transceiver without placing the transceivers into the water.

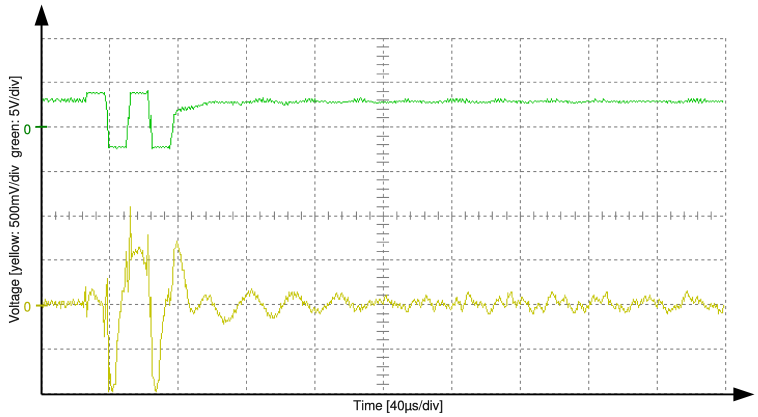

Figure 5.30: Amplified signal of the second ultrasonic transceiver. Both transceivers are placed in the water. The green trace is the generated output signal of the first transceiver and the yellow trace is the amplified signal of the second transceiver.

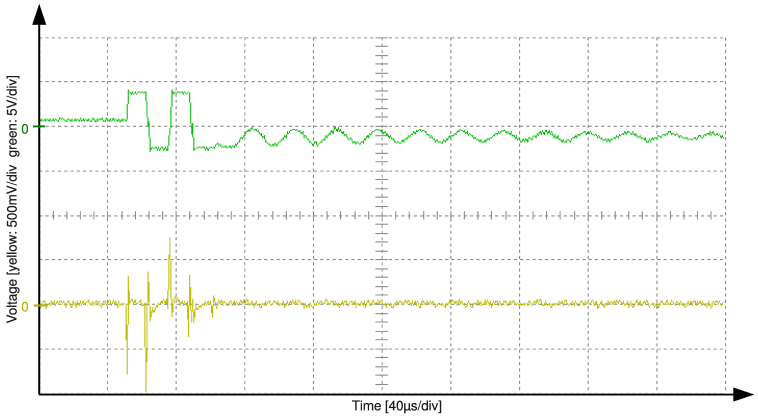

Figure 5.31: Amplified signal of the second ultrasonic transceiver. Both transceivers are placed out of the water. The green trace is the generated output signal of the first transceiver and the yellow trace is the amplified signal of the second transceiver.

It can be seen that there is a big difference between 5.30 and 5.31. There is no signal if the transceivers are placed out of the water. This shows that the transceivers are conceived only for the application in water.

The amplified and rectified signal is shown in Figure 5.32. The influence of the electro-

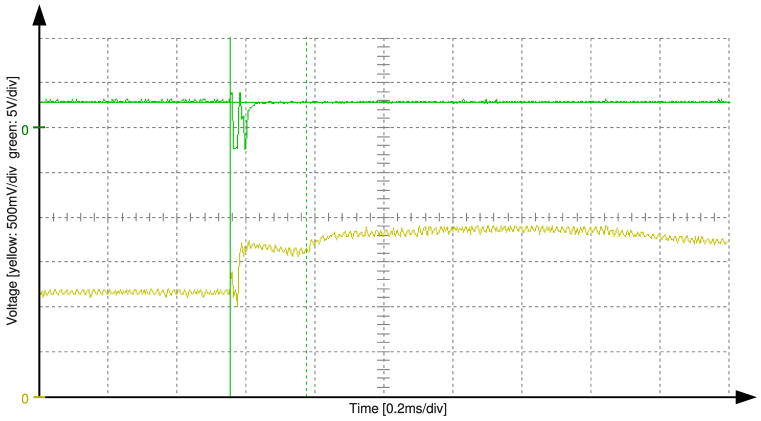

Figure 5.32: Amplified and rectified signal of the second ultrasonic transceiver. The green trace is the generated output signal of the first transceiver and the yellow trace is the amplified and rectified signal of the second transceiver.

magnetic disturbances can be seen clearly. The result is a high immediate increase of the output voltage. This can be filtered by software. The software starts the sampling process of the received signal after the sending process is completed. Then, it waits only for the next increase. This increase represents the reflected sound waves.

The measured latency is $t_{latency,meas} = 222\,\mu s$. This is higher than the calculated one ($171.8\,\mu s$). The reason could be the response time of the transceivers. The difference here is $222\mu s - 171.8\mu s = 50.2\,\mu s$.

Figure 5.33 shows the amplified and rectified signal at a lower water level of $7.5\,cm$. It can be seen that the measured latency time is reduced to $170\,\mu s$. The expected latency time is:

$$t_{latency,7.5cm} = \frac{\sqrt{\left(\frac{8.5cm}{2}\right)^2 + (7.5cm)^2} \cdot 2}{v} = \frac{0.1724m}{1482m/s} = 116.3\,\mu s$$

The difference to the measure latency time is $170\mu s - 116.3\mu s = 53.7\,\mu s$.

Finally, the measurements have been done at a very low water level of $3\,cm$. The results are shown in Figure 5.34. It can be seen that the measured latency time is reduced to $106\,\mu s$. The expected latency time is:

$$t_{latency,3cm} = \frac{\sqrt{\left(\frac{8.5cm}{2}\right)^2 + (3cm)^2} \cdot 2}{v} = \frac{0.104m}{1482m/s} = 70.2\,\mu s$$

The difference to the measure latency time is $106\mu s - 70.2\mu s = 35.8\,\mu s$.

Therefore, the difference of the measured and the expected latency depends on the water level. The correction algorithm can be implemented in software.

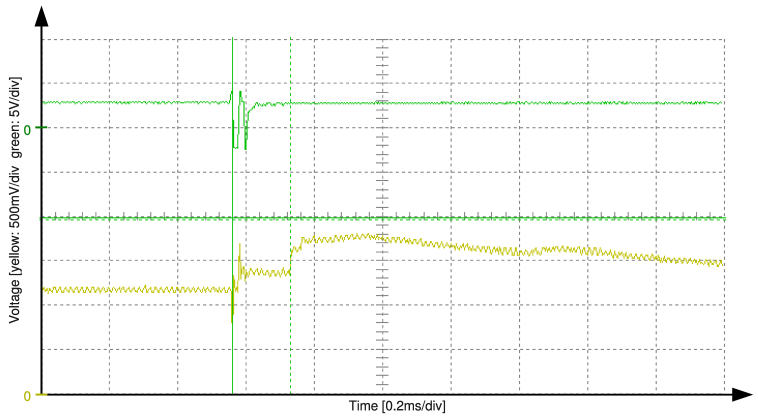

Figure 5.33: Amplified and rectified signal of the second ultrasonic transceiver at a water level of 7.5 *cm*. The green trace is the generated output signal of the first transceiver and the yellow trace is the amplified and rectified signal of the second transceiver.

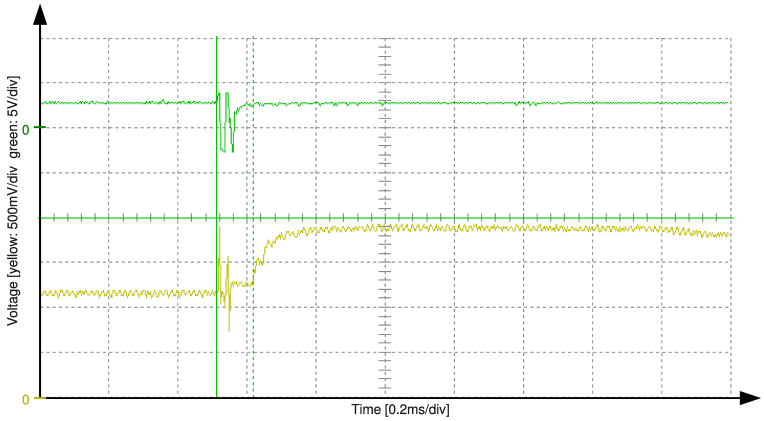

Figure 5.34: Amplified and rectified signal of the second ultrasonic transceiver at a water level of 3 *cm*. The green trace is the generated output signal of the first transceiver and the yellow trace is the amplified and rectified signal of the second transceiver.

A second test environment with a larger basin was used to be able to measure distances of up to 80 *cm*. A measurement application has been written which samples continuously the analog input signal of the rectified amplifier output. The reflected ultrasonic signal causes an increase of the rectified signal. The number of the sample with a significant increase is returned as measurement value. Figure 5.35 shows the result of the measurement with this software. It can be seen that the accuracy of the measurement is between 10 *cm* and 20 *cm*. It can be enhanced by using more powerful ultrasonic waves and more sensitive amplifiers.

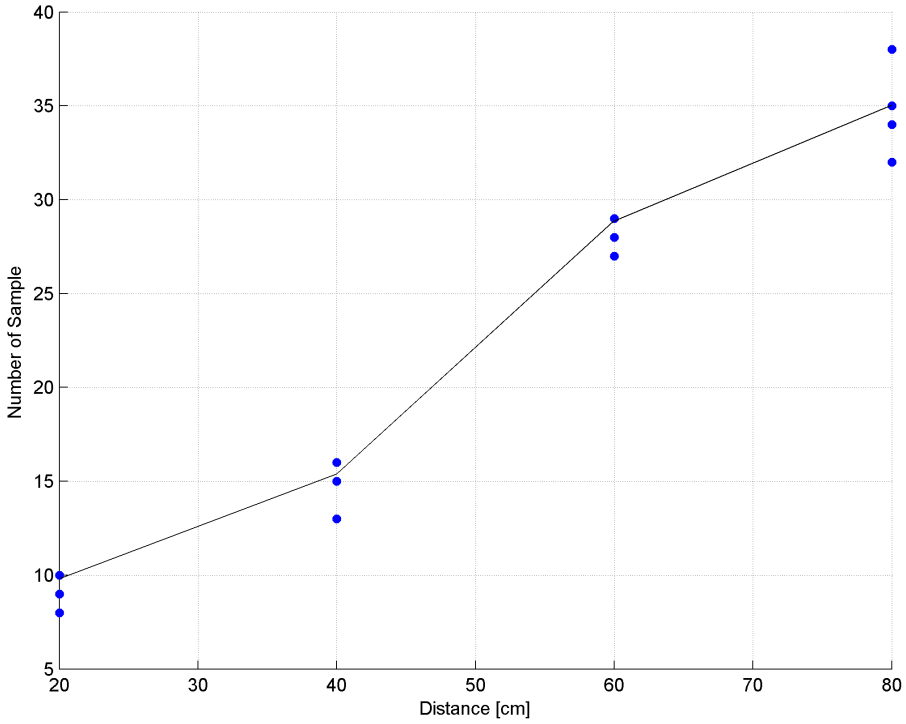

Figure 5.35: Ultrasonic distance measurement using only one mote as transmitter and receiver. The distance between both ultrasonic transceivers has been modified in four steps. About 20 measurements have been done at each distance.

5.8 GPS Measurements

The results of the GPS measurement can be found in this Section. The measurement setup only consists of two RiverMotes with a GPS receiver (mote 2 and mote 3). The third RiverMote was used as base station (mote 1). It was connected to a PC, which records the measured data. Mote 2 and mote 3 activate the GPS module at startup and perform a factory reset of the module. Therefore, both modules start working with the same initial data. The GPS modules perform a position fix every second. This data is processed by the motes and sent to the base station. Mote 2 and mote 3 are placed with a distance of approx. one meter between of them. Both were placed at the same height outside without any obstacles between them and the sky.

Figure 5.36 shows the altitude measurement of both RiverMotes. It can be seen that the variation of the altitude over the time is very high (more than 100 meters). In addition, the variation of the first node is uncorrelated to the variation of the second node. Therefore, the real height difference cannot be calculated out of this data. The data was sent from the GPS module via the NMEA protocol standard. This GPS module does not support a raw data format. Therefore, it cannot be used to determine the river level. GPS modules of a different manufacturer could also be more accurate. However, this would go beyond the scope of this master's thesis.

A positive result of this measurement is, that both nodes were only supplied by the

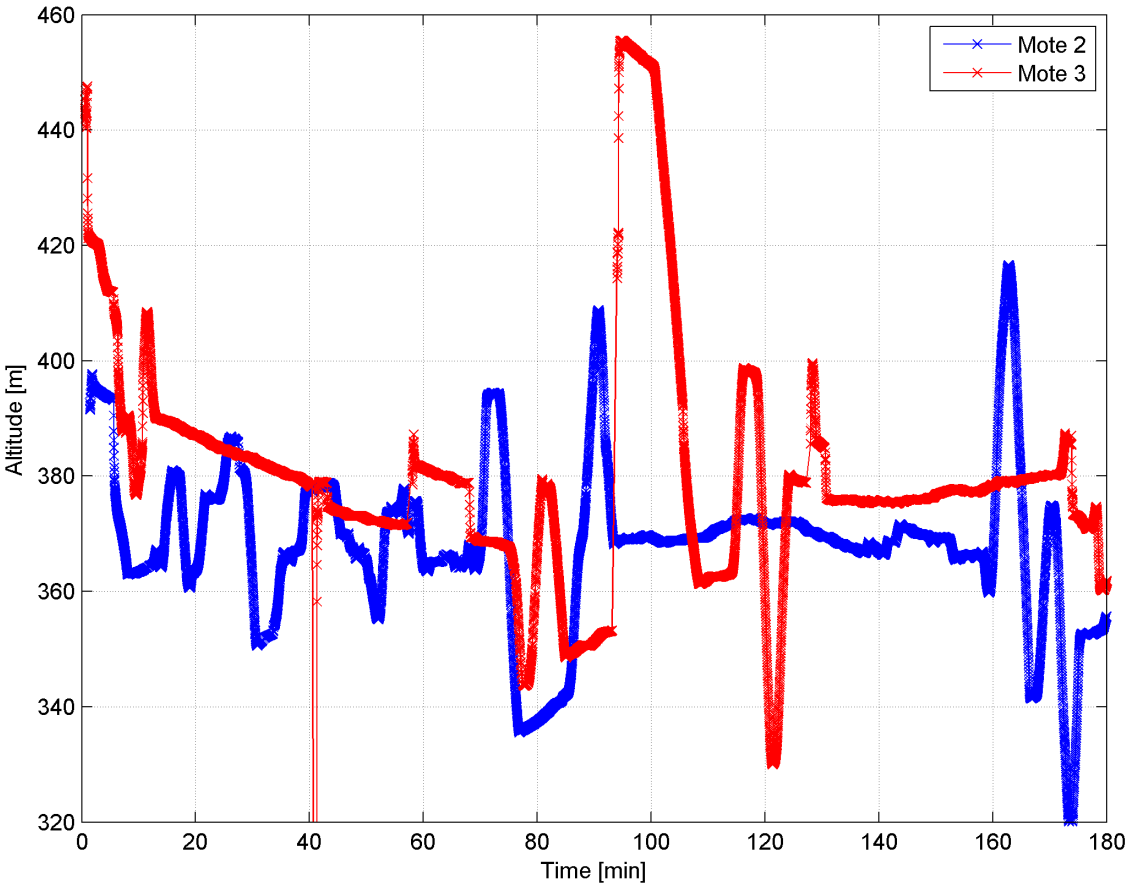

Figure 5.36: Altitude of the GPS measurement with two RiverMotes.

EHS. The ultracapacitors kept fully charged at both nodes. It was a sunny day and both nodes harvested enough energy to keep the GPS module activated during the whole measurement. Therefore, it is possible to keep the GPS module activated during the whole daytime if it is a sunny day.

A second GPS measurement has been taken at Schwarzlsee near Graz. Figure 5.37 shows the result of this measurement. Mote 2 was placed during the whole measurement at a fix position and height. Mote 3 has been placed half a meter higher than mote 2 initially. Mote 3 has been moved down to the lake after 7 minutes. This can be seen clearly in the plot. The rapid change of the measured height of both RiverMotes after 8.5 min was the first time that both nodes have changed in the same way. Mote 3 has been returned to its initial position after 9.5 minutes. The difference of both motes after the movement to the lake and back isn't the same difference as it was at the beginning of the measurement. Therefore, the standard GPS measurement cannot be used to determine the height difference as mentioned above.

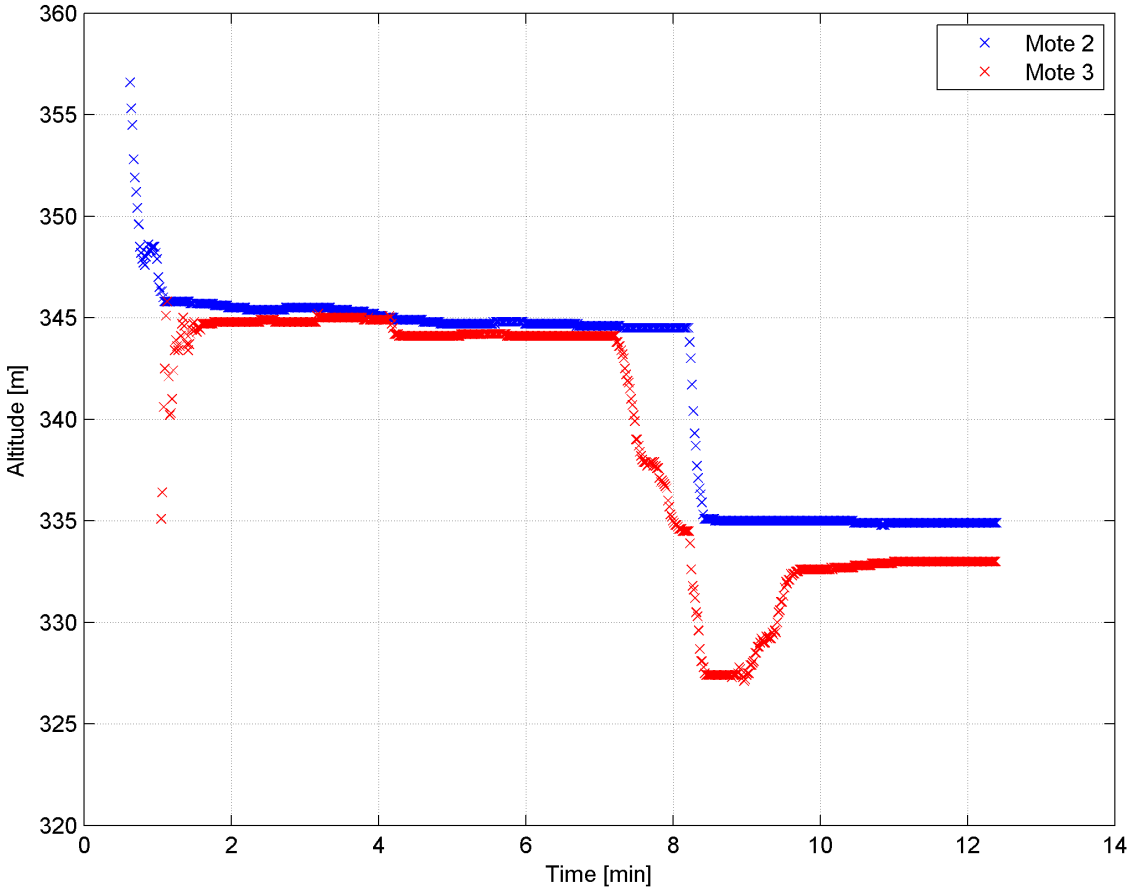

Figure 5.37: Altitude of the GPS measurement with two RiverMotes.

5.9 Long-Term Measurements

This Section presents the results of the long-term measurement. The long-term measurement setup is very similar to the setup of the GPS measurements. Mote 2 and mote 3 are placed on the south balcony of Institute for Technical Informatics. The balcony is roofed, but is opened to the south. Therefore, the solar cells are exposed to the sunlight during daytime. Both nodes are programmed to send the gathered data to the base station (mote 1) after a given interval.

Mote 2 is configured to send the data only every 10 min. It is also configured to activate the GPS module for ten position fixes. Mote 2 is placed under a clear-transparent cover. Since the balcony is roofed, the GPS module does not get a valid signal.

Mote 3 is configured to send the data every 50 s. The higher activation interval causes higher power consumption. Therefore, it does not activate the GPS module. It is only used to measure the energy state and the temperature. Mote 3 is mounted in a housing with a grayish-transparent cover.

Figure 5.38 shows the measured voltages of mote 2 and Figure 5.39 of mote 3. It can be seen that the long-term measurements last for five days. The RiverMotes operate con-

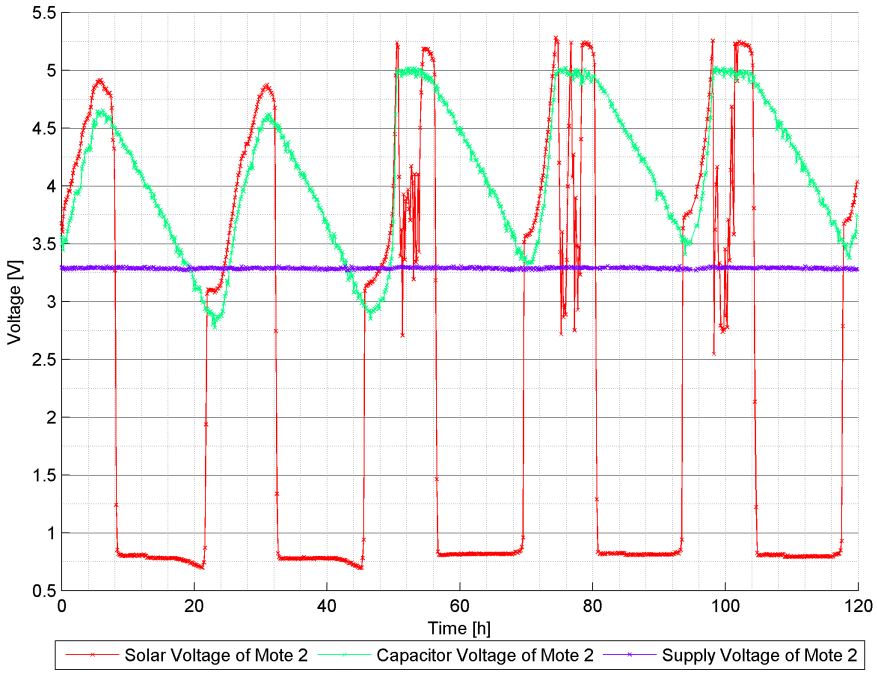

Figure 5.38: Measured voltages of mote 2 during the long-term test.

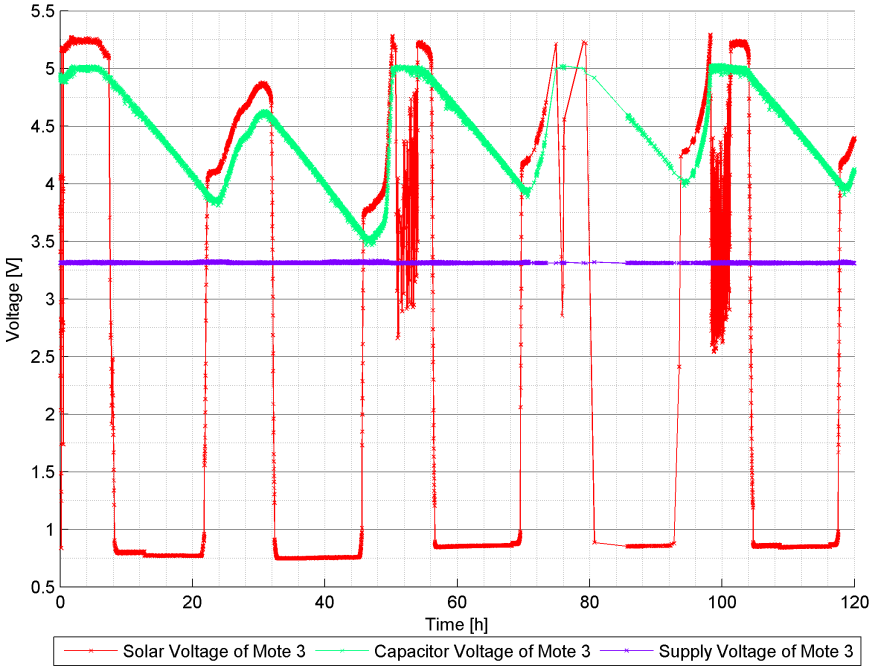

Figure 5.39: Measured voltages of mote 3 during the long-term test.

tinuously without a manual recharging of the ultracapacitors during these days. Initially, mote 3 was fully charged ($5\,V$) and mote 2 was charged to a voltage of $3.5\,V$. The first two days were cloudy and the nodes could not harvest much energy. Mote 3 could not harvest enough energy to stay in an energy neutral operation mode during the first two days. The reason is that this mote was placed under a grayish-transparent cover. It reduces the harvestable energy severely. Mote 2 was placed under a clear-transparent cover and so it could stay in an energy-neutral operation mode. Besides, both RiverMotes were placed at a roofed balcony, as mentioned before. It is very important to have as much open-air as possible during days with bad weather conditions. Therefore, the harvestable energy is higher than the measured one.

The output voltage of the EHS of both RiverMotes is constant during the measurement period. The temperature in the housing varies strongly as it can be seen later in Figure 5.43. Therefore, it is independent of the voltage of the ultracapacitors and of the temperature.

The fall-off of the solar voltage at fully charged ultracapacitors is caused by the overcharge protection circuit. The simulation of the overcharge protection did not show such a behavior. However, it is not disturbing, because the ultracapacitors are kept fully charged during the rest of daytime.

Figure 5.40 shows the current of mote 2 during the long-term measurement and Figure 5.41 shows the current of mote 3. Both plots show the bad weather condition at the first

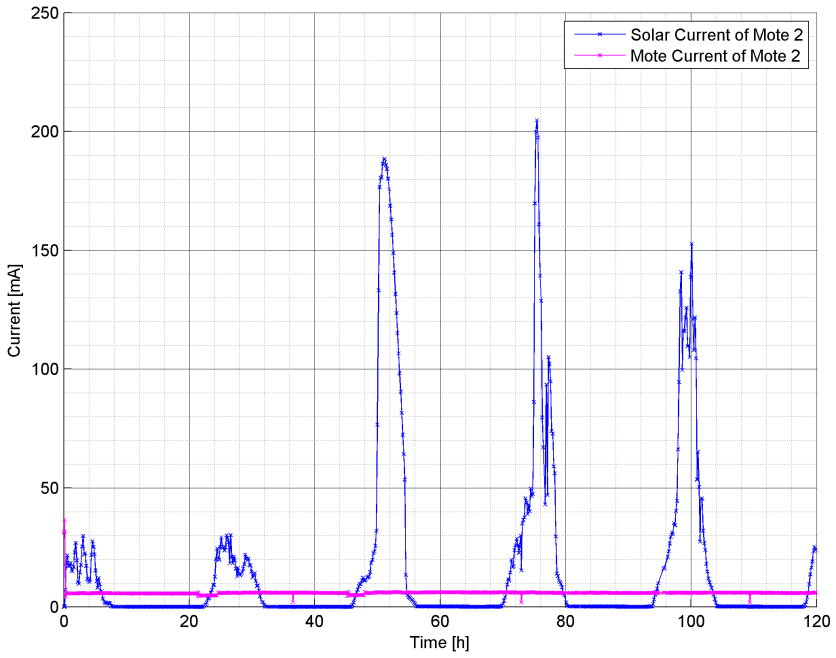

Figure 5.40: Measured currents of mote 2 during the long-term test.

two days. The third day was very sunny. This results in a high solar current during this day.

The comparison of both plots shows the effect of different housings. It can be seen that

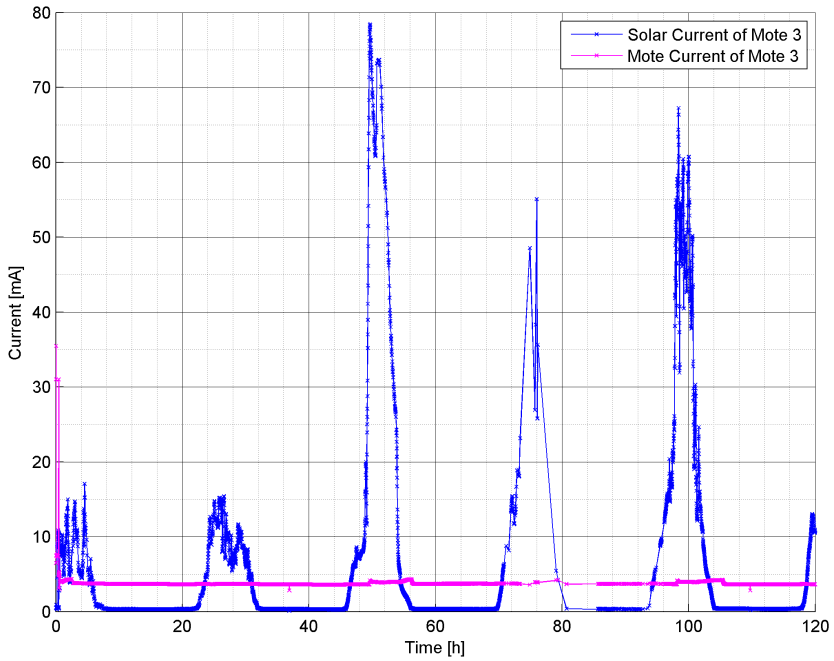

Figure 5.41: Measured currents of mote 3 during the long-term test.

the solar cell of mote 3 only drives about half the current than the solar cell of mote 2. Both cells are aligned horizontally. Figure 5.42 shows the average currents of each day. The difference between the solar current of mote 2 and of mote 3 is lower at bad lighting

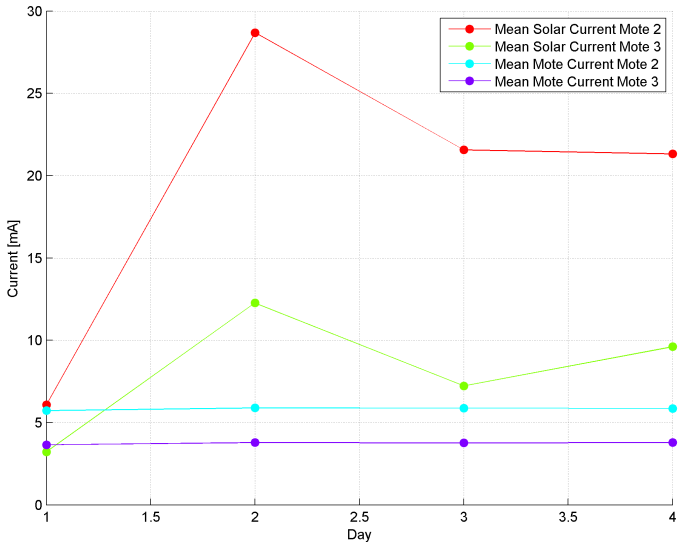

Figure 5.42: Average currents of each day. The first day was left out, because of incompleteness.

conditions. Generally, a clear-transparent covering of the solar cell should be used.

The average output currents of the EHSs of each RiverMote are nearly constant during the whole measurement (Figure 5.40, 5.41 and 5.42). It is also independent from the temperature. The temperature trend during the whole measurement is shown in Figure 5.43. The Figure shows the uncorrected temperatures measured by both RiverMotes.

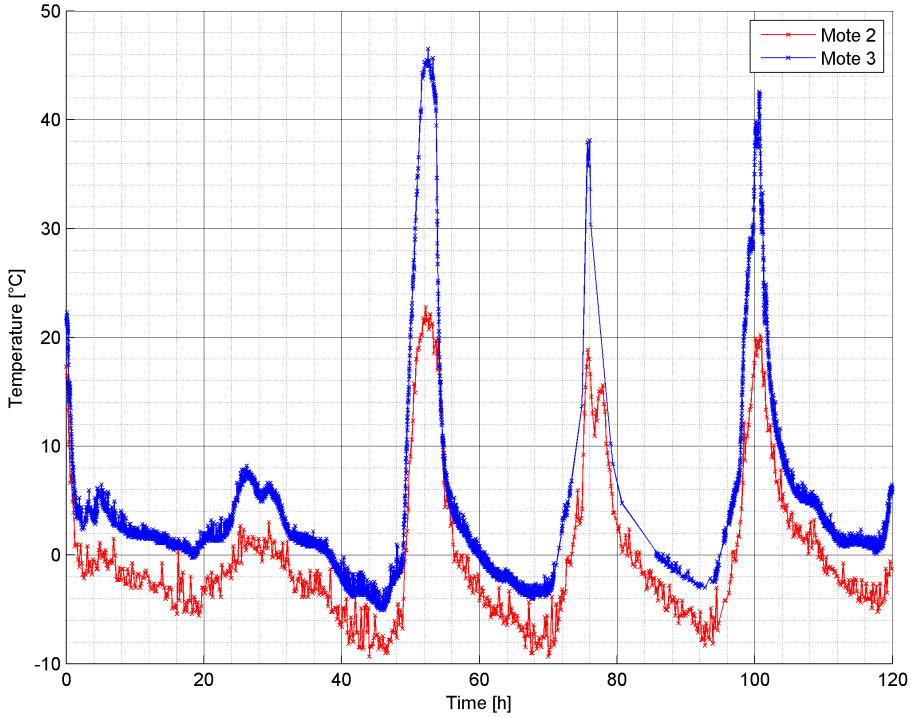

Figure 5.43: Temperature traces of both RiverMotes during the long-term test. The measurement data have not been corrected. The offset error is $\pm 20\,°C$ as specified in [45].

The measurements have an offset error of $\pm 20\,°C$ as specified in the data sheet [45]. The measurements show the need for correcting the temperature values. A single point calibration is sufficient as described in the data sheet.

It can be seen that the temperature in the grayish housing (mote 3) increases much more. The highest temperature was reached on third day of the long-term test and was $46\,°C$. The outside temperature was about $10\,°C$ on this day. Much higher values are expected in summer. The absolute maximum temperature of $80\,°C$ should not be exceeded. Therefore, the design of the housing of the RiverMotes must ensure that the inside temperature does not exceed the maximum temperature.

The measurement of the air temperature cannot be done with the sensor inside the housing on sunny days. A special sensor outside of the housing is necessary if the air temperature should be measured.

Figure 5.44 and 5.45 show the calculated input power and output power of mote 2 and mote 3.

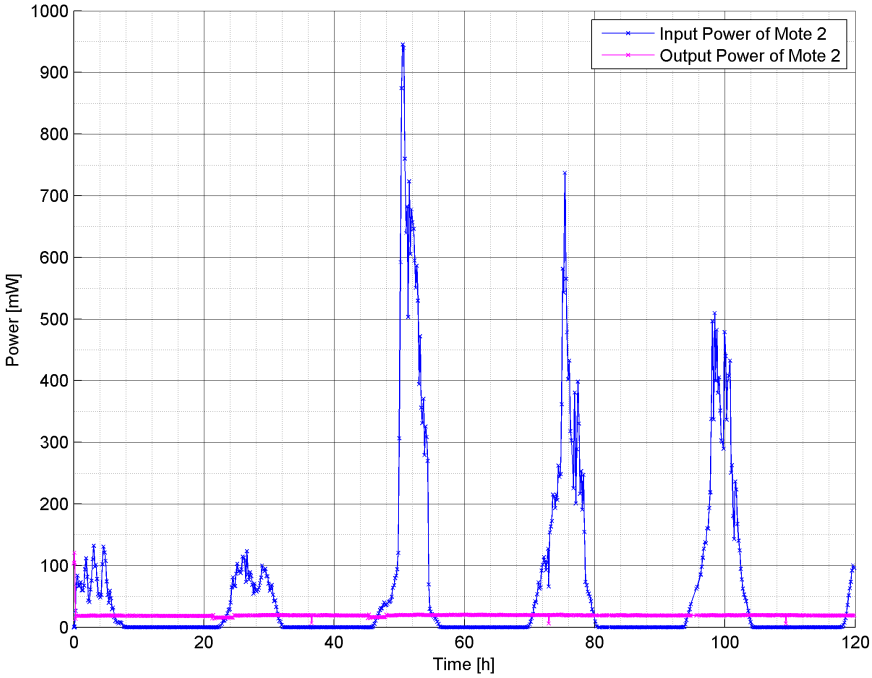

Figure 5.44: Input and output power of the EHS of mote 2 during the long-term test.

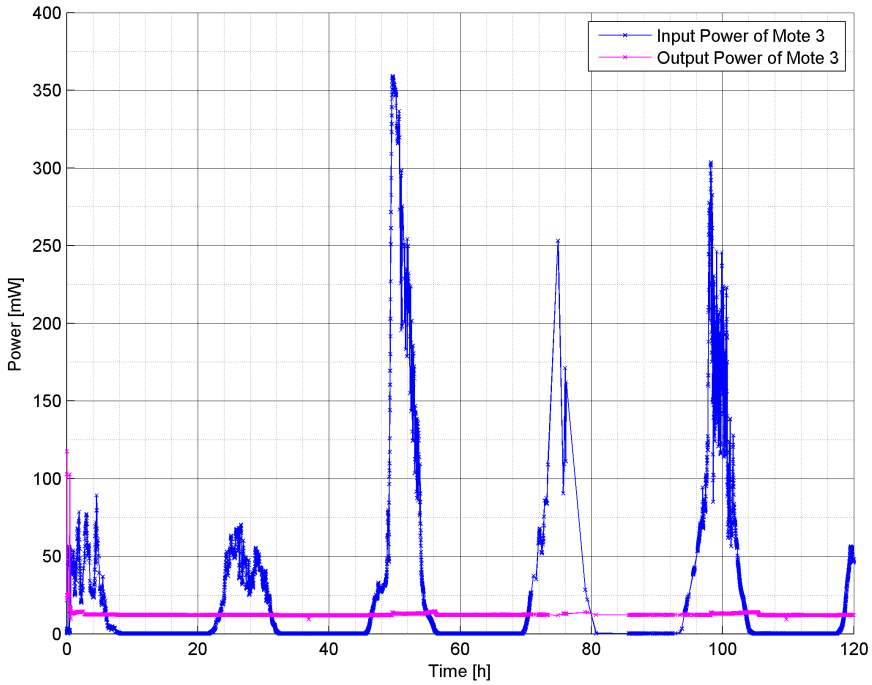

Figure 5.45: Input and output power of the EHS of mote 3 during the long-term test.

The traces of the input and output power are similar to the traces of the solar and mote current. The average input and output power of each day are shown in Figure 5.46.

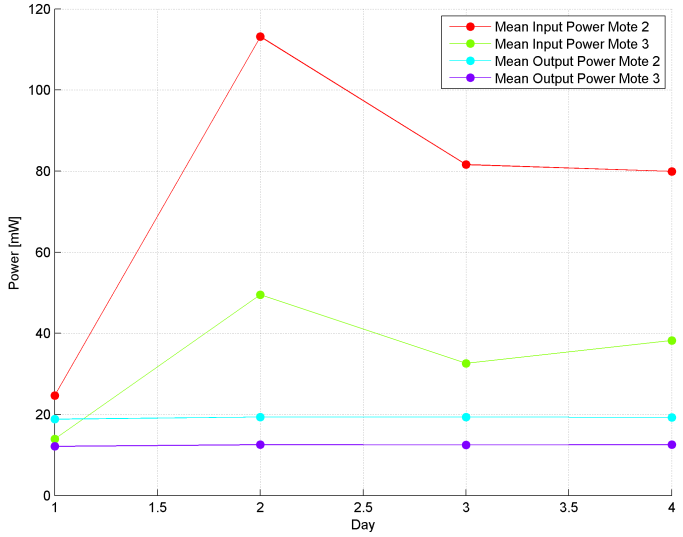

Figure 5.46: Average input and output power of each day. The first day was left out, because of incompleteness.

The solar cell must harvest an energy of $E_{24h,solar} = 1863\,J$ each day as described in Section 3.3.3. The average power during the whole day can be calculated with:

$$P_{24h,solar,avg} = \frac{E_{24h,solar}}{24h} = \frac{1863J}{24h} = 21.56\,mW$$

It can be seen that the input power on the second day (first values in Figure 5.46) of mote 3 is lower than the calculated value. Therefore, the voltage of the ultracapacitors decreases. The input power of mote 2 is a little bit higher than the calculated one. The voltage of the ultracapacitors keeps constant. Therefore, the size of the solar cell is sufficient to supply the RiverMote.

5.10 Range Measurements

The results of the range measurements can be found here. The measurements are taken on the area of Schwarzlsee near Graz. The receiver is placed on the dashboard of a car. The sender is moved to a given distance. A packet is sent to the receiver about every second. The packet consists of the standard measurements (voltage, current, without GPS) including a sequence number. The sequence number and the arrival time of the packet are used to detect lost packets. The receiver is configured to receive only packets with correct checksum.

Figure 5.47 shows the results of the first range test. The sender is placed $442\,m$ off the receiver in line-of-sight. The receiver measures the received signal strength indicator (RSSI) value of the received packets. These values are plotted over time. Only one packet

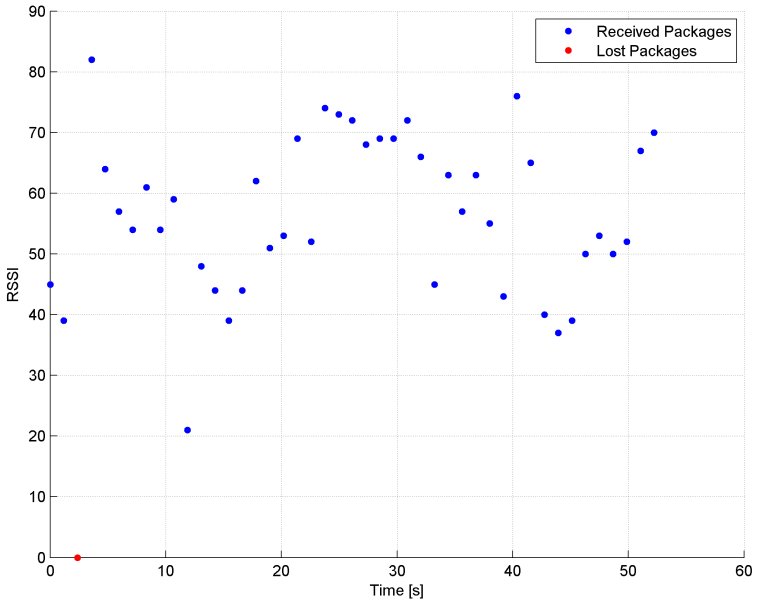

Figure 5.47: RSSI value of the received packets. The sender is placed 442 m off the receiver.

is lost during the measurement (52 s). The packet loss rate is:

$$lossrate = 1 - \frac{receivedpackets}{sentpackets} = 1 - \frac{44}{45} = 2.2\,\%$$

The received signal power can be determined with the RSSI value. The dependency of the RSSI value and the received signal power is shown in Figure 5.48.

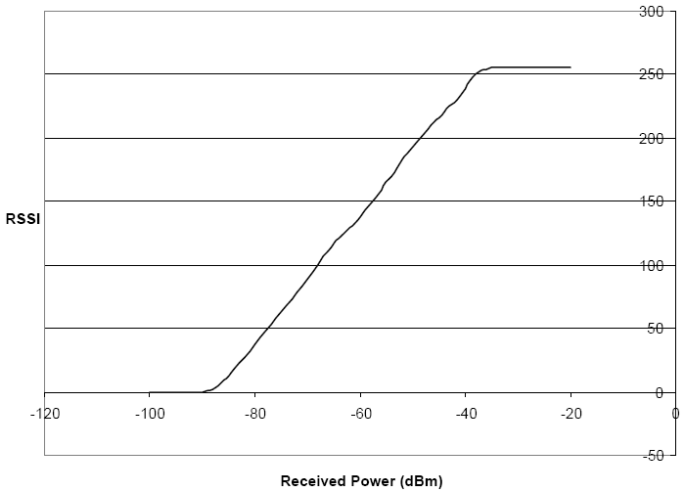

Figure 5.48: Dependency of the RSSI value and the received signal power from [27].

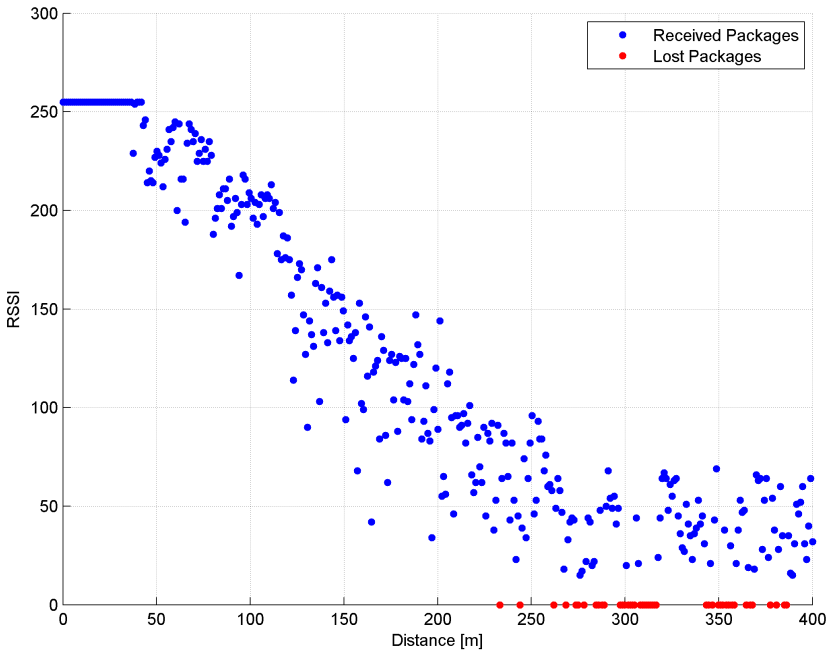

Figure 5.49: RSSI value of the received packets. The sender is moved towards the receiver.

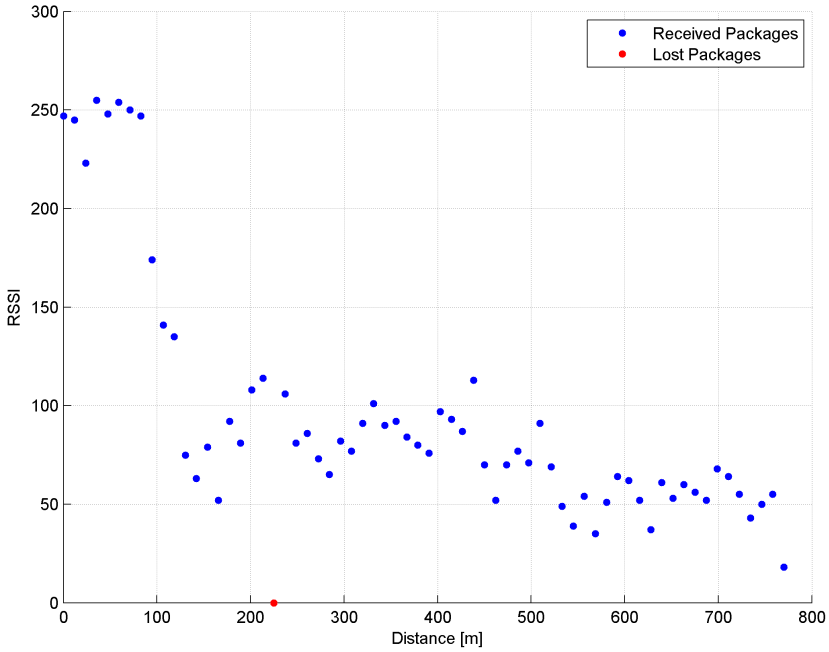

Figure 5.50: RSSI value of the received packets. The sender is moved away from the receiver.

Figure 5.49 shows the result of the second range test. The sender is moved towards the receiver with a speed of about $5\,km/h$. It starts at a distance of about $400\,m$. The distance has been decreased constantly. There is no line-of-sight connection between the sender and the receiver from $200\,m$ to $400\,m$. Therefore, the packet loss is much higher than at the previous measurement. Trees and small buildings are blocking the line-of-sight.

The results of the third measurement are shown in Figure 5.50. The sender is placed at a fix position and the receiver is moved at this measurement. The small number of packets is the result of the higher velocity of the movement. The speed of the car with the receiver is about $35\,km/h$. It can be seen that most of the packets are received successfully.

A measurement with reduced transmission power shows a maximum range of $500\,m$. The transmission power is reduced from $+20\,dB$ to $0\,dB$.

Therefore, it is possible to transmit packets over a distance of more than $500\,m$ even with a reduced transmission power.

6 Conclusion and Future Work

This master's thesis presents a new WSN platform for river monitoring. The platform includes an EHS that is used to harvest environmental energy with a solar cell. Ultracapacitors are used to store the energy for the night. This enhances the lifetime of the platform, because no batteries are used.

The RiverMote is equipped with a powerful 2.4GHz 802.14.4 RF module. It is used for communication and has a measured range of up to $800\,m$. The task of the RiverMote is to measure the water level of rivers. Therefore, the whole platform should be placed in a buoy. Two different measurement principles have been evaluated. The first principle is the measurement of the water level with ultrasonic sensors. The interval between the sent and the received ultrasonic waves is measured. The distance can be calculated using the measured interval. The second principle uses GPS modules to detect height differences between these measurements. A third measurement principle was envisioned but not implemented. It is the measurement of the river level using pressure transducers. However, the mote is conceived to be expanded by several sensors. Therefore, such a pressure transducer can be integrated easily.

The following Sections discuss the single units of the hardware and summarize the respective measurement results.

6.1 Energy Harvesting System

Solar cells are used to harvest the needed energy. These solar cells are selected specially to be able to charge the ultracapacitors directly (Schott Solar ASI3Oo05/162/192FAmod). This reduces the hardware complexity and the costs. The concept Section of this master's thesis has shown that the more ultracapacitors are connected in series the more energy can be stored. Therefore, two ultracapacitors are connected in series. The resulting nominal voltage of both ultracapacitors is $5\,V$ and the resulting capacity is $155\,F$.

The voltage of both ultracapacitors must be balanced. The reason is the difference of the leakage currents of both ultracapacitors. Measurements have shown that the voltage inverter is able to balance the voltages properly. Furthermore, the overcharge protection keeps the voltage under or equal to the nominal voltage.

Current counters are used to measure the solar and the mote current. The accuracy of these current counters depends on the current. The error of both current counters is higher at low currents. The accuracy of the mote current counter is better than $20\,\%$ if the mote current is greater than $2\,mA$. The accuracy of the solar current counter is better than $20\,\%$ if the solar current is greater than $3\,mA$. These accuracies are worse than the expected ones. However, they are sufficient to estimate the input and output power of the EHS system.

Three measurements have shown that the efficiency of the circuit of the EHS is about $80\,\%$. It is sufficient to supply the RiverMote. The loss of the direct charging process

depends on the voltage of the ultracapacitors. It is about 20 % at 3 V of the ultracapacitors. Therefore, the overall EHS efficiency is better than 66.56 % if the voltage of the ultracapacitors is not below this voltage.

The long-term measurement has shown that the EHS is able to supply continuously the mote. The WSN platform can operate energy-neutral, also on days with bad weather conditions.

6.2 Wireless Sensor Node

The following Sections discuss the results of the main components of the mote. The mote is also equipped with a USB interface. It is used for programming and communication with a PC.

6.2.1 Ultrasonic Unit

Measurements have shown that the ultrasonic unit is able to measure the water level of a test basin. A calibration of the ultrasonic unit has not been done, because it depends on the final housing and the placement of the ultrasonic transceivers. Furthermore, the circuit for generation of the ultrasonic waves should be placed away from the circuit for receiving the waves. However, the measurements have shown a proper functionality of the circuits.

6.2.2 GPS Module

The GPS module is able to receive the GPS signals and to communicate with the microcontroller. The GPS module can be programmed by the microcontroller to send specific data. The challenge is the uncorrelated data of different GPS modules of other RiverMotes. Furthermore, the measured height of the GPS modules varies very strongly. Therefore, the normal data output of the GPS module cannot be used to determine the height difference of two RiverMotes. However, the supply of the GPS module and the communication works properly. It can also be set to a sleep state by the microcontroller. The module stops working but does not loose any data in this state.

6.2.3 Microcontroller

The microcontroller cooperates properly with the other hardware components. It can be programmed via the USB interface. In addition, the communication between the microcontroller and a PC is possible via the USB interface. Therefore, the data of the mote can be sent to a PC and logged there.

The microcontroller is used to calculate the input and output power and the available power of the ultracapacitors. Therefore, it measures the solar voltage, the supply voltage and the voltage of the ultracapacitors. Furthermore, it counts the pulses of the current counters. Measurements have shown that the microcontroller is able to measure these values.

The microcontroller can communicate with the RF module. Therefore, a wireless communication between different nodes is possible and has been tested. Measurements have

shown a range of up to 800 m at full power. The measurements have also shown that the loss rate within the range depends mainly on the obstacles between the sender and the receiver.

The microcontroller is connected to an expansion connector. Therefore, the mote can be extended with different sensors. This ensures a high flexibility of the whole WSN platform.

6.3 Software

The implemented software is sufficient to test the functionality of the WSN hardware. It is not suited for bigger projects. The access to the hardware should be unified by using abstraction layers as shown in Figure 2.6. The implemented classes are also an overhead for the functionality. Much code is generated by the compiler due to the classes. Therefore, the functionality can be encapsulated in normal functions. This would reduce the generated code and enhance the programming speed.

6.4 Future Work

The following list shows the possible improvements of the hardware of the introduced WSN platform:

Current Counters: The error of the current counters is high at low currents. The accuracy can be improved by selecting better components of the current counter. The integration capacitor should have a low tolerance and low leakage currents. Besides, the leakage currents of other components of the current counter (e.g. the operational amplifier and the MOSFET) should be as low as possible.

Maximum Power Point Tracking: The EHS can be improved by implementing a maximum power point tracker. This enhances the energy that can be harvested from the solar cell. Therefore, the whole EHS must be redesigned. This is complex and there will be a rise in costs of one RiverMote.

USB Interface: The USB interface can be skipped if the mote is used for long-term measurements. It can be programmed via the JTAG interface and the RF module can be used for communication.

Ultrasonic Module: The ultrasonic module can be improved in three ways:

1. The circuit for the generation of the ultrasonic waves should be separated from the circuit for receiving the reflected waves. Therefore, the reflected sound waves can be detected easier.
2. The circuit for the generation of the ultrasonic waves can be improved itself. Ultrasonic waves with higher amplitudes can be generated with higher output voltages. Therefore, the reflected waves have higher amplitude and they can be detected easier.
3. The circuit for receiving the reflected ultrasonic waves can be improved, too. The gain of the amplifier can be enhanced to be able to detect the reflected waves better.

The software, which is used for the tests, can also be improved. The following list shows the possible improvements of the software of the WSN platform:

Software Structure: The software structure should be redesigned to reduce the code size and for a better abstraction. The software should be split in different layers to enhance the flexibility as discussed in Section 6.3.

TinyOS: As mentioned at the beginning of this master's thesis, it seems possible to port TinyOS to the hardware of the WSN platform. It is a big task because the porting is very complex. Since the same microcontroller is used as with the TelosB mote, big parts of the code can be reused. One of the big changes is the communication module. It is new and therefore, new drivers must be written.

GPS Module: The standard data of the GPS module cannot be used to measure the height difference of two RiverMotes. It might be possible to access the raw data of the GPS module. The GPS module must be programmed to send the raw data to the microcontroller. These data can be analyzed to determine the height of the GPS receiver.

The programs, which are used for programming and for communication with the mote, can be improved, too:

BSL programmer: The programming speed of the BSL programmer could be enhanced. This would reduce the programming time.

Integration: The programming software and the logging software could be integrated in a single environment. This would improve the flexibility and the usability of the software.

A Appendix: Circuit Diagrams

The complete circuit diagram of the EHS can be found on the pages 108 and 109. The first image on page 108 shows the overcharge protection of the EHS. This circuit is the same circuit as simulated in Section 4.1.1. The voltage conditioning circuit and the capacitor balancing circuit can also be found on this page. The second image on page 109 shows the solar current counter and the mote current counter. The connector to the mote is also shown on this page.

The complete circuit diagram of the mote can be found on pages 110 to 112. The first image on page 110 shows the connection of the microcontroller. The connector to the EHS, the JTAG connector and the expansion connector are also shown on this page. The second image on page 111 shows the USB interface including the power supply via USB and the decoupling circuit. It also shows the reset circuit and the LED circuit. The third image on page 112 shows the radio module, the GPS interface and the ultrasonic circuit.

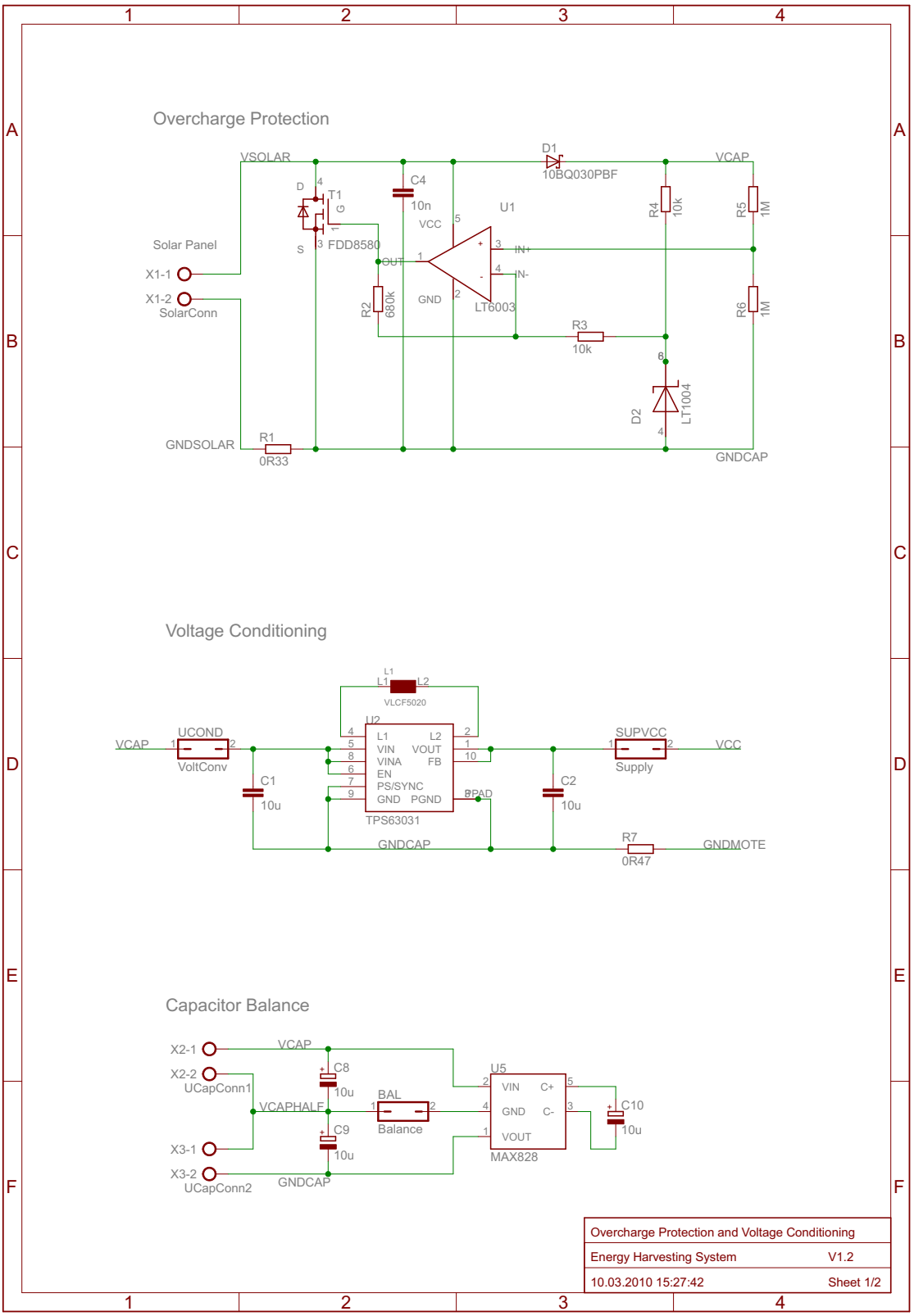
Overcharge Protection
VSOLAR
D1
10BQ030PBF
VCAP
C4
10n
U1
R4
10k
R5
1M
T1
FDD8580
Solar Panel
X1-1
X1-2
SolarConn
OUT
VCC
IN+
IN-
GND
LT6003
R2
680k
R3
10k
R6
1M
D2
LT1004
R1
0R33
GNDSOLAR
GNDCAP
Voltage Conditioning
L1
VLCF5020
U2
VIN
VOUT
VINA
FB
EN
PS/SYNC
GND
PGND
PPAD
TPS63031
VCAP
UCOND
VoltConv
C1
10u
C2
10u
SUPVCC
Supply
VCC
R7
0R47
GNDMOTE
GNDCAP
Capacitor Balance
X2-1
X2-2
UCapConn1
X3-1
X3-2
UCapConn2
VCAP
C8
10u
VCAPHALF
C9
10u
BAL
Balance
U5
VIN
C+
GND
C-
VOUT
MAX828
C10
10u
GNDCAP
Overcharge Protection and Voltage Conditioning
Energy Harvesting System V1.2
10.03.2010 15:27:42 Sheet 1/2

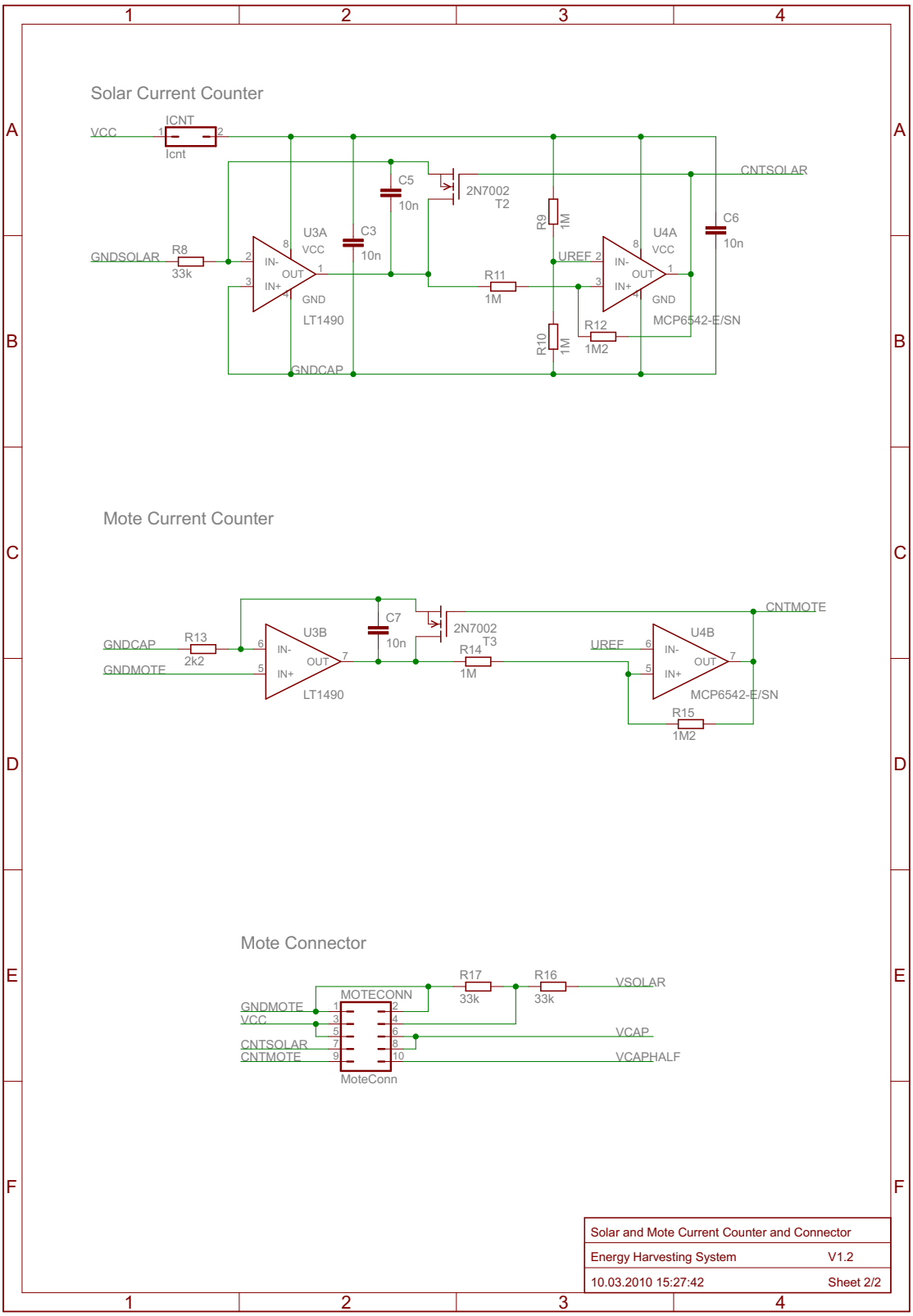
Solar Current Counter
VCC
ICNT
Icnt
CNTSOLAR
C5
10n
2N7002
T2
R9
1M
C6
10n
GNDSOLAR
R8
33k
U3A
VCC
IN-
IN+
OUT
GND
LT1490
C3
10n
UREF
R11
1M
U4A
MCP6542-E/SN
R10
1M
R12
1M2
GNDCAP
Mote Current Counter
CNTMOTE
GNDCAP
R13
2k2
GNDMOTE
U3B
C7
10n
2N7002
T3
R14
1M
UREF
U4B
MCP6542-E/SN
R15
1M2
Mote Connector
MOTECONN
R17
33k
R16
33k
VSOLAR
GNDMOTE
VCC
CNTSOLAR
CNTMOTE
VCAP
VCAPHALF
MoteConn
Solar and Mote Current Counter and Connector
Energy Harvesting System V1.2
10.03.2010 15:27:42 Sheet 2/2

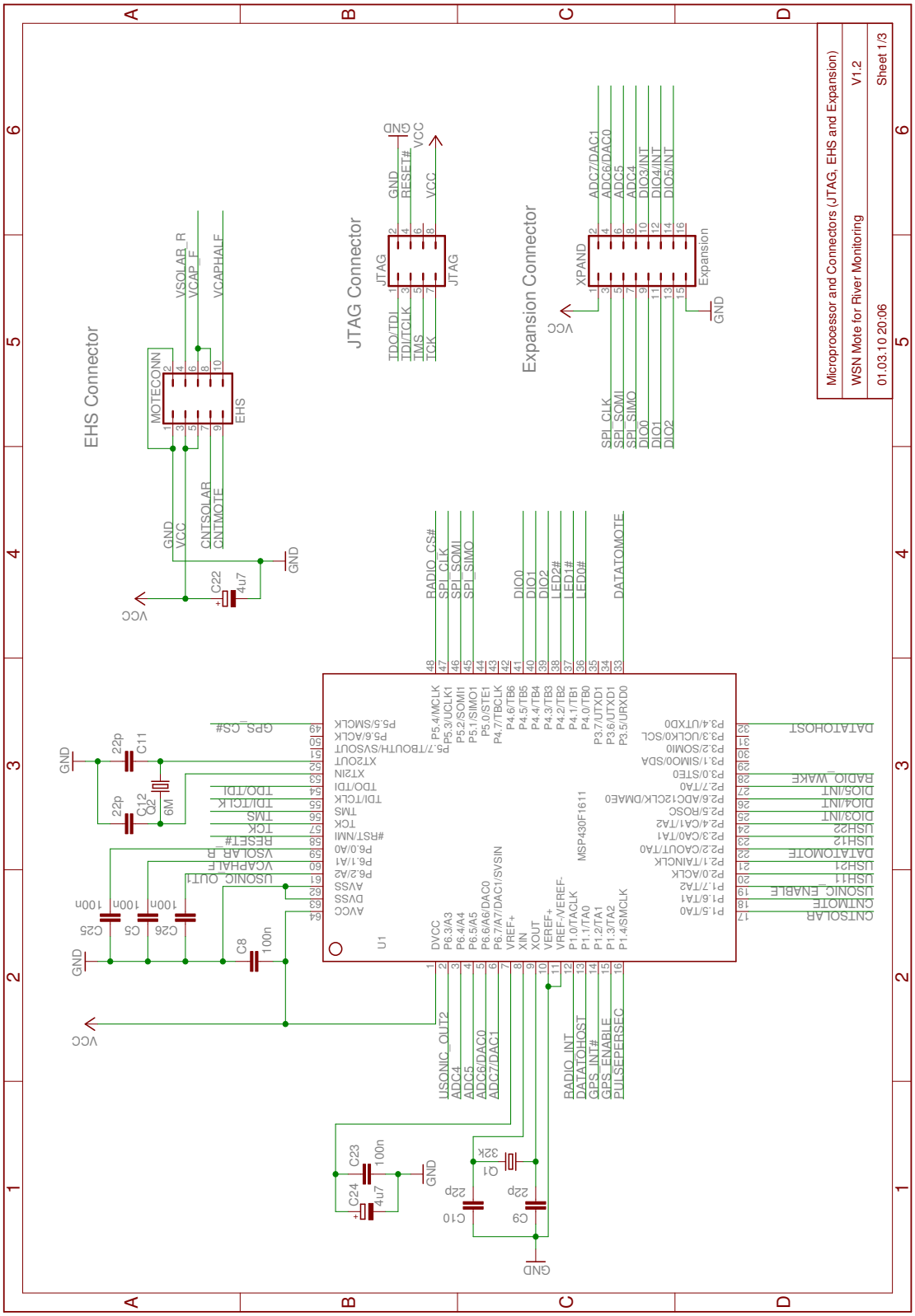
Microprocessor and Connectors (JTAG, EHS and Expansion)
V1.2
WSN Mote for River Monitoring
01.03.10 20:06
Sheet 1/3
EHS Connector
JTAG Connector
Expansion Connector
MSP430F1611
U1
Q1
Q2
32k
6M

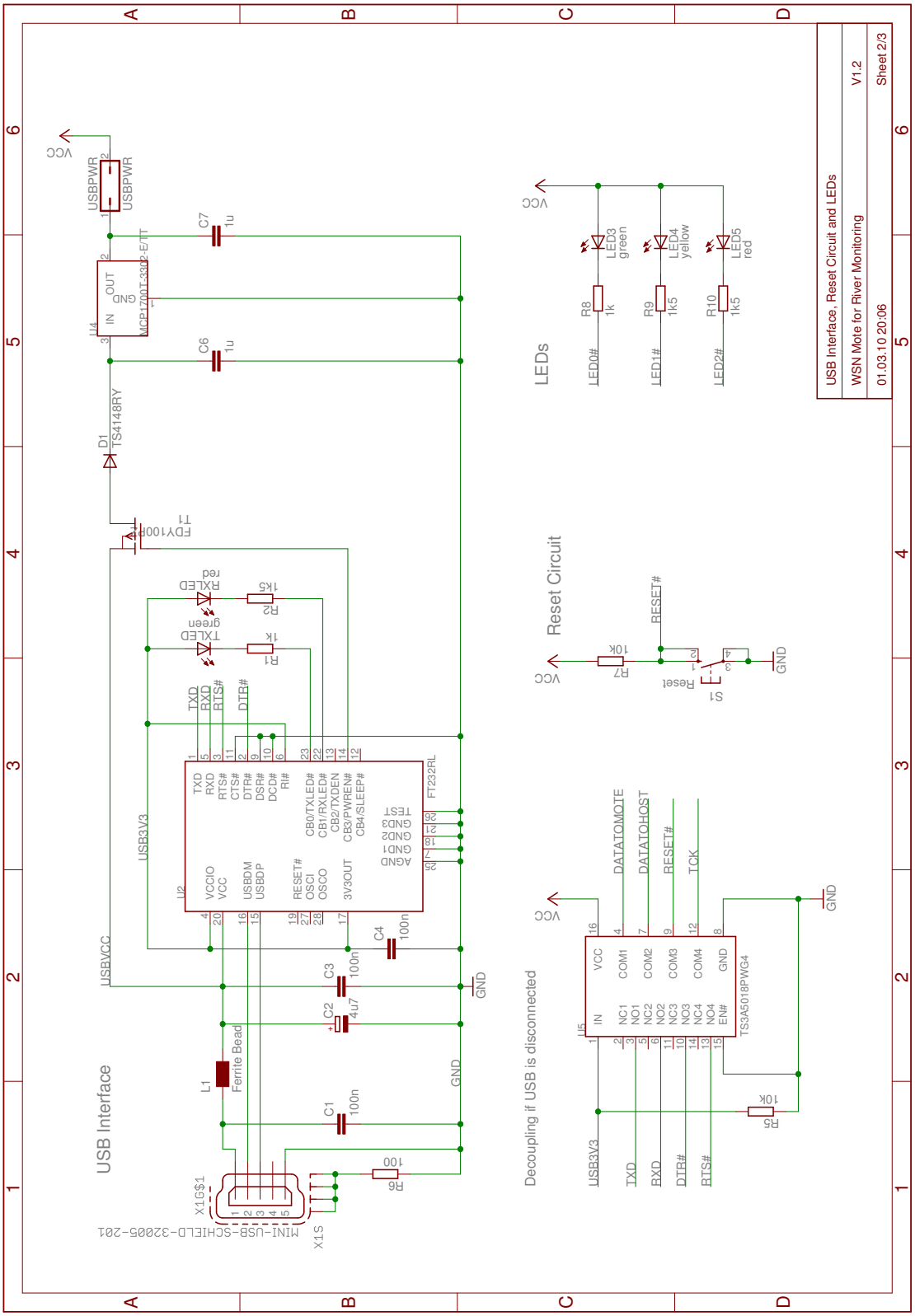
USB Interface
Reset Circuit
LEDs
Decoupling if USB is disconnected
USB Interface, Reset Circuit and LEDs
WSN Mote for River Monitoring
V1.2
01.03.10 20:06
Sheet 2/3
VCC
GND
USBPWR
C7 1u
C6 1u
U4 MCP1700T-3302E/TT
D1 TS4148RY
T1 FDY100H
RXLED red
TXLED green
R2 1K5
R1 1K
TXD
RXD
RTS#
DTR#
U2 FT232RL
USB3V3
USBVCC
C4 100n
C3 100n
C2 4u7
L1 Ferrite Bead
C1 100n
R6 100
X1G$1
MINI-USB-SCHIELD-32005-201
X1S
LED0# R8 1k LED3 green
LED1# R9 1k5 LED4 yellow
LED2# R10 1k5 LED5 red
RESET# R7 10K S1 Reset
U5 TS3A5018PWG4
DATATOMOTE
DATATOHOST
RESET#
TCK
R5 10K

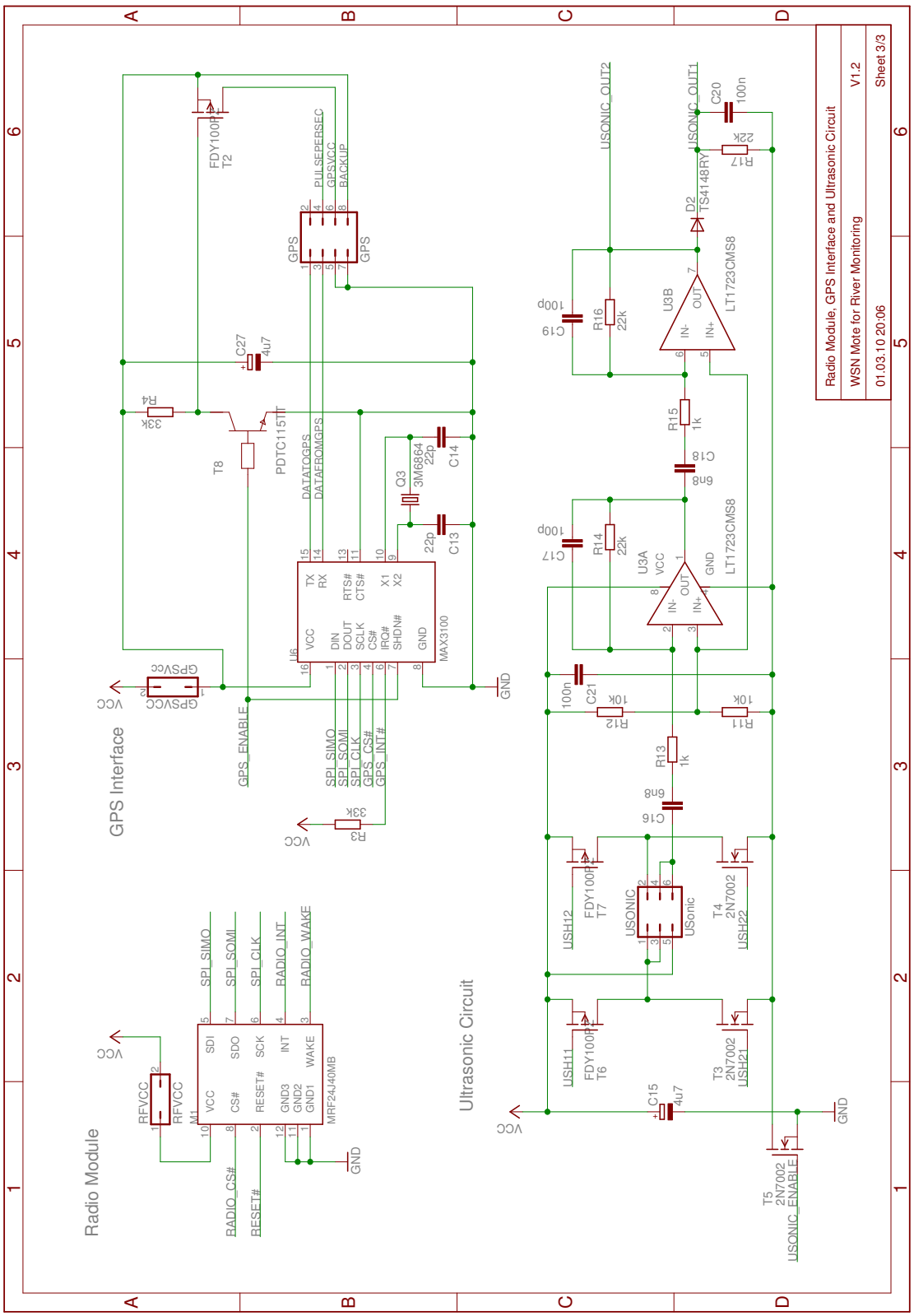
Radio Module, GPS Interface and Ultrasonic Circuit
WSN Mote for River Monitoring
V1.2
01.03.10 20:06
Sheet 3/3
GPS Interface
Radio Module
Ultrasonic Circuit
MAX3100
MRF24J40MB
LT1723CMS8
TS4148RY
PDTC115TT
3M6864
FDY100PT
2N7002
GPS_ENABLE
USONIC_ENABLE
RADIO_CS#
RESET#
SPI_SIMO
SPI_SOMI
SPI_CLK
RADIO_INT
RADIO_WAKE
GPS_CS#
GPS_INT#
USONIC_OUT1
USONIC_OUT2
VCC
GND

B Appendix: Hardware Illustration

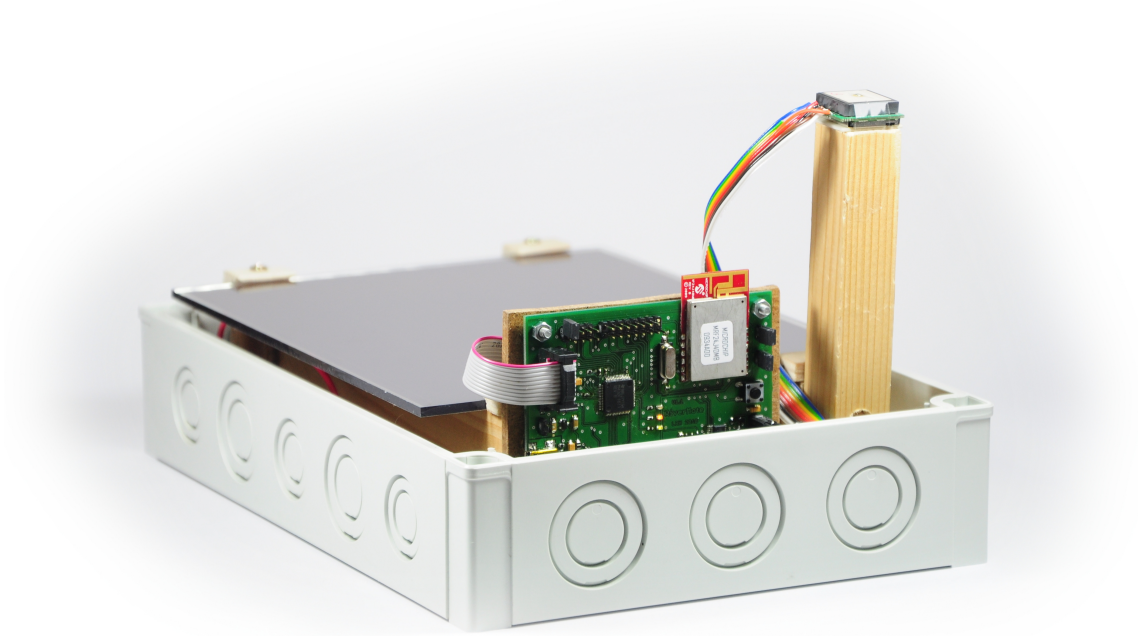

Figure B.1: Illustration of the RiverMote hardware including the solar cell and the housing.

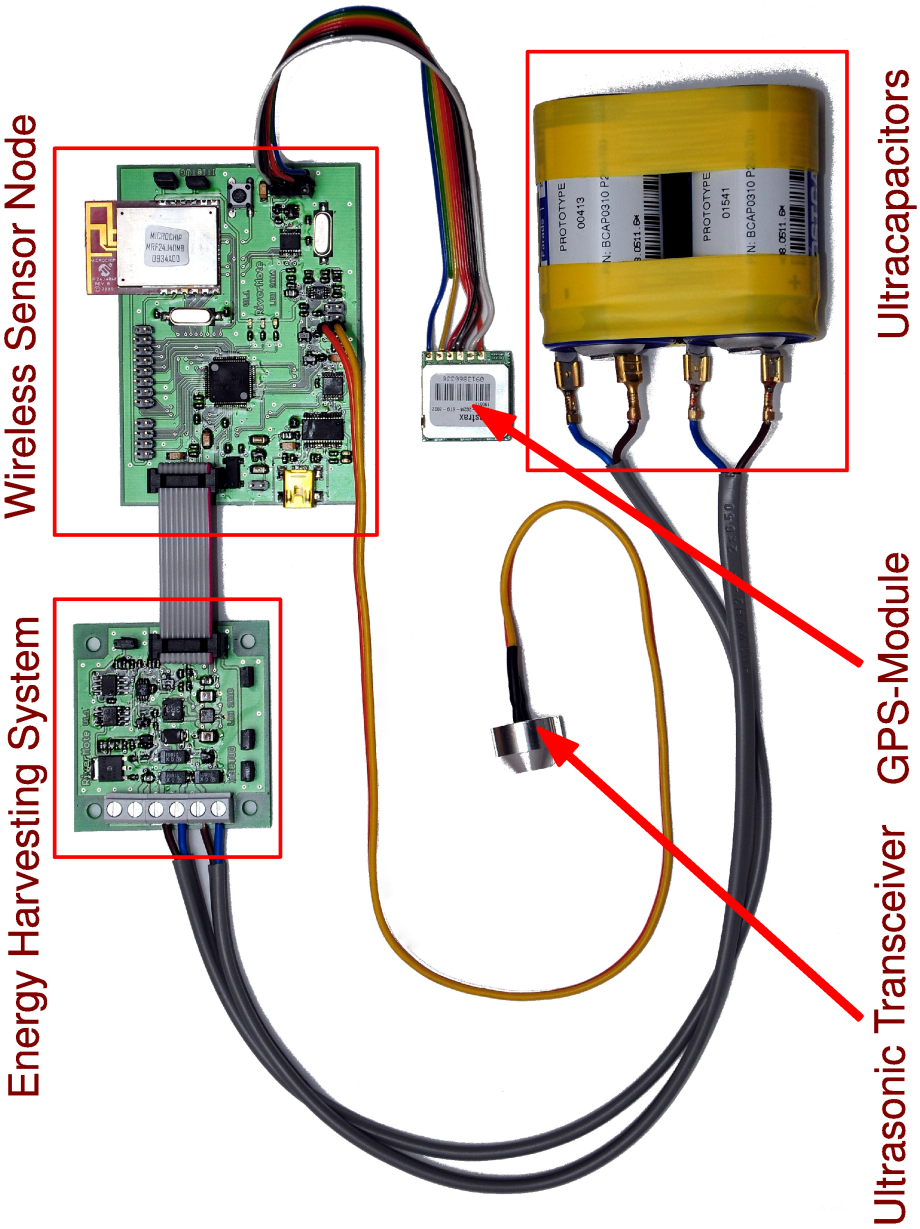

Figure B.2: Illustration of the RiverMote hardware (without solar cell).

Bibliography

[1] I. F. Akyildiz, W. Su, Y. Sankarasubramaniam, and E. Cayirci. Wireless sensor networks: a survey. *Computer Networks*, 38(4):393–422, 2002.

[2] C. Alippi and C. Galperti. An adaptive system for optimal solar energy harvesting in wireless sensor network nodes. *IEEE Transactions on Circuits and Systems I: Regular Papers*, 55(6):1742–1750, July 2008.

[3] C. Bergonzini, D. Brunelli, and L. Benini. Algorithms for harvested energy prediction in batteryless wireless sensor networks. In *3rd International Workshop on Advances in sensors and Interfaces*, pages 144–149, June 2009.

[4] E. Böhmer. *Elemente der angewandten Elektronik*. Friedr. Vieweg & Sohn, 12 edition, 2000.

[5] M. Bromage, K. Obraczka, and D. Potts. Sea-labs: A wireless sensor network for sustained monitoring of coral reefs. *NETWORKING 2007. Ad Hoc and Sensor Networks, Wireless Networks, Next Generation Internet*, pages 1132–1135, 2007.

[6] M. Broussely, S. Herreyre, P. Biensan, P. Kasztejna, K. Nechev, and R. J. Staniewicz. Aging mechanism in li ion cells and calendar life predictions. *Journal of Power Sources*, 97-98:13–21, 2001.

[7] J.-H. Chang and L. Tassiulas. Maximum lifetime routing in wireless sensor networks. *IEEE/ACM Trans. Netw.*, 12(4):609–619, 2004.

[8] C.-T. Chen and F. J. Millero. Reevaluation of wilson's sound-speed measurements for pure water. *The Journal of the Acoustical Society of America*, 60(6):1270–1273, 1976.

[9] P. Corke, P. Valencia, P. Sikka, T. Wark, and L. Overs. Long-duration solar-powered wireless sensor networks. In *EmNets '07: Proceedings of the 4th workshop on Embedded networked sensors*, pages 33–37, New York, NY, USA, 2007. ACM.

[10] C. Enz, N. Scolari, and U. Yodprasit. Ultra low-power radio design for wireless sensor networks. In *Radio-Frequency Integration Technology: Integrated Circuits for Wideband Communication and Wireless Sensor Networks*, pages 1–17, Nov.-2 Dec. 2005.

[11] P. Glatz, P. Meyer, A. Janek, T. Trathnigg, C. Steger, and R. Weiss. A measurement platform for energy harvesting and software characterization in wsns. pages 1–5, nov. 2008.

[12] V. Handziski, J. Polastre, J.-H. Hauer, C. Sharp, A. Wolisz, and D. Culler. Flexible hardware abstraction for wireless sensor networks. In *Proceedings of the 2nd European Workshop on Wireless Sensor Networks*, pages 145–157, Jan.-2 Feb. 2005.

[13] F. Hicks, P. M. Steffler, and R. Gerard. Finite element modeling of surge propagation and an application to the hay river, n.w.t. *Canadian Journal of Civil Engineering CJCEB8*, 19:454–462, 1992.

[14] D. Hughes, G. Blair, G. Coulson, P. Greenwood, B. Porter, P. Smith, and K. Beven. An adaptable wsn-based flood monitoring system.

[15] D. Hughes, P. Greenwood, G. Blair, G. Coulson, P. Smith, and K. Beven. An intelligent and adaptable grid-based flood monitoring and warning system.

[16] A. Janek, C. Trummer, C. Steger, R. Weiss, J. Preishuber-Pfluegl, and M. Pistauer. Simulation based verification of energy storage architectures for higher class tags supported by energy harvesting devices. *Microprocessors and Microsystems*, 32(5-6):330–339, 2008. Dependability and Testing of Modern Digital Systems.

[17] A. Kansal, J. Hsu, S. Zahedi, and M. B. Srivastava. Power management in energy harvesting sensor networks. *ACM Trans. Embed. Comput. Syst.*, 6(4):32, 2007.

[18] A. Kansal, D. Potter, and M. B. Srivastava. Performance aware tasking for environmentally powered sensor networks. In *SIGMETRICS '04/Performance '04: Proceedings of the joint international conference on Measurement and modeling of computer systems*, pages 223–234, New York, NY, USA, 2004. ACM.

[19] Kingbright. Smd chip led lamp (superbright yellow). SPEC NO: KDA0024, Sept. 2001.

[20] Kingbright. Smd chip led lamps (super bright green). SPEC NO: KDA0081, Sept. 2001.

[21] Kingbright. Smd chip led lamp (hyper red). SPEC NO: DSAA4838, June 2007.

[22] J.-S. Lee and Y.-C. Huang. Itri zbnode: A zigbee/ieee 802.15.4 platform for wireless sensor networks. In *IEEE International Conference on Systems, Man and Cybernetics*, volume 2, pages 1462–1467, Oct. 2006.

[23] J.-W. Lee, Y. K. Anguchamy, and B. N. Popov. Simulation of charge-discharge cycling of lithium-ion batteries under low-earth-orbit conditions. *Journal of Power Sources*, 162(2):1395–1400, 2006.

[24] K. Martinez and R. Ong. Glacsweb: a sensor network for hostile environments. In *IEEE SECON*, pages 81–87, 2004.

[25] MAXIM. Voltage-inverter ic forms high-efficiency rail splitter - an1199. http://www.maxim-ic.com, Application Note AN1199, Aug. 1997.

[26] MaxwellTechnologies. Datasheet bcap0310 p250. http://www.maxwell.com, Document number: 1009473.5, November 2009.

[27] Microchip®. Mrf24j40 data sheet - ieee 802.15.4 2.4 ghz rf transceiver. www.microchip.com, DS39776B, 2008.

[28] M. Minami, T. Morito, H. Morikawa, and T. Aoyama. Solar biscuit: A battery-less wireless sensor network system for environmental monitoring applications. *The 2nd International Workshop on Networked Sensing Systems*, 2005.

[29] J. M. Molina, P. Isasi, A. Berlanga, and A. Sanchis. Hydroelectric power plant management relying on neural networks and expert system integration. *Engineering Applications of Artificial Intelligence*, 13(3):357–369, 2000.

[30] T. Moore, K. Zhang, G. Close, and R. Moore. Real-time river level monitoring using gps heighting. *GPS Solutions*, 4:63–67, 2000.

[31] G. Morgan-Owen and G. Johnston. Differential gps positioning. *Electronics & Communication Engineering Journal*, 7(1):11–21, Feb 1995.

[32] T. Muneer. *Solar Radiation and Daylight Models*. Elsevier Butterworth-Heinemann, 2004.

[33] NationalInstruments. Pxi6221 - low-cost m series multifunction data acquisition - 16-bit, 250ks/s, up to 80 analog inputs. www.ni.com, Mar. 2010.

[34] H. Patt, P. Jürging, and W. Kraus. *Naturnaher Wasserbau - Entwicklung und Gestaltung von Fließgewässern*. Springer Berlin Heidelberg, 2009.

[35] E. J. Plate. Flood risk and flood management. *Journal of Hydrology*, 267(1-2):2–11, 2002.

[36] J. Polastre, R. Szewczyk, and D. Culler. Telos: enabling ultra-low power wireless research. In *Proceedings of the 4th international symposium on Information processing in sensor networks*, page 48. IEEE Press, 2005.

[37] D. Puccinelli and M. Haenggi. Wireless sensor networks: applications and challenges of ubiquitous sensing. *Circuits and Systems Magazine, IEEE*, 5(3):19–31, 2005.

[38] V. Raghunathan, A. Kansal, J. Hsu, J. Friedman, and M. Srivastava. Design considerations for solar energy harvesting wireless embedded systems. In *Proceedings of the 4th international symposium on Information processing in sensor networks*, page 64. IEEE Press, 2005.

[39] D. Raskovic, O. Lewis, and D. Giessel. Time synchronization for wireless sensor networks operating in extreme temperature conditions. *41st Southeastern Symposium on System Theory*, pages 24–28, 2009.

[40] K. Römer and F. Mattern. The design space of wireless sensor networks. *IEEE Wireless Communications*, 11(6):54–61, Dec. 2004.

[41] SchottSolar. Asi oem outdoor solar modules. http://www.schottsolar.com, 2007.

[42] W. Seah, Z. A. Eu, and H.-P. Tan. Wireless sensor networks powered by ambient energy harvesting (wsn-heap) - survey and challenges. In *1st International Conference on Wireless Communication, Vehicular Technology, Information Theory and Aerospace & Electronic Systems Technology*, pages 1–5, May 2009.

[43] TexasInstruments®. Msp430x1xx family - user's guide. www.focus-ti.com, SLAU049F, 2006.

[44] TexasInstruments®. Tps63001 - high efficient single inductor buck-boost converter with 1.8-a switches. www.focus-ti.com, SLVS520B, July 2008.

[45] TexasInstruments®. Msp430f15x, msp430f16x, msp430f161x mixed signal microcontroller. www.focus-ti.com, SLAS368F, 2009.

[46] TinyOSCommunityForum. Tinyos hardware designs. http://www.tinyos.net/scoop/special/hardware, November 2009.

[47] I. Vasilescu, K. Kotay, D. Rus, M. Dunbabin, and P. Corke. Data collection, storage, and retrieval with an underwater sensor network. In *Proceedings of the 3rd international conference on Embedded networked sensor systems*, pages 154–165. ACM, 2005.

[48] G. Werner-Allen, J. Johnson, M. Ruiz, J. Lees, and M. Welsh. Monitoring volcanic eruptions with a wireless sensor network. In *Proceedings of the Second European Workshop on Wireless Sensor Networks*, 2005.

[49] Wikipedia. Luftdruck. http://de.wikipedia.org/wiki/Luftdruck, November 2009.

[50] H. Yin and C. Li. Human impact on floods and flood disasters on the yangtze river. *Geomorphology*, 41(2-3):105–109, 2001.

[51] M. A. Youssef. A constrained shortest-path energy-aware routing algorithm for wireless sensor networks. In *Wireless Commun. and Networking Conference*, pages 794–799, 2002.

[52] J. Zhang, C. Zhou, K. Xu, and M. Watanabe. Flood disaster monitoring and evaluation in china. *Global Environmental Change Part B: Environmental Hazards*, 4(2-3):33–43, 2002.